GROWTH AND CHARACTERIZATION OF GREEN ELECTROLUMINESCENT THIN FILMS

By

TAO FENG

A DISSERTATION PRESENTED TO THE GRADUATE SCHOOL
OF THE UNIVERSITY OF FLORIDA IN PARTIAL FULFILLMENT
OF THE REQUIREMENTS FOR THE DEGREE OF
DOCTOR OF PHILOSOPHY

UNIVERSITY OF FLORIDA

2001

ACKNOWLEDGMENTS

First of all, I am greatly indebted to my adviser and my committee chairman Dr. P. H. Holloway, who gave me guidance and support. I feel fortunate to be guided by Dr. Holloway. Working for Dr. Holloway was the richest three years in my life. I learned immensely from him.

It is also my great honor to have four other distinguished professors (Dr. Robert Dehoff, Dr. Kevin Jones, Dr. Rolf Hummel and Dr. Fan Ren) as my committee members.

In addition, I thank Dr. Mark Davidson, who offered me help and advice with every detail of my project. Regarding pulsed laser deposition, I am truly thankful to Dr. Rajiv Singh and Dr. D. Kumar at the University of Florida, and Dr. Jim Fitz-Gerald and Dr. Heungsoo Kim at Naval Research Lab.

For sample analyses, I am especially grateful to Dr. Maggie Puga-Lambers on SIMS, Wayne Acree on EDX/SEM, Dr. Michael Kaufmann on XTEM, and Eric Lambers on XPS.

I also appreciate the help and input my colleagues in Dr. Holloway's group offered to me. I especially thank Joohan Kim for sputtering deposition, Jay Lewis and Jong-pyo Kim for electrical measurement and Bill Glass for optical characterization.

Finally, I am indebted immeasurably to my parents who gave me love and support all the time.

TABLE OF CONTENTS

CHAPTERS page

Abstract of Dissertation Presented to the Graduate School
of the University of Florida in Partial Fulfillment of the
Requirements for the Degree of Doctor of Philosophy

GROWTH AND CHARACTERIZATION OF
GREEN ELECTROLUMINESCENT THIN FILMS

By

Tao Feng

August 2001

Chairman: Dr. P. H. Holloway
Major Department: Materials Science and Engineering

Growth and characterization of Pulsed laser deposited and sputter deposited green Zn_2GeO_4:Mn and electron beam evaporated $Zn_{1-x}Mg_xS$:Mn thin films were investigated.

Experimental results show that electroluminescent brightness of Zn_2GeO_4:Mn grown by sputter deposition was independent of working pressure and Ar/O_2 ratio. Green photo- and electroluminescence were obtained from Zn_2GeO_4:Mn films deposited on Si (for photoluminescence only), glass/ITO/ATO and Al_2O_3/Au/Pb(ZrTi)O_3 substrates with the emission wavelength at 540 nm and CIE color coordinate at x = 0.263 and y = 0.683. The Zn_2GeO_4:Mn electroluminescent film grown on a dielectric layer of Pb(ZrTi)O_3 by pulsed laser deposition showed much higher brightness than that grown by sputter deposition (450 cd/m^2 versus 120 cd/m^2 at 2.5 kHz) primarily due to better film crystallinity resulting from higher substrate temperature (250^{o}C versus R.T.) and from surface damage resulting from high energy Ar plasma. Zn_2GeO_4:Mn deposited on

Al_2O_3/Au/Pb(ZrTi)O_3 substrate showed higher EL brightness (450 cd/m^2 versus 45 cd/m^2 at 2.5kHz) than that deposited on glass/ITO/ATO due to better crystallinity resulting from a longer annealing time, and higher breakdown electric field for the thicker Pb(ZrTi)O_3 layer. The Zn_2GeO_4:Mn grown by pulsed laser deposition was Zn-deficient (Zn/Ge atomic ratio = 0.83 and 0.77 at a substrate temperature of 250^{o}C and 800^{o}C). A reaction of Zn_2GeO_4:Mn and Pb(ZrTi)O_3 was observed upon annealing at temperature over 800^{o}C. Optimum annealing for Zn_2GeO_4:Mn on Pb(ZrTi)O_3 was obtained using a temperature of 700^{o}C for 5 hours. The Zn_2GeO_4:Mn grown on Pb(ZrTi)O_3 substrate showed extremely poor EL brightness when the film thickness was smaller than 5000Å. This was hypothesized to be due to a reduced voltage drop across the phosphor layer because Zn_2GeO_4:Mn was not continuous. In addition, a large leakage current resulted from the rough Zn_2GeO_4:Mn/Pb(ZrTi)O_3 interface.

By partially substituting Mg for Zn, $Zn_{1-x}Mg_xS$:Mn electroluminescent emission showed a green shift compared with the yellow/orange of ZnS:Mn due to crystal field reduction. Green photo- and electroluminescence were obtained from Zn_2GeO_4:Mn film deposited on glass/ITO/ATO substrate with the emission wavelength at 578 nm and CIE color coordinates at x = 0.5049, and y = 0.4900 versus ZnS:Mn emission at 592 nm, and the CIE coordinates at x = 0.5451, y = 0.4529). Film doped from a MnS source-doping exhibited EL brightness of 40 cd/m^2 for 6700Å while those doped from metallic Mn source exhibit 90 cd/m^2 for 13500Å both at 60Hz. Optimum Mn doping of 0.12% in the ZnMgS:Mn film was determined using SIMS. Using cross section TEM, columnar ZnMgS crystallites were observed in $Zn_{0.8}Mg_{0.2}S$:Mn.

CHAPTER 1
INTRODUCTION

The history of phosphors has spanned nearly 400 years. Phosphor was first observed in 1603.[1] One of the first large-scale commercializations of a device using phosphors was television tubes, which are also known as cathode ray tube (CRT).[2] The first practical electroluminescent display was reported by Sharp corporation in 1974.[3] Use of electronic displays began with the development of the CRT. However, the CRT had inherent disadvantages in its thick glass tube and large size (depth beyond 35”), required for scanning of the electron beam across the phosphor screen. Driven by portable electronics applications, flat panel display technologies are now under active development. The flat panel display industry accounts for almost 50% of the total display market and is expected to increase to 63% of a more than $100 billion market by the year 2005.[4] Included among flat panel technologies are liquid crystal display (LCD),[5] plasma display panel (PDP),[6] inorganic light emitting diode (LED),[7] organic LED (OLED),[8] also known as organic electroluminescent display (OEL) and field emission display (FED),[9] laser-based diode display (LDD) and electroluminescent (EL) display. [10] Currently, the flat panel display market is dominated by LCDs and PDPs are just reaching the market as mass produced product, even though it is clear that neither currently meets the demanding economic and performance requirements for this application, leaving the market open to still-developing technologies. Only EL displays are discussed in detail. The reader is referred to several other reviews that discuss other displays for more information.[11], [12], [13], [14]

Electroluminescence in ZnS:Cu was first reported by Gudden and Pohl in 1920. [3] Since then, electroluminescent devices were developed from powder to thin film, from DC to AC, from inorganic to organic, and from monochrome to multicolor. The first electroluminescent display using ZnS:Mn phosphor was developed by Sharp in 1974.[15,16] Currently, the leading companies to develop EL displays are Sharp, Planar Systems and Tektronix. The alternating-current thin-film electroluminescence (ACTFEL) display has found its place in the market region that relies on its wide operation temperature range from -40^{o} to 150^{o}C, as well as its wide view angle and large contrast ratio and ruggedness.[1] Its applications include medical, automotive, industrial and military.[4] The advantage of the wide operation temperature range is especially attractive for military applications. Power consumption and operation voltage of these displays is higher than the available portable electronics. The largest limitations for the technology are the lack of a full-color, red-green-blue (RGB) product and the low brightness. The sensitivity of human eyes to green is much lower than red and the relative brightness of R, G, B for a good white is 1:4:1. [10, 17] So far, the best red brightness is obtained from filtered yellow ZnS:Mn, which is 65 cd/m^2 at 60 Hz drive frequency.[10] In order to match this best red brightness, 260 cd/m^2 of the green brightness is required for a white. However, the best green phosphor available is ZnS:Tb, which gives 100 cd/m^2 at 60 Hz drive frequency. Therefore, further developments in green-emitting ACTFEL phosphors are desired. There is a need to seek new green candidates to improve brightness and stability. In this dissertation, two phosphors used for green ACTFEL devices were studied: one oxide (Zn_2GeO_4:Mn) and one sulfide ($Zn_{1-x}Mg_xS$:Mn).

Chapter 2 presents a background of ACTFEL devices and a general understanding of the phosphor thin film growth techniques and the device operation. In Chapter 3, experimental procedures are presented that cover thin film growth, heat treatment and characterization. In Chapter 4, characterization results are shown for the first Zn_2GeO_4:Mn ACTFEL devices fabricated using pulsed laser deposition. Results show a higher brightness in the Zn_2GeO_4:Mn ACTFEL devices deposited on $Pb(ZrTi)O_3$ compared with those deposited on glass/ITO/ATO, resulting from improved phosphor film crystallinity due to much longer allowed annealing times. In Chapter 5, the film growth optimization and characterization results of Zn_2GeO_4:Mn ACTFEL devices produced using RF sputtering deposition are presented, which shows that the performance of Zn_2GeO_4:Mn ACTFEL devices is insensitive to the growth parameters of base pressure, working pressure and Ar/O_2 ratio over a large range. The Zn_2GeO_4:Mn ACTFEL devices fabricated using the two previously mentioned deposition techniques are shown to exhibit green emission at a broad peak around 540 nm. In Chapter 6, the important results are discussed showing a dramatically better performance in the pulsed laser deposited Zn_2GeO_4:Mn ACTFEL device compared with the sputter deposited device. This improved performance is due to the less surface damage and a higher substrate temperature used in PLD processing, both of which lead to improved crystallinity. I also discuss the substantially reduced performance of Zn_2GeO_4:Mn ACTFEL devices on annealing at 800^oC. Degradation of device performance in this case results from the reaction of Zn_2GeO_4:Mn with its underlying layer $Pb(ZrTi)O_3$. In Chapter 7, an investigation into electron-beam (e-beam) evaporated ZnMgS:Mn ACTFEL devices is presented showing that use of a MnS doping source gave better

performance than a metal Mn doping source. Further, the best performance was found at optimum Mn^{2+} 0.12% in film and MgS phase segregation in the film was observed using XTEM. Chapter 8 gives conclusions.

CHAPTER 2
LITERATURE REVIEW

2.1 Introduction

The definition of electroluminescence (EL) is the non-thermal generation of light resulting from the application of an electric field to a substance,[16] usually a semiconductor. The electroluminescence discussed in this dissertation is different from that of inorganic semiconductor-based light emitting diodes (LEDs), diode lasers or organic electroluminescence (OEL). Excitation of a luminescent center in the present type of EL involves ballistic electron transport in an inorganic host rather than the recombination of electron-hole pairs in a p-n junction. To be more specific, the electroluminescence discussed here is thin film alternating electroluminescence, rather than powder electroluminescence or DC electroluminescence, each of which works by a different mechanism.[16]

This chapter covers information from the fundamentals of the EL device to the literature review of the two green phosphors Zn_2GeO_4:Mn and ZnMgS:Mn studied in this dissertation. The fundamentals of the EL device include the device structures, device operation physics and device materials. The literature review of Zn_2GeO_4:Mn ACTFEL devices focuses on the pulsed laser deposition and the sputtering deposition of available oxide phosphors. The literature review of ZnMgS:Mn concentrates on the results of the electron-beam (e-beam) evaporated ZnMgS:Mn, the issue of ZnS-MgS solubility, and the mechanism of crystal field modification due to Mg substitution for Zn.

2.2 ACTFEL Device Structures

Depending on whether a device emits a single color or multiple colors, ACTFEL devices can be categorized into two types: monochrome devices and multi-color devices. In this dissertation, only monochrome green devices were involved. A complete ACTFEL device generally has a multi-layer structure of *substrate/bottom conducting layer/bottom dielectric layer/phosphor layer/top dielectric layer /top conducting layer*. Sometimes, this ACTFEL device structure is also referred to as MISIM (metal-insulator-semiconductor-insulator-metal). The most important layer of all these layers is the phosphor layer, which is sandwiched by two (isolated) conducting layers at each side to allow a voltage to be applied across it. For the alternating current thin film electroluminescent devices, the dielectric layer(s) is required to limit the current passing through the phosphor layer. Each of them is inserted between the phosphor layer and the conducting layer. Depending on which side is transparent, an EL device structure can be categorized into two: the standard device structure and the inverted device structure as shown in Figure 2-1. When the substrate and the two bottom layers are transparent, the light emitted from the phosphor comes out from the substrate side and the viewing direction is from the phosphor layer to the substrate side. In this research, the standard device structure is glass/ITO/ATO/phosphor layer/BTO/Al. Glass is used as a transparent substrate, ITO is a transparent bottom conducting layer, ATO is a transparent bottom dielectric layer, BTO is a transparent top dielectric layer, and opaque metal Al is bottom conducting layer, which also acts as an optical reflector. If any of the bottom layers are not transparent, the top layers are required to be transparent. This latter structure is called the inverted structure and the emitted light is viewed from the top layers. In this research, the inverted device structure is Al_2O_3/Au/Pb(ZrTi)O_3/phosphor layer/BTO/ITO. Since

the opaque Al_2O_3 substrate together with Au conducting layer and $Pb(ZrTi)O_3$ dielectric layer is not transparent, the transparent dielectric layer BTO and transparent conducting layer ITO are used for the top layers. In either of the two structures, the layers at one side of the phosphor layer are transparent and the layers at the other side are opaque so that the light can be viewed at the transparent side. So-called "half-cell" structures, containing only one dielectric layer, are typically used for research. The general rule is that brightness in the "half-cell" structure device is half of that in the "full-cell" complete structure device.

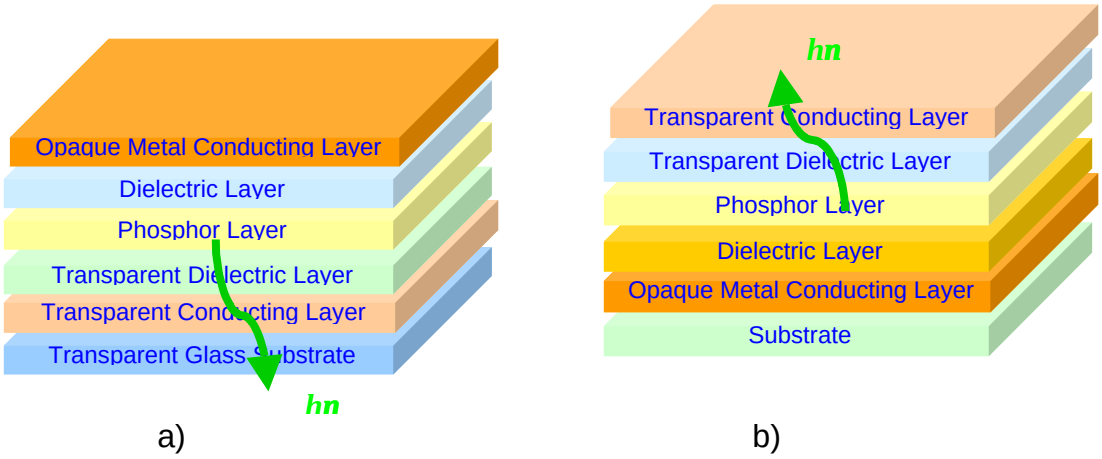

Figure 2-1 ACTFEL device structures: a) Standard and b) Inverted[16]

2.3 Optical and Electrical Characterization of ACTFEL Devices

2.3.1 Brightness

An ACTFEL device is operated by applying high voltage pulses of alternating polarity. Any waveform of alternating polarity may be used, including sine waves, triangle waves, square pulses, and trapezoidal pulses, with the applied voltage specified

as the maximum voltage per pulse, rather than the RMS value.[18] Frequency for the alternating polarity may vary from 60 Hz to from 1 to 2.5 kHz. Generally, there is a voltage threshold above which a significant amount of light is produced. The plot of brightness as a function of voltage is known as a B-V curve. Devices often are compared by the value of brightness at 40 V above this threshold, and this value is called the B_{40} value. These data are generally plotted on a linear scale. Typical data from an ACTFEL device is shown in Figure 2-2. There are several common methods for determining the threshold voltage. The most frequently used method involves finding the highest slope of the B-V curve, then extrapolating this slope back to the voltage axis. This has the advantage of defining the portion of the B-V curve relative to the voltage at which rapid turn-on occurs.

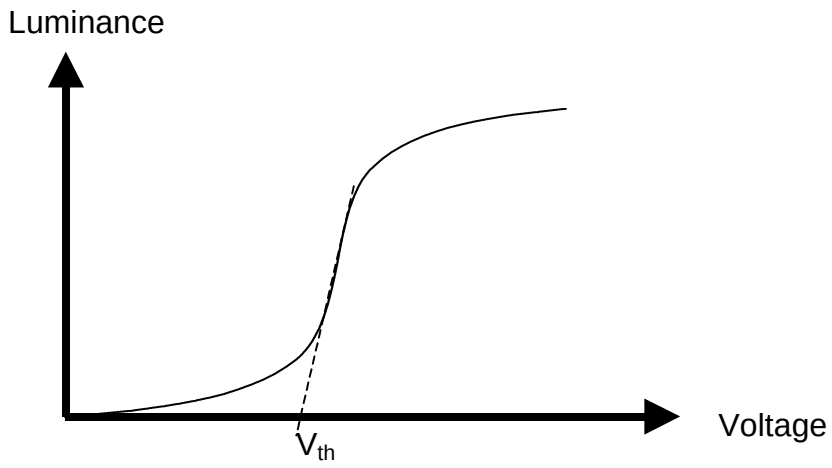

Figure 2-2 Typical B-V curve of ACTFEL devices showing the extrapolation method for determining V_{th}

Finally, electrical characteristics are often used to define threshold. This is done most often with Q-V and C-V curves, which are discussed in Section 3.6.1.4. The electrical

turn-on obtained from Q-V often corresponds closely with the optical turn-on obtained from B-V.

2.3.2 Chromaticity

Quantitative methods for evaluating chromaticity and colorimetrics were developed that are standard to the entire display community. These methods involve relating the spectral distribution of the phosphor to values that correspond to the color seen by an observer. The most commonly used standard is that established by Commission Internationale de l'Eclairage (CIE), which defines chromaticity using three unitless values (x, y and z CIE coordinates) that can be plotted on a two-dimensional graph (since z = 1-x-y), known as the CIE diagram. These plots offer a convenient quantitative comparison of the color of different phosphors.[19] Under the additive mixing rule, any color can be reproduced by adding the three primary colors (tristimulus values.) The CIE system uses monochromatic sources as the primary colors for blue (λ= 435.8cm), green (λ= 546.1nm) and red (λ= 700nm). The R, G and B tristimulus cuves are denoted as x, y and z, and are shown in Figure 2-3. Color is determined by calculating X, Y and Z values, such that

$$X = K_m \int_{380}^{780} \Phi_{e\lambda} \bar{x}(\lambda) d\lambda$$

$$Y = K_m \int_{380}^{780} \Phi_{e\lambda} \bar{y}(\lambda) d\lambda$$

$$Z = K_m \int_{380}^{780} \Phi_{e\lambda} \bar{z}(\lambda) d\lambda$$

where K_m is the luminous efficiency coefficient which is 680 lm/W, $\Phi_{e\lambda}$ is the spectral output of the source, λ is the wavelength and $\bar{x}(\lambda)$, $\bar{y}(\lambda)$ and $\bar{z}(\lambda)$ are the spectral response of the standard observer for each of the three primary colors: red, green and blue.

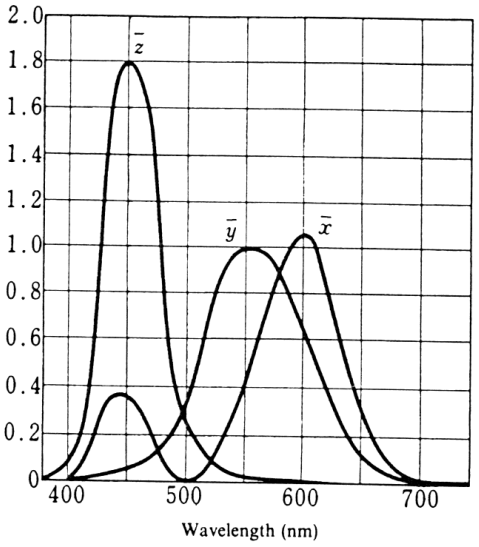

Figure 2-3 Red (x), green (y), and blue (z) tristimulus curves[19]

The chromatic coordinates are then found from

$$x = \frac{X}{X + Y + Z}$$

$$y = \frac{Y}{X + Y + Z}$$

$$z = \frac{Z}{X + Y + Z}$$

Two chromaticity values are traditionally expressed as x and y. The x and y values are plotted on the CIE diagram, shown in Figure 2-4. The curved perimeter of the CIE diagram, which spans from blue to red, is defined by single wavelengths and represents completely saturated colors. Any broadening of the emission spectrum results in

coordinates inside these boundaries and toward the center or “white” region of the diagram.

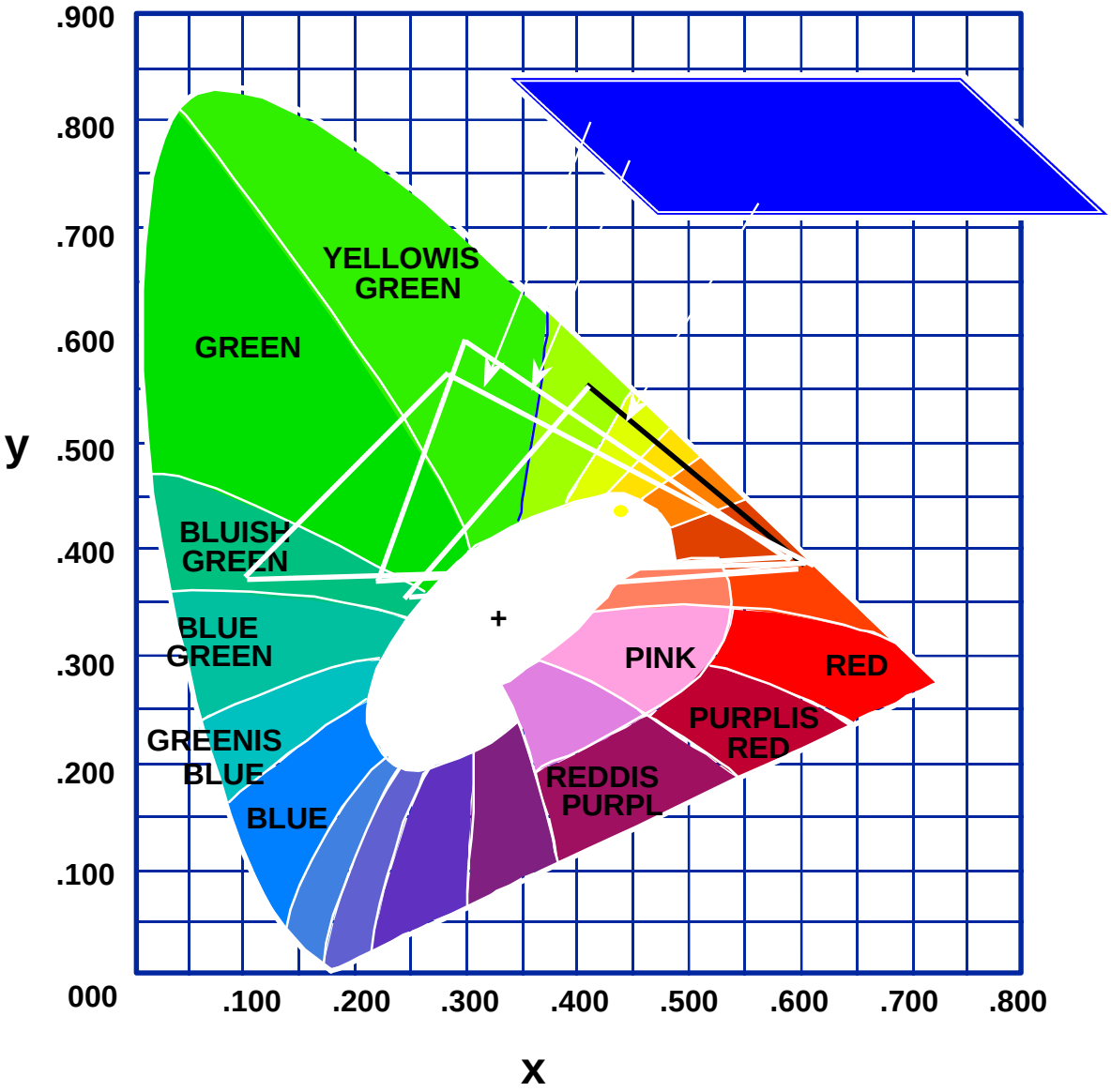

Figure 2-4 1931 Commission de L’ Eclariage chromaticity diagram[16]

2.3.3 Electrical Behavior – Ideal Circuit Model

Interpretation of the electrical characteristics of an ACTFEL device is aided by considering an equivalent circuit model. Below threshold, the device can be modeled

accurately by considering the insulators and the phosphor layer as series capacitors. The two insulators can be combined numerically by treating them as series capacitors and can be considered as a single ideal capacitor. At a certain threshold voltages, rapid turn-on occurs where a real current flow through the phosphor layer, sometimes called conduction or dissipative current (as opposed to the charging current which charges the capacitors and is discharged on removal of the applied voltage). In an ideal device, the dissipative current is stored until an opposing pulse is applied and the current flows in the opposite direction. Using the procedure described by Ono,[16] the device can be modeled as a circuit where the phosphor layer is modeled as a parallel capacitor and nonlinear resistor. The nonlinear resistor has the current-voltage characteristics shown in Figure 2-5. The nonlinear resistor often is modeled as a set of back-to-back Zener diodes. The derivation of the following characteristics is given in more detail by Ono,[16] but results of the circuit analysis are presented here. Below threshold, the applied voltage is distributed capacitively by the phosphor and the insulators giving

$$V_P = \frac{C_I}{C_I + C_P} V_a \qquad (2\text{-}1)$$

$$V_I = \frac{C_P}{C_I + C_P} V_a \qquad (2\text{-}2)$$

where V_a is the applied voltage, V_I and V_P are the voltages across the insulator and the phosphor layer, respectively. C_I and C_P are the insulator and phosphor capacitance, respectively. C_I is the combination of C_{i1} and C_{i2}, given by $C_{i1}C_{i2}/(C_{i1}+C_{i2})$ since they are connected in series. When $C_{i1} = C_{i2}$, which is the symmetric device case, $C_I = C_i/2$. Above the threshold, the resistive portion of the phosphor circuit allows current to flow (conduction current) until the voltage across the phosphor returns to threshold. At the

same time, the conduction current must be balanced by capacitive current which will charge the insulating capacitors to maintain the overall voltage across the device. Therefore, the final voltages above threshold are

$$V_{P,f} = V_{P,th} = \frac{C_I}{C_I + C_P} V_{th} \qquad (2\text{-}3)$$

$$V_{I,f} = V_a - V_{P,f} \qquad (2\text{-}4)$$

Here the concept of field clamping is apparent. Voltage across the phosphor layer in this simple equivalent circuit model is maintained at the threshold voltage regardless of the applied voltage. The amount of dissipative charge transferred through the phosphor, as required to maintain the applied external voltage, is

$$Q^{ext} = 2C_I V_{I,f} = 2C_I (V_a - V_{th})$$

and the interface charge density at the end of a pulse is half this value. (The circuit model represents a perfectly symmetric device. Therefore, the other half of the transferred charge neutralized the previous interface charge.) Using this value for transferred charge along with the voltage transferred from the phosphor to the insulators, the power consumption density is found to be

$$P_{in} = 2Q^{ext} V_{p,th} = 4 f C_I (V_a - V_{th}) V_{p,th} \qquad (2\text{-}5)$$

where *f* is the drive frequency. The luminous efficiency ηis the brightness, L, divided by the power consumption, given by

$$\boldsymbol{h} = \frac{L}{P_{in}} = \frac{L}{4 f C_I (V_a - V_{th}) V_{p,th}}$$

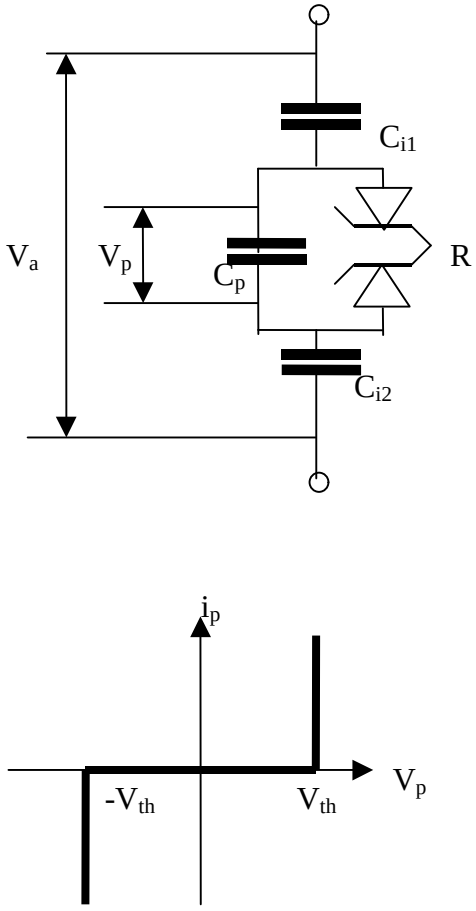

Figure 2-5 Equivalent circuit for an ACTFEL device showing the current-voltage characteristics of the non-linear resistor[16]

2.4 Device Physics

The physical processes of electroluminescence can be broken down into several steps: (1) injection of electrons into the conduction band, (2) acceleration of a fraction of the electrons to ballistic energies due to the applied field, (3) impact excitation of the luminescent centers by electrons with sufficient energy, (4) radiative relaxation of the centers (in competition with non-radiative relaxation), and (5) outcoupling of the generated photons. These processes are shown schematically in Figure 2-6. Electrons are

generated at the interface between the phosphor layer and dielectric layer. The vertical axis stands for the energy *E*. When a voltage drop is applied through the phosphor layer, the band-gap is tilted from the cathode side of the phosphor layer to the anode side. Electrons from the interface are accelerated under this electric potential, subsequently exciting luminescent centers in the phosphor. An additional process which can occur is (3b) impact ionization of the lattice or of defects by electrons, which is also shown in Figure 2-6. In the following paragraphs, these processes will be discussed in more detail.

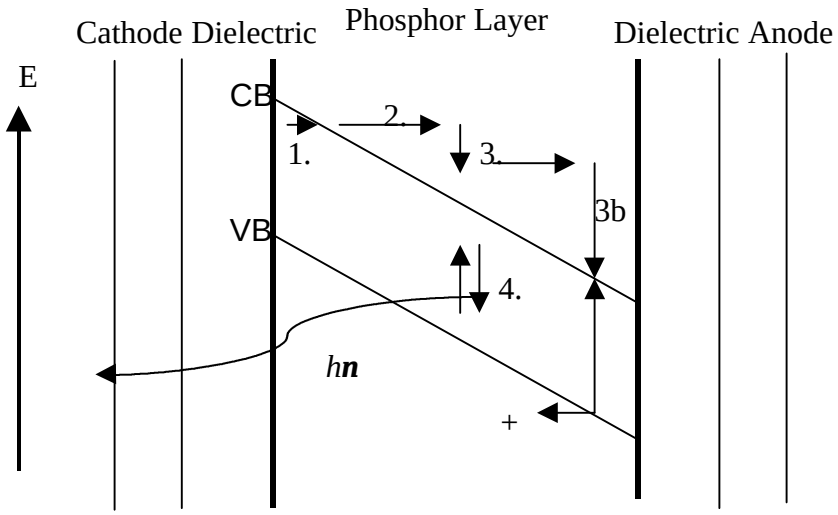

Figure 2-6 Electroluminescence process of ACTFEL device

2.4.1 Electron Injection

The source of charge carriers under steady state operation is generally accepted as being primarily from interface states for ZnS:Mn devices.[20] The depth and concentration of available interface states has been shown to change significantly when the dielectric was changed. When the local electric field at the cathode reaches threshold level, charge injection takes place. Among the possible mechanisms responsible for injection of electrons into the conduction band are thermionic emission, pure tunneling, and phonon-

assisted tunneling.[21] At room temperature and for trap depths of 1.5eV, pure tunneling is the dominant injection mechanism among the three. The expression for the emission rate from pure tunneling is:

$$e_n^{PT} = \frac{qf_p}{4(2m^* E_{it})^{\frac{1}{2}}} \exp[(-\frac{4}{3}\frac{4(2m^*)^{\frac{1}{2}} E_{it}^{\frac{3}{2}}}{q\hbar f_p})(1-(1-(\frac{\Delta E_{it}}{E_{it}})^{\frac{5}{3}}]$$

where q is the electronic charge, f_p is the electric field in the phosphor, m^* refers to the electron effective mass, E_{it} is the interface trap depth, $\boldsymbol{D}E_{it}$ is the coulombic barrier lowering and h is Planck's constant. If the electron injection is a result of the pure tunneling effect, its emission rate should be independent of temperature. However, a weak temperature dependence is observed.[22] Therefore, the more accurate way to explain the electron injection is the phonon-assistance tunneling which is a combination of the first two mechanisms, where phonon interactions allow efficient tunneling.

2.4.2 Charge Transport

Charge transport in a high electric field, as is the case in ACTFEL devices, has been studied extensively. A critical issue is the efficiency with which charge carriers are able to gain sufficient energy to impact excite the luminescent centers without loss. Two methods have been used to calculate the characteristics of high field electronic transport in ZnS. The goal of the calculations is to determine the fraction of electrons that are able to excite luminescent centers. One involves the use of band structure calculations and Monte Carlo simulations, in which independent probabilities for scatting events are used to determine the fate of a large number of carriers.[3, 23, 24, 25] The second technique is the

lucky-drift transport model.[26] This is an analytical model in which the mean free path for electrons is analyzed with respect to scattering events.

In the first theory, the assumption is made that "all electrons are hot" at a high field of ~1MV/cm, and ballisitic or nearly loss-free acceleration was predicted.[26] This theory explained the avalanche breakdown observed in ZnS ACTFEL devices. In the second theory, two transport modes are considered. One is ballistic transport, which is collision-free. The other is the drift mode, which occurs after the electron has had one collision, which increases the probability of subsequent collisions. This theory explained the ACTFEL devices with poor crystallinity.[26]

2.4.3 Impact Excitation and Ionization

Impact excitation and ionization are two parallel processes that occur in the phosphor device. The primary process involved in excitation in ZnS:Mn devices is direct impact excitation,[26] in which the energy threshold for the process is essentially the transition energy for the luminescent center.[26] The probability for this process is determined by the impact cross section of the luminescent center, and the average impact length for an electron is found from $l_l = (\sigma N)^{-1}$ where σ is the impact cross section in units of cm^2 and N is the concentration of centers in units of cm^{-3}. This cross-section has been estimated experimentally by Mach and Mueller to be 4.0×10^{-16} cm^2 (+/-20%) for Mn^{2+} in ZnS, which is near the value of the ionic cross section.[3] Another possible excitation process is impact ionization followed by electron recapture and radiative relaxation. This is believed to be the dominant process involved in excitation of Eu^{3+} in ZnS. There may be other excitation mechanisms, such as energy transfer from electron-

hole pairs to luminescent centers,[20] which has been suggested to account for excitation of Tb^{3+}. Direct impact ionization of the lattice can occur if electrons reach sufficient energy. The energy threshold is normally thought to be either the bandgap of the host material[23, 14] or 1.5x this value.[27]

2.4.4 Radiative Decay

When an impurity center is in an excited state, that energy will eventually be dissipated. The relaxation process can occur by either 1) emission of a photon, b) non-radiative relaxation, which can be in the form of emission of one or more phonons to the lattice etc, or c) energy transfer to another center. For display applications, it is desirable to maximize the first process and to minimize the second. The third case can be useful or harmful in different situations.[28] For a simple two-level system, the rate of return from an excited state to the ground state is given by

$$\frac{dN_e}{dt} = -N_e P_{eg}$$

where N_e is the number of luminescent ions in the excited state, t is the time and P_{eg} is the probability of spontaneous emission from the excited to the ground state. Integration yields

$$N_e(t) = N_e(0)\exp(\frac{-1}{\boldsymbol{t}_R})$$

where $\boldsymbol{t}_R$ ($=P_{eg}^{-1}$) is the radiative decay time, and the exponential decay of intensity results.[28] An excited ion can relax through the emission of phonons by coupling to an electromagnetic vibration or the lattice vibration. Because the probability of this process

is an Arrhenius dependence on temperature, the decrease in probability of photon emission with temperature is known as thermal quenching.[20]

2.4.5 Optical Outcoupling

Optical outcoupling is dependent on the internal reflection angle. For a useful device, generated photons must escape the device in the direction of the viewer, so the concept of internal reflection angle must be considered. When light with incidence angle θ_1 passes from one media n_1 to the less dense media n_2, the deflection angle θ_2 is determined by the following equation:

$$n_1 \sin\boldsymbol{q}_1 = n_2 \sin\boldsymbol{q}_2$$

When the deflection angle θ_2 reaches its maximum 90^o, no deflection will occur and all the light will be reflected and confined in the media 1. Since in most cases the media 2 is normally air or vacuum, the refraction index of n_2 is assumed as 1.00. According to the above equation, the critical incidence angle θ_c is given by:

$$\boldsymbol{q}_c = \arcsin(\frac{1}{n_1}) \qquad (2\text{-}6)$$

When all the possible incidence angles lower than the critical angle are considered, the light that can be deflected out of the phosphor layer is given by:

$$\boldsymbol{h}_{opt} = \int_0^{ar\sin(\frac{1}{2.4})} \sin\boldsymbol{q} d\boldsymbol{q} = 1-(1-(\frac{1}{2.4})^2)^{05} \approx 0.1$$

The optical outcoupling efficiency can be improved by increasing the surface roughness and thereby reducing internal reflection. It has been shown that a rough surface can

increase outcoupling by more than on order of magnitude.[29] However, too rough a surface can reduce contrast because of increased diffuse scattering.[16]

2.5 ACTFEL Materials

As mentioned earlier, three different materials are involved in an ACTFEL device: the phosphor materials, the dielectric materials (also called insulators), and the conducting materials (also called electrodes). These three different materials, as well as substrate, are discussed separately here according to their individual function.

2.5.1 Substrates

For a standard device, the primary requirements for the substrate are transparency, smooth surface and the ability to withstand thermal treatments required by subsequent layers. It is also desirable that the material be inexpensive. For these reasons, the most common substrate material is Corning 7059 soda-lime-silicate glass. This is an alkali-free, barium bororsolicate glass often used for LCD substrates (J-47). It has a softening temperature of ~600^{o}C, and large panels can undergo rapid thermal anneals (RTAs) of up to 650^{o}C without significant damage or warping.[30] For research purposes, smaller samples of 2”x 2” in size may be subjected to RTAs up to 850^{o}C without significant damage. In addition Corning 7059 is alkali-free to prevent migration of such species into the device. For higher temperatures, glass-ceramics are available which meet the substrate requirements, but these materials are too expensive to be economically viable substrate materials for commercial applications. Glass substrates were used for the standard device structures in this research.

The substrate requirements for the inverted structure devices also include a smooth surface and the ability to meet the thermal considerations for processing of subsequent layers. For the inverted structure, the substrate could act as part of the device, comprising the bottom insulator, and electrical properties must be considered. These are discussed in Section 2.5.3. For devices with the structure in which the bottom electrode is deposited on the top of the substrate, alumina substrates have also been used.[31] For active matrix applications, the on/off state of the pixels are controlled by transistors located underneath each pixel, and the silicon-based IC array is used as the substrate.[16] In this research, opaque polycrystalline Al_2O_3 substrate was used for the inverted device structure since it can withstand much higher processing temperature than glass.

2.5.2 Electrodes

Two kinds of electrode materials are used for ACTFEL devices: transparent electrodes and opaque electrodes.

2.5.2.1 Transparent Electrodes

The transparent electrode layer is used to allow emitted light to be viewed. Three critical materials requirements for transparent electrode are: 1) it must be sufficiently conductive; 2) it much be as transparent as possible in the spectral region of the emission from the device to minimize absorption and/or color perturbation; 3) it must withstand the thermal processing of subsequent layers. The material most commonly used for this application is indium-tin-oxide (ITO).[16] This is normally an alloy of 90 wt% In_2O_3 and 5~10% wt% SnO_2, sometimes doped with F. An ITO thickness of 200nm is typical. Good transparency (90%) can be obtained at this thickness with a resistivity of ~1x 10^{-4}

Ω-cm, providing a resultant sheet resistance of ~5Ω/square. The primary cause for high conductivity in ITO is oxygen deficiencies, since oxygen vacancies act as shallow donors which are efficiently ionized at room temperature.[32] Oxygen vacancy concentrations can be affected by annealing at high temperature. Another transparent conductor commonly used in the inverted structure is ZnO:Al.[33]

2.5.2.2 Opaque Electrodes

For the standard structure, the requirements for the opaque electrode are not stringent because it is the last layer deposited. The critical materials requirements for opaque electrodes are: 1) it must have sufficient conductivity, which for most metals is far better than that of the transparent electrode, and 2) good adhesion to the top insulator is also critical. Aluminum is the most common electrode material for several reasons. First, it is inexpensive. Second, it is easily deposited by evaporation or sputtering. Third, it has a low melting temperature and exhibits desirable wetting characteristics to many common insulator materials, providing the possibility for self-healing breakdown by fusing of the metal surrounding a short. The typical thickness for this layer is 100~200 nm. One tradeoff to be considered for Al as an electrode is its high reflectivity, which enhances brightness but reduces the contrast in a display. For inverted structures in which the electrode is deposited on the bottom of the phosphor layer, other metals such as Au, Mo, Ta and W are candidates besides aluminum.

2.5.3 Insulators

The insulating layers of an ACTFEL device are an integral part of the capacitive nature of the device, as seen in the equivalent circuit model in Section 2.3.3.. The bottom

insulator undergoes the same thermal processing as the phosphor layer and therefore must have thermal stability and chemical compatibility with the bottom electrode and phosphor layer in addition to good adhesion. The most important electrical requirements are that this insulator prevents current flow through the device and withstands electrical breakdown under the potential fields used in the device, usually up to 2MV/cm. In addition, the characteristics of the phosphor-insulator interface affect the depth and concentration of interface states[34] and therefore significantly influence device performance. Critical properties for reliable, efficient performance are as follows[16]:

1. High dielectric constant $\varepsilon_o\varepsilon_r$;
2. High dielectric breakdown electric field, F_{BD}
3. Small number of pinholes and defects
4. Good adhesion
5. Small loss factor, tanδ.

ε_o and ε_r are the dielectric constant of vacuum and the relative dielectric constant of the insulating layer, respectively. tanδ is a measure of the dissipative characteristics of the capacitor and is equal to $1/(2\pi fRC)$, where f is the frequency, R is the resistance and C is the capacitance of the insulating layer.

In order to optimize the insulating layers for device efficiency, it is useful to go back to the electrical behavior using the relationships presented in Section 2.3.3.. Equation 2-1 and 2-2 show that the proportion of the voltage which is across the phosphor is governed by the relative capacitance of the phosphor and insulating layers. To maximize the portion of the applied voltage dropped across the phosphor layer, the

capacitance of the insulators should be maximized while that of the phosphor is minimized. The insulator and phosphor capacitances are determined by the equation

$$C = \varepsilon_o \varepsilon_r \frac{A}{t} \qquad (2\text{-}7)$$

where t is the layer thickness. It is apparent that to optimize the insulator capacitance, either the dielectric constant should be maximized as noted in the above list of attributes, or the layer thickness should decrease. Indeed it is useful to minimize the insulator thickness in a device. However, a lower limit on thickness is set by two factors. The first is the third attribute in the list of characteristics, namely a small number of defects and pinholes. The thinner the insulating layer the larger the probability of having defects and pinholes in the film. This is primarily a processing issue and careful process control can minimize the problem. The second limitation is the breakdown electric field strength, also noted in the above list. The second limitation is the electric field strength, E = V/t. For a fixed voltage, the thinner the dielectric film is, the higher the electric field strength and the greater the chance of dielectric breakdown.

Generally speaking, it has been observed that materials with a higher dielectric constant have a small breakdown strength, and vice versa. In addition, the high dielectric constant materials tend to exhibit propagating breaking, meaning than small defects lead to catastrophic failure . The typical dielectric materials used are $BaTa_2O_6$ (BTO), $PbTiO_3$, $BaTiO_3$, SiN_x, SiON. Two insulating materials used for this research were ATO and PZT. ATO is made of $(Al_2O_3/TiO_2)_n$ multilayers grown by atomic layer epitaxy.[35] By replacing Zr for Ti in $PbTiO_3$, $Pb(Zr_{0.5}Ti_{0.5})O_3$ (PZT) was used as an insulating layer. The dielectric properties of ATO and PZT are listed Table 2-1 for comparison.[36]

2.5.4 Phosphors

2.5.4.1 Hosts

The host is, by its definition, the host material for the luminescent centers. A critical consideration for the host material is its bandgap characteristics.

Table 2-1 Parameters of dielectric materials ATO and PZT

Dielectric parameters	ATO ($(Al_2O_3/TiO_2)_n$)	PZT ($Pb(Zr_{0.5}Ti_{0.5})O_3$)
Dielectric constant ε_r	Al_2O_3 8 TiO_2 60	$PbTiO_3$ 150~1700
Electric breakdown strength	Al_2O_3 5~8 MV/cm TiO_2 0.2 MV/cm	$PbTiO_3$ 0.5 MV/cm

It should satisfy the following several criteria:

1. The host bandgap must be large enough not to absorb any emission from the luminescent center. For complete visible transmission, this requires a band gap of at least 3.1eV.
2. The host must be a good insulator below threshold. This is required to maintain a voltage drop and subsequent electric field across the phosphor layer, leading to the sub-threshold capacitive nature of the phosphor.
3. The host must have a high breakdown strength to allow for efficient acceleration of electrons. This requires that the breakdown field of the phosphor must be at least 1 MV/cm.
4. The host must have good crystallinity and a low phonon-coupling coefficient to minimize electron scattering.

5. The host must provide a suitable substitutional lattice site for the luminescent center.

These requirements have historically been met best by sulfur- and oxide-based compounds. The typical sulfur-based hosts are ZnS, SrS, CaS, $SrGa_2S_4$ and $CaGa_2S_4$.[1, 10, 37, 38] The typical oxide hosts are Zn_2SiO_4, $ZnGa_2O_4$, Zn_2GeO_4, Ga_2O_3.

Since the band gap of host materials for ACTFEL devices is generally wider than that of Si or III-V semiconductors, EL phosphor materials are also called wide-gap semiconductor materials. The band-gap of ZnS and Zn_2GeO_4 together with that of Si[39] is listed in Table 2-2.

Table 2-2 Typical wide band-gap semiconductor host materials[16, 40]

Semiconductor Materials	Si	ZnS	Zn_2GeO_4
Bandgap	1.12eV	3.4eV (Zincblende) 3.6eV (Wurtzite)	4.4eV (Rhombohedral)

2.5.4.2 Luminescent Centers

The spectral properties, and to a large extent the temporal properties, of optical emission are primarily influenced by the activator impurity in the phosphor. There are two types of luminescent centers commonly used in phosphor applications. In many lamp and CRT phosphors, luminescence results from recombination of electrons and holes trapped in deep donor and deep acceptor levels, respectively. This class of luminescent center is not used in ACTFEL devices because the electron-hole pairs are unstable under high fields and the luminescence is effectively quenched.[16, 41] The second type of center

uses localized transition between electronic states of an isolated dopant ion. This dopant ion is typically either a transition metal such as Mn^{2+}, Cr^{2+}, Ti^{4+}, Cu^{+}, Ag^{+}, a rare earth ion such as Eu^{3+}, Eu^{2+}, Ce^{3+}, Tb^{3+}, or Tm^{3+}, or an S^{2} configuration ion such as Pb^{2+} or Bi^{3+} .[16, 28] One characteristic of importance in terms of both understanding the luminescent process and for application to displays is the radiative decay time. The decay time is determined primarily by two selection rules related to the electronic configuration of the ground and excited states, as well as the surroundings of the ion.[28] One of these selection rules is referred to as the parity selection rule, which forbids transitions between levels of the same parity, i.e. transitions within the d shell, within the f shell, or between the d shell and s shell are forbidden. The other selection rule is the spin selection rule, which forbids transition between configurations with different spin states. Forbidden transitions have longer decay time.[28]

The transition metal ions mentioned above all have a d^{n} valence configuration and their emission spectra are all characteristic of intra-shell d-d transitions. They are therefore all forbidden by the parity selection rule,[28] and their emission is usually broad band. Therefore, decay times for the transition metal can be in the range of 100μs to several ms, depending on the spin selection rule and symmetry. Another general characteristic of the transition metal activators is that because the transitions originate in the valence d-shell, they are strongly influenced by the crystal field and ligand fields of the host. The crystal field modification of Mn^{2+} by the host will be discussed in more detail in Section 2.7.4..

There are two very different types of transitions observed for rare earth ions. The first is observed in Ce^{3+} and Eu^{2+} in which the ground state configurations have a *4f*

valence. The excited states have one or more electrons promoted to the 5d orbital, which is strongly affected by the surroundings and symmetry of the ions. The second type of rare earth transition is an intra-shell 4f-4f transition. This type of transition is seen in Eu^{3+}, Tb^{3+}, and most other trivalent rare earths. These transitions are all parity forbidden and have decay times typically of several ms. The spectra are characterized by line transitions, and are insensitive to the surroundings and symmetry of the ion since the *4f* electrons are shielded by the *6s* orbital.

2.5.4.3 Host-Center systems

In addition to considering the electrical properties and processing conditions of the host and the luminescent properties of the center, one must consider the compatibility and interrelationships between the two. Size mismatching of the activator on the cation site is important, as is the valence match (or mismatch) with the host. For the case of ZnS:Mn, the ion size (Zn^{2+} is 0.60Å, Mn^{2+} is 0.66Å), the valence (both are 2+) match well. For the case of ZnS:Tb, the ions size of Tb^{3+} 0.92 Å is much larger than that of Zn^{2+}. Besides, Tb^{3+} leaves one positive charge after it substitutes for Zn^{2+}. In this case, Ag^{+} or F^{-} ions are used to compensate the charge.

In terms of the host material, there are two categories of phosphors: sulfides and oxides. Green phosphors include ZnS:Mn (optically filtered), ZnS:Tb, CaS:Ce , SrS:Ce and CaS:Ce in the sulfide based materials,[17] and Zn_2SiO_4:Mn, Zn_2GeO_4:Mn, $ZnGa_2O_4$:Mn and Ga_2O_3:Mn in the oxide based materials.[42] Among the sulphide phosphors, the highest brightness and efficiency is obtained in ZnS:Tb. Among the oxide phosphors, Zn_2SiO_4:Mn demonstrates the highest brightness. More details about

Zn_2GeO_4:Mn and ZnMgS:Mn will be discussed in Section 2.6. and Section 2.7 respectively.

Table 2-3 Performance of green ACTFEL devices using sulfide and oxide phosphor materials

	L (cd/m^2) 60Hz (1kHz)	η (lm/W) (1kHz)	CIE(x,y)
Sulfide-based	L_{40}	η_{40}	
ZnS:Mn filter	160	1.0	0.65,0.35
ZnS:Tb,F	125 (2100)	05~1.0	0.30,0.60
CaS:Ce	10 (150)	0.1	0.27,0.52
SrS:Ce	65 (900)	0.44	0.19,0.38
ZnMgS:Mn[43]	(325)		0.35,060
Oxide-based[42]	L_{max}	η_{max}	
Zn_2SiO_4:Mn	230 (3020)	0.78	0.251,0.697
Zn_2GeO_4:Mn	39 (341)	0.25	0.263,0.683
$ZnGa_2O_4$:Mn	235 (758)	1.2	0.082,0.676
Ga_2O_3:Mn	227 (1018)	1.7	0.198,0.654

2.6 Zn_2GeO_4:Mn ACTFEL Devices

2.6.1 General Consideration of Oxide Phosphors

The most widely used phosphor host materials in ACTFEL devices are sulfide compounds.[16,1] Requirements for the phosphor layer in ACTFEL devices were discussed in Section 2.5.4.1. Among these requirements, the need for efficient transport of high energy electrons and the need for good crystallinity have limited the interest in oxides as potential EL phosphors.[16] Empirically, oxides have larger band gaps than sulfides and are not as capable of transporting significant current densities of hot electrons.[16] Efficient host materials for ACTFEL phosphors are generally limited to those materials with bandgap energies in the range of 3.5~4.5 eV. Oxides tend to be more refractory than

sulfides and achieving good crystallinity at processing temperatures compatible with glass substrates (~550 °C) is difficult or impossible with most oxide phosphors.[42]

Renewed interest in oxide ACTFEL phosphors has stemmed from progress made in alleviating both of these limitations. In terms of the current transport, much recent work in oxide phosphors has been focused on materials with moderate band gaps such as Ga_2O_3 (4.52-4.84 eV),[44] $ZnGa_2O_4$ (4.3eV),[45] and Zn_2GeO_4:Mn (4.68eV).[46])

2.6.2 Green Oxide ACTFEL Devices

Typical green phosphors used for ACTFEL devices are $ZnGa_2O_4$:Mn,[47] Zn_2SiO_4:Mn, Zn_2GeO_4:Mn, $Zn_2Ge_xSi_{1-x}O_4$:Mn, and GaO_3:Mn. The color of $ZnGa_2O_4$:Mn EL emission is the closest to the standard green color (546.1 nm). The highest brightness was obtained in Zn_2SiO_4:Mn, with a value of 5000 cd/m^2 achieved at a drive frequency of 1 kHz.[42] Ga_2O_3:Mn EL devices demonstrated the lowest threshold voltage of 110V at a thickness of 1μm.[42] The lowest processing temperature for a green oxide phosphor is observed for Zn_2GeO_4:Mn, with a value of 650^{o}C. Limited by processing constraints, Zn_2SiO_4:Mn crystallinity is poor due to its high crystallization temperature. By substituting Ge for Si, $Zn_2Ge_xSi_{1-x}$O4:Mn demonstrated the best performance of all green oxide phosphors due to improved crystallinity.[42]

RF sputtering deposition has been frequently used to produce oxide ACTFEL devices. RF sputtering deposition of a variety of oxide ACTFEL devices was reported by Minami, et al.[42] These films were deposited at 250^{o}C on a 0.2mm $BaTiO_3$ sheet and annealed at 700~1100 ^{o}C for 5 hrs. in Ar. The unique characteristic of this deposition is the use of the $BaTiO_3$ substrate which acted as both substrate and insulating layer.

$BaTiO_3$ can be annealed at much higher temperature than typical glass substrates. However, this large 0.2mm thickness reduced the capacitance of the $BaTiO_3$ sheet, in accordance with the equation $C = \varepsilon_o\varepsilon_r A/t$. Smaller capacitance in the insulating layer lowers the voltage drop across the phosphor layer, according to the equation $V_p = C_{in} /(C_p + C_{in}) * V_a$. Fortunately, $BaTiO_3$ has a dielectric constant of over 1500, which can compensate for the large thickness required for a substrate.

Other growth techniques for oxide phosphors include dip-coating, sol-gel and pulsed laser deposition. Dip-coating was reported to show a better performance than sputtering deposition for the oxide ACTFEL devices. Sol-gel processing has been reported only for powder $ZnGa_2O_4$:Mn EL devices. Pulsed laser deposition of $ZnGa_2O_4$:Mn deposited on a single-crystal substrate was report by Norton et al.[48] Single-crystal substrate MgO_2 was used for high temperature processing in order to obtain better crystallization of the $ZnGa_2O_4$:Mn layer. The films were deposited at substrate temperatures from 250^{o}C to 800^{o}C. Photoluminescence was obtained from the film at 540nm. It was found that the PL intensity was more strongly dependent on crystallinity rather than surface roughness. Zn deficiency in the phosphor gwas found to be dependent on the substrate temperature. However, use of a $ZnGa_2O_4$ target containing extra Zn showed worse PL performance.

2.6.3 Zn_2GeO_4 Host Crystal Structure

This research particularly focused on the green oxide phosphor Zn_2GeO_4:Mn. As presented in Section 2.5.4.3., host materials accommodate the luminescent centers. For the case of Zn_2GeO_4:Mn, Mn^{2+} should replace Zn^{2+} to incorporate into the Zn_2GeO_4 host.

There are two types of Zn^{2+} positions available in the Zn_2GeO_4 reverse spinel structure, tetrahedral and octahedral. In the regular spinel structure, the two Zn^{2+} ions in the primary Zn_2GeO_4 unit are located in octahedral positions and one Ge^{4+} ion is in a tetrahedral position. In the reverse spinel, one Zn^{2+} is in an octahedral position, the other one in a tetrahedral site, and the Ge^{4+} is in an octahedral position. The tetrahedral and octahedral position of Zn^{2+} are shown in the Figure 2-7. The octahedral position is only shown with a quarter of its volume, while the other three quarters are in other primary unit cells. Transition of Mn^{2+} is allowed only when it is in an octahedral symmetric position. No transition of Mn^{2+} is allowed when it is in a non-symmetric tetrahedral position.[16]

2.6.4 Pulsed Laser Deposition of Oxide Thin Films

Pulsed laser deposition has been used for oxide materials for some time, especially for oxide superconducting materials such as $Yba_2Cu_3O_{7-x}$.[49, 50, 51] Pulsed laser deposition has unique advantages, including film stoichiometry close to that of the target, low contamination level, high deposition rate and non-equilibrium processing. Pulsed laser deposition of phosphor materials have been reported such as $ZnGa_2O_4$:Mn presented above and Y_2O_3:Eu. [52, 53] The interaction of the laser with the target and plasma during pulsed laser ablation can be broken down into four regimes: 1) Interaction of incident laser with the target resulting in ablation of target surface; 2) Interaction of the ablated materials with laser resulting in formation of plasma. 3). Expansion of the plasma. and 4) Interaction of the plasma with background gas resulting in formation of interaction plume right above the target. The first regime could be either of two situations, depending on which process is dominant, thermal diffusion or optical absorption.

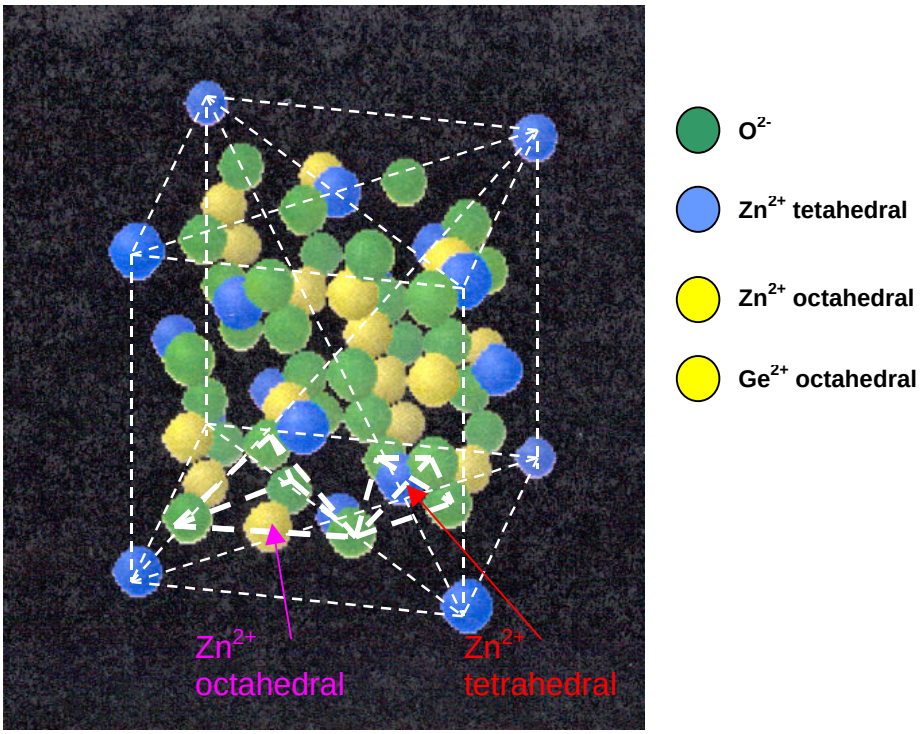

Figure 2-7 Reverse spinel structure of Zn_2GeO_4

This is determined by three factors: 1) the laser pulse parameters (temporal power density $I_{(t)}$, pulsed duration t_p, and wavelength $\boldsymbol{l}$), 2) target optical properties (reflectivity R, and absorption coefficient α), and 3) the thermal properties of the target materials (thermal conductivity K, latent heat per unit volume L_v, specific heat per unit volume C_v, and ablation temperature T_v, etc). Thermal diffusion length L_d is given by the equation:

$$L = \sqrt{2 * D * t_p}$$
$$D = K / C_v$$

When the thermal diffusion length is larger than the optical absorption length, the laser penetrates deeper into the target resulting in ablation of particles from the target. When the thermal diffusion length is smaller than the optical absorption length, only the near-

surface region of the target is heated up by laser. More details about the pulsed laser deposition mechanism is referred to [54].

Formation of particles on the phosphor film surface is an issue. There are several ways to reduce surface particle density. One method is to increase ambient gas pressure to prevent ablated target clusters from forming a particle before they reaches substrate. A second option is to place the substrate at an angle to the target plane, instead of placing it right above the target, to keep the substrate away from the particle landing area.

2.7 ZnMgS:Mn ACTFEL Devices

2.7.1 $Zn_{1-x}Mg_xS$-based Thin Film Growth

ZnMgS:Mn electroluminescent thin film devices were only reported by Noma and Minami, et al. in 1998.[43] In this report, ZnMgS:Mn films were grown on glass/ITO/SiO_2/SiN_x by e-beam deposition. Mn doping was provided from a MnS source. It was grown at a substrate temperature of 150^{o}C and in-situ annealed at 630^{o}C for 1 hour. The best electroluminescence was 333cd/m^2 at a drive frequency 60Hz. The EL emission wavelength of the film deposited from a $Zn_{0.7}Mg_{0.3}S$:Mn source was 552nm, which is a greenish color.[43]

ZnMgS is also used for quantum well devices. It was reported that ZnS/ZnMgS films were grown on III-V compound semiconductor single-crystal substrates to form quantum wells.[55, 56] The deposition techniques used were MOCVD (metal oxide chemical vapor deposition)[55] and MBE (molecule beam epitaxy).[56] A strain effect due to lattice constant mismatch was observed in the ZnS/ZnMgS quantum wells.

The stoichiometry of ZnMgS film is strongly affected by ambient sulfur pressure during processing. ZnMgS grown by MBE under excess sulfur pressure has been reported.[57] Extra sulfur pressure was observed to increase the growth rate. Without the use of excess sulfur, ZnMgS film deposition on GaP was not repeatable.[57]

2.7.2 ZnS-MgS Crystal Structures

ZnMgS is formed from the reaction of ZnS and MgS. The typical ZnS crystal structures are cubic zinc-blende or hexagonal wurtzite. MgS forms in the cubic rocksalt crystal structure. The two ZnS structures are illustrated in Figure 2-8. The zinc-blende structure is similar to the diamond structure, which is two interpenetrating face centered cubic (f.c.c.) primary units located at positions ¼ of the body diagonal from each other in the [111] diagonal direction. The only difference between the zinc-blende structure and diamond structure is that the two f.c.c cells in zinc-blende are occupied by two different types of atoms (ions), such as Zn^{2+} and S^{2-} for the case of ZnS. The wurtzite form of ZnS is two hexagonal primary units with one lattice shifted in $[1\bar{2}\bar{2}0]$ direction, as shown in Figure 2-8, with one lattice occupied by Zn^{2+}, the other by S^{2-}. MgS occurs only in the cubic rock-salt structure, which has two f.c.c. primary units with one lattice shifted ½ in the [100] direction.

2.7.3 ZnS-MgS Solubility

For ZnMgS, the amount of MgS replacing ZnS is restricted by its solubility in ZnS. The equilibrium phase diagram of ZnS and MgS is shown as Figure 2-9. As shown in this diagram, from pure ZnS to ZnMgS with 7% MgS incorporation exhibits the ZnS-β phase

in the wurtzite hexagonal structure, while ZnMgS with 7% to 24% MgS replacement produces the ZnS-α phase, which is zinc-blende cubic structure. In ZnMgS with over 24% MgS replacement, a separate MgS-γ phase will be formed which is rocksalt cubic structure.

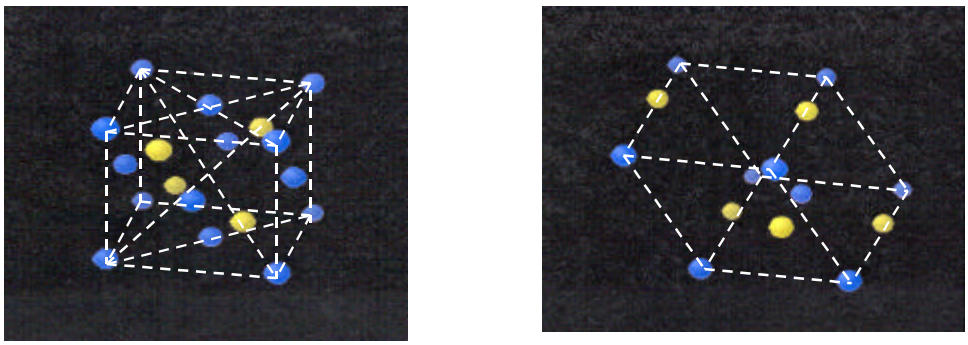

a) b)

Figure 2-8 ZnS crystal structures: a) zinc-blende and b) wurtzite

Therefore, ZnS can be replaced by only 24% MgS before the MgS phase is segregated out. Slightly different solubility for ZnS and MgS was reported in other literature.[58] Zn can replace Mg at atomic percentages up to 0.87 percent, resulting in a compound formula of $Zn_{0.87}Mg_{0.13}S$, compared with pure ZnS. It was reported that Zn-rich $Zn_xMg_{1-x}S$ at $1<x<0.14$ is zinc-blende structure, and Mg-rich $Zn_xMg_{1-x}S$ at $0.07<x<0$ is rocksalt structure.[59]

2.7.4 Crystal Field Modification of Mn^{2+}

The outer shell electron arrangement of a Mn atom is $3d^5 2s^2$. After two electrons are lost from the outer shell, the Mn^{2+} ion is formed with an outer shell electron arrangement of $3d^5$. The quantum level of the five electrons is ^6S, ^4G, ^4D, ^4P, ^4F, respectively, in terms of

quantum level definition: ^{2s+1}L.[16] These five quantum levels are the case for an isolated Mn^{2+}

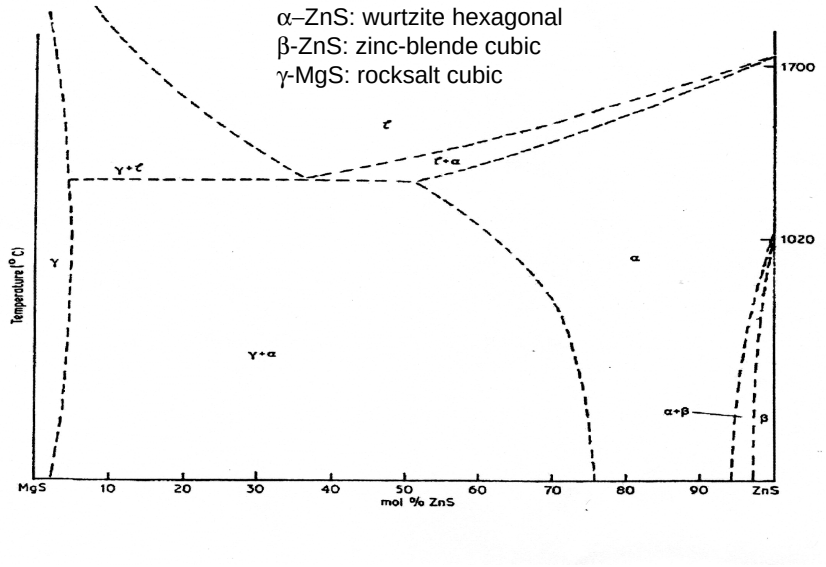

Figure 2-9 Equilibrium phase diagram of ZnS-MgS

The ^6S is the ground state of an isolated Mn^{2+}. These levels are degenerated under the crystal field, but the extent depends on the environment of the Mn^{2+} ion. The five levels are split in the way as shown in Figure 2-10. For instance, ^4G is split into three $^4T_1$, $^4T_2$, and ^6A. The only allowed transition in Mn^{2+} is the transition from $^4T_1$ of ^4G to ^6A of ^6S. The level of $^4T_1$ of the Mn^{2+} ion is changed depending on the strength of the crystal field formed around it. How the crystal field strength effects the energy states is governed by Schrodinger's Equation:

$$(\frac{2E}{\hbar} + \vec{V})\Psi = 0 \qquad (2\text{-}8)$$

in which *h* is Plank's constant, *E* is the kinetic energy, ***V*** is the potential and Ψ is the wave function of an electron. ***V*** is the crystal field strength mentioned above, which is a

vector quantity. According to the crystal field theory, the transition of dopant ions can be simulated.[60] According to the parity rule discussed in Section 2.7.4., the $^4T_1$ to $^6A_1$ transition of Mn^{2+} in a symmetric position is allowed, while $^4T_1$ to $^6A_1$ in a non-symmetric position is not allowed. An octahedral position is formed by eight facets, which are constructed by six atoms, as shown below in Figure 2-11 (a). In contrast, the tetrahedral position is formed by four facets and constructed by four atoms. The tetrahedral position of Mn^{2+} shown in the Figure 2-11 (b).

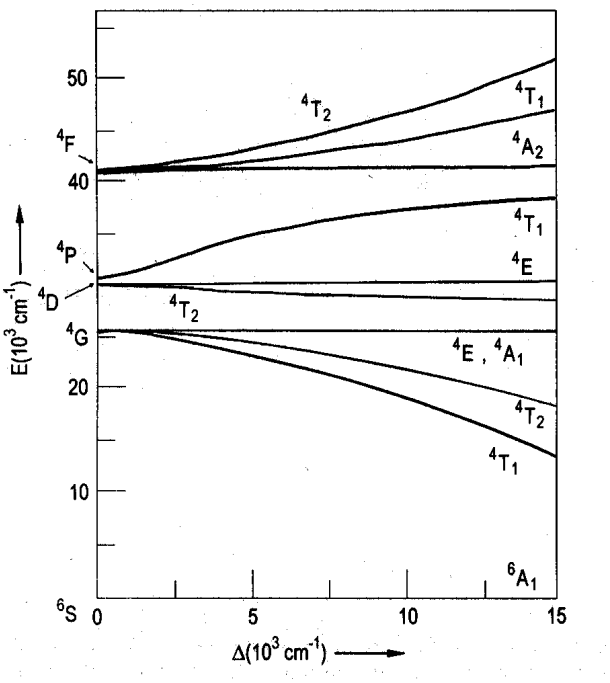

Figure 2-10 Degeneration of Mn^{2+} energy states under crystal Field

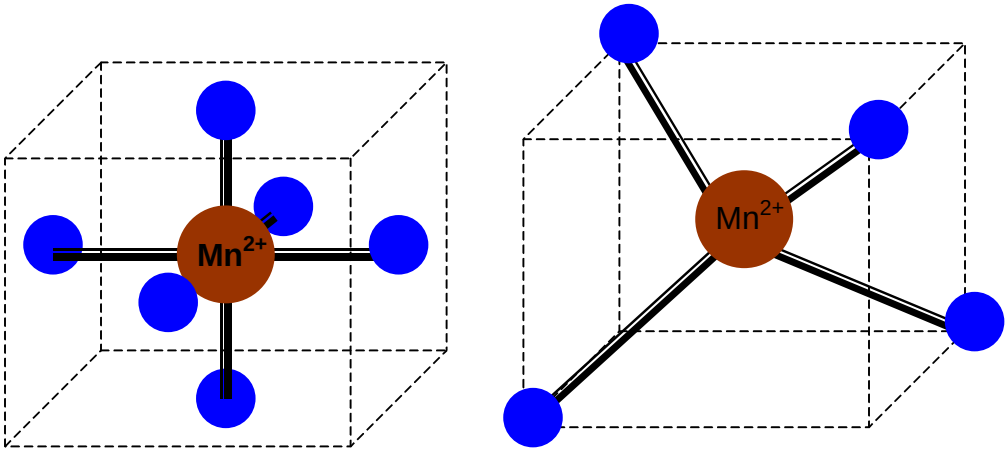

a) b)

Figure 2-11 Positions of Mn^{2+} luminescent center in host a) at octahedral and b) at tetrahedral

CHAPTER 3
EXPERIMENTAL PROCEDURES

Preparation of Zn2GeO4:Mn and ZnMgS:Mn green ACTFEL devices includes source preparation, substrate choice, thin film deposition and heat treatment. Characterization of the devices includes the optical, electrical, microstructural and chemical characterization.

3.1. Source Preparation

Two different phosphor layers were used for green ACTFEL devices in this research: Zn_2GeO_4:Mn and ZnMgS:Mn. Targets (or pellets) of source material were required for the thin film deposition techniques used. These source materials were not commercially available in target form, but required careful preparation before any deposition processes could be utilized. The compound Zn_2GeO_4:Mn target was prepared both for pulsed laser deposition and RF sputtering, while $Zn_{1-x}Mg_xS:Mn_y$ pellets were used for e-beam evaporation. Generally the target can be used for many runs of sputter deposition, while the pellet can be used only once for evaporation and should be completely evaporated during the evaporation process.

3.1.1 Preparation of Zn_2GeO_4:Mn Target

Two Zn_2GeO_4:Mn targets at one-inch diameter and prepared exactly in the same way were used respectively for pulsed laser deposition and sputtering deposition. The Mn concentration ([Mn]) was fixed at 1.5% atomic relative to Zn concentration ([Zn]) in the

target. According to the literature, there is an optimum [Mn] for best optical performance in Zn_2GeO_4:Mn of approximately 1%~2%.[61, 62]

The Zn_2GeO_4:Mn target was obtained by firing a powder mixture of ZnO, GeO_2 and MnO_2 at a temperature of 1100^oC. There were two firing processes involved: firing before and after the target was pressed. The goal of the pre-firing process was to obtain Zn_2GeO_4:Mn resulting from the reaction of the powder mixture. The goal of the post-firing process was to condense the target for better thin film growth. Details of the Zn_2Geo_4:Mn target preparation are shown in the following chart:

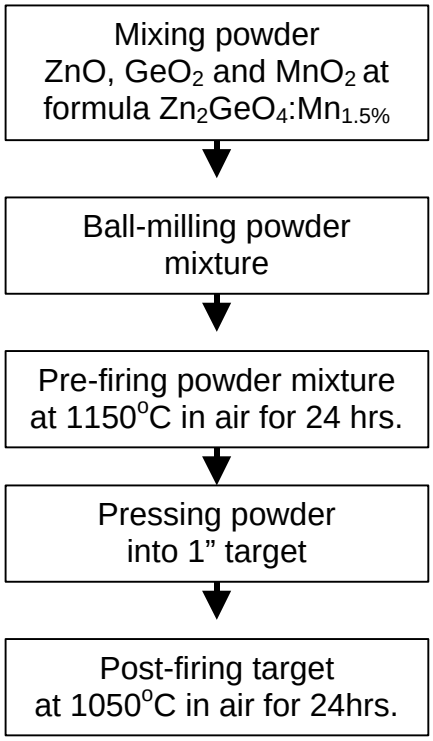

Figure 3-1 Flow chart of Zn_2GeO_4:Mn target preparation procedure

First, ZnO, GeO_2 and MnO_2 powders were mixed at the formula ratio Zn_2GeO_4:Mn 1.5%. All the source powders were purchased from Alfa Aesar. Even though Mn^{2+} is the luminescent center in Zn_2GeO_4:Mn, the source used for Mn was

MnO_2, with an ionic valence of Mn^{4+}. This was done because Mn^{4+} was expected to substitute one of the two Zn^{2+} positions to become Mn^{2+} after the powder mixture was fired. The physical properties of the three powder sources are listed in the table:

Table 3-1 Physical properties of Zn_2GeO_4;Mn target source materials[63]

Zn_2GeO_4:Mn	ZnO	GeO_2	MnO_2
Atomic ratio	2	1	0.15%*2
F.W. (g/mol)	81.37	104.59	86.94
Melting point(^oC)	1975^oC	1086^oC	535^oC (decompose.)
Purity (Puratronic)	99.9995%	99.999%	99.9995%

Next, in order to obtain an intimate physical mixing, the powder mixture was ball-milled with ceramic media for 24 hrs. During ball milling, the powder mixture was immersed in acetone. The color of the pure MnO_2 source was dark gray, and the ZnO and GeO_2 were white. It was evident that the powders were well mixed after ball milling since the powder mixture was changed from white to gray even though it contained only a very small amount of MnO_2. Mixing and grinding by hand would not be capable of changing the mixture color from white to gray. After ball-milling, the mixture was dried on a hot plate to remove the acetone.

Third, the mixture powder was fired in a furnace at 1150^oC in N_2 for 24 hours to form Zn_2GeO_4:Mn. The Zn_2GeO_4 crystal structure was expected to be formed upon firing. Firing is a chemical process since ZnO, GeO_2 and MnO_2 reacted with each other during firing. During firing, Mn^{4+} in MnO_2 was expected to convert into Mn^{2+} and replace the Zn^{2+} in the octahedral position of the spinel structure, but not the Zn^{2+} in the tetrahedral position since the transition of Mn^{2+} is only allowed when it is at the

symmetric octahedral position rather than non-symmetric tetrahedral position. The Mn^{2+} transition is referred to in Section 2.7.4..

Fourth, the fired powder mixture was pressed into an one inch diameter target using an hydraulic press. After placing the powder into a 1" diameter steel die, a 5000lb force was slowly loaded onto it to form the target. Porosity was a concern for the target. A solid and highly condensed target was desired for both pulsed laser deposition and sputtering deposition, especially for the former since it is less likely to be cracked during deposition by high energy laser because of higher thermal conductivity. A good quality film starts with a good target. A large press loading can reduce porosity in the target. However, overloading during pressing would result in the cracked target. The way to measure porosity of a target is by the pore density given by the following equations,

$$\textit{Pore density} = \textit{Actual mass density} / \textit{Theoretical mass density} \quad (3\text{-}1)$$

$$\textit{Real mass density} = \textit{Target weight} / \textit{Target Volume} \quad (3\text{-}2)$$

$$\textit{Theoretical mass density} = \textit{Weight of all atoms in the primary cell} / \textit{Volume of the primary cell} \quad (3\text{-}3)$$

Since the size of Zn_2GeO_4:Mn target was 1" in diameter and 0.5cm high and the weight was 3.74g, the actual mass density of Zn_2GeO_4:Mn was given by

$$\textit{Actual mass density of } Zn_2GeO_4 \textit{:Mn target} = \textit{Weight of the target} / (\boldsymbol{p} * (\textit{diameter of the target}/2)^2 * \textit{height of the target} \quad (3\text{-}4)$$

The volume of a primary unit Zn_2GeO_4 is a*b*c where a,b,c are lattice constants. A Zn_2GeO_4 primary unit contains two Zn_2GeO_4 molecules and each Zn_2GeO_4 molecule contains two Zn atoms, one Ge atom and four O atoms. Therefore, the theoretical mass density of Zn_2GeO_4:Mn is given below,

$$\textit{Theoretical mass density of } Zn_2GeO_4 \textit{:Mn Target} = 2 * (2 * F.W.(Zn) + F.W.(Ge) + 4 * F.W.(O)) / (a*b*c) \quad (3\text{-}5)$$

It should be noted that since Mn concentration is low, its contribution to the theoretical mass density of Zn_2GeO_4:Mn was ignored. The pore density of the Zn_2GeO_4:Mn target was 0.45 according to the above equations, assuming Zn_2GeO_4:Mn is in the rhombohedral crystal structure. It should be noted that there are three different Zn_2GeO_4:Mn forms, which have different lattice constant a, b, and c. Here the rhombohedral Zn_2GeO_4:Mn was chosen for the pore density calculation.

Finally, the target was post-fired in a furnace at 1050^{o}C in N_2 for 24 hours to consolidate the target. The temperature was increased slowly to 150^{o}C in 4 hours and remained at 150^{o}C for 4 hours in order to completely remove moisture from the target before it was heated up quickly to 1050^{o}C in 2 hours. Normally, the outer part of a target heats up faster than the inner part. If the temperature were increased too quickly from room temperature to 1050^{o}C, the outer part of the target would become dense before the moisture in the inner part came out. The moisture would then be trapped inside the target and the target tends to be cracking during firing.

3.1.2 Preparation of $Zn_{1-x}Mg_xS:Mn_y$ Pellets

The $Zn_{1-x}Mg_xS:Mn_y$ pellets were obtained by reacting ZnS, MgS and MnS (or metal Mn) powders which were mixed according to the formula ratio of Zn, Mg, and Mn. As shown in Figure 3-2, the pellet preparation procedure basically can be broken into three steps: 1) grinding the power mixture, 2) sintering in Ar/H_2S at 650~850^{o}C and 3) shaping it into 0.25” diameter pellets which can fit into the 0.5” diameter graphite crucible. The most important part for the pellet preparation was sintering, in which step the ZnMgS crystal structure was expected to form.

3.2 Substrate Preparation

3.2.1 Glass/ITO/ATO Substrates

The substrate types used for this research were glass and Al_2O_3 ceramic. Both types were deposited with a bottom conducting layer and a bottom dielectric layer before they were used for the phosphor layer growth. Therefore, the substrates, along with the two bottom layers, were glass/ITO/ATO and Al_2O_3/Au/Pb(ZrTi)O_3, which are used for standard EL devices and inverted EL devices respectively.

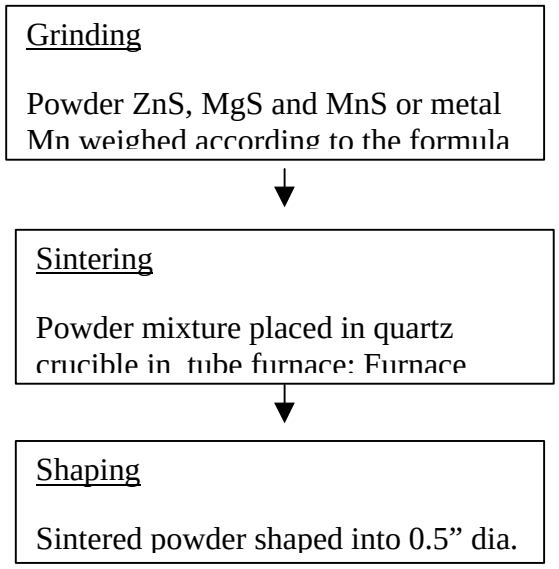

Figure 3-2 Flow chart of $Zn_{1-x}Mg_xS$:Mny pellet preparation procedure

Transparent glass/ITO/ATO substrates were used for the standard ACTFEL devices in which the emitted light comes out of the substrate side. The glass substrate used here can resist temperatures up to 850^{o}C. ITO is a 2000Å transparent conducting layer and ATO is a 2500Å transparent dielectric layer. The ATO layer was formed from Al_2O_3/TiO_2 layers deposited using atomic layer deposition by Planar Systems, Inc. It was used for both

standard ZnMgS:Mn and Zn_2GeO_4:Mn ACTEFL devices. Since the annealing temperature of this substrate was restricted by the glass substrate transition temperature and ITO degradation temperature, the highest annealing temperature used for this substrate was 800^oC for 2 minutes.[46] Before the substrate was loaded into the vacuum chamber, it was cleaned in an ozone cleaner for 6 minutes and blow dried. The substrate was cut from 2"x2" into 0.67"x1" for e-beam evaporation of ZnMgS:Mn, into 0.5" x 0.5" for pulsed laser deposition of Zn_2GeO_4:Mn and into 1"x1" for sputtering deposition of Zn_2GeO_4:Mn depending on the available thickness uniformity for each of the deposition techniques.

3.2.2 Al_2O_3/Au/Pb(ZrTi)O_3 Substrates

The opaque Al_2O_3/Au/Pb(ZrTi)O_3 substrate was used for the inverted ACTFEL devices. In this case, the emitted light comes out of the top transparent layer(s) instead of the substrate side. The Al_2O_3 substrate is a 0.5mm polycrystalline ceramic sheet. A 2000Å gold layer was deposited on the ceramic sheet and patterned as electric contacts. A 20μm Pb(ZrTi)O_3 (PZT) layer was screen printed on the gold layer. The 2"x2" substrates with Au and PZT were provided by Westaim. The Al_2O_3 substrate, including the Au layer and the PZT layer, is referred to as the PZT substrate in this dissertation. Pb(ZrTi)O_3 has a much higher processing temperature and much higher dielectric constant compared with ATO. The processing temperature of Pb(ZrTi)O_3 is limited by its melting temperature of 950^oC [63] and its dielectric constant ranges from 300~1500.[36] This substrate was used for Zn_2GeO_4:Mn ACTFEL devices since high temperature was required for crystallization of Zn_2GeO_4:Mn. The crystallization temperature of

Zn_2GeO_4:Mn is 650^oC.[46] The patterned 2”x2” substrate could be used for four individual EL device units. One 2”x2” substrate was cut into four 0.25” x 0.25” substrates for pulsed laser deposition of Zn_2GeO_4:Mn or four 1”x1” for sputtering deposition of Zn_2GeO_4:Mn. The poor thickness uniformity of pulsed laser deposition restricted the substrate size down to 0.25” x 0.25”. The size of the substrate used for sputtering deposition of Zn_2GeO_4:Mn was restricted by the size of the one inch diameter Zn_2GeO_4:Mn target and the substrate-target distance of 3.1cm.

3.3 Thin Film Growth

Growth of phosphor layers was one of the most important parts of this research. The ZnMgS:Mn phosphor layer was grown by e-beam evaporation and the Zn_2GeO_4:Mn phosphor layer was grown by pulsed laser deposition and RF sputtering deposition. All phosphor layers were grown in vacuum systems at base pressures varying from 10-5 to 10^{-6} Torr.

3.3.1 Vacuum Systems

The deposition techniques for the top opaque Al conducting layer, the top transparent conducting layer and the top transparent dielectric layer are not included here. The vacuum system used for each of the three phosphor layer deposition techniques was different. However, in all these cases the roughing vacuum was provided by an oil-sealed mechanical pump. When the roughing pressure reaches the crossover point of 100 mTorr, the roughing valve is closed, backing valve is opened and the gate valve for high vacuum is opened. The high vacuum pump is typically backed up by the same mechanical pump

used for roughing. Several interlocks are used in the vacuum systems. Interlock between vacuum gauge and high vacuum valve is designed to prevent damaging the high vacuum pump when the chamber pressure is too high. Vacuum gauges varied from low vacuum thermo-couple and capacitance gauges to high vacuum ion gauges. More details about vacuum system design and maintenance is referred to.[64, 65]

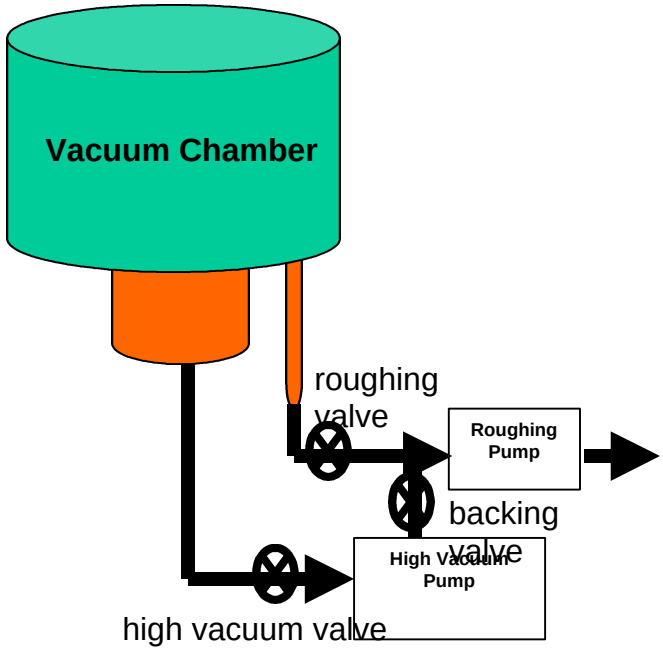

Figure 3-3 Schematic diagram of vacuum systems

3.3.2 Pulsed Laser Deposition of Zn_2GeO_4:Mn

Pulsed laser deposition of Zn_2GeO_4:Mn was prepared by two different systems, one at University of Florida and one at the Naval Research Laboratory (NRL) in Washington D.C. The Zn_2GeO_4:Mn samples prepared by University of Florida focused on photoluminescence of Zn_2GeO_4:Mn on silicon. The samples prepared by NRL were

aimed at obtaining electroluminescence of Zn_2GeO_4:Mn on glass/ITO/ATO and on Al_2O_3/Au/Pb($Zr_{0.5}Ti_{0.5}$)O_3.

The pulsed laser deposition parameters generally include laser power density, laser repetition rate, background ambient gas pressure, deposition time and substrate temperature. The deposition condition for pulsed laser deposition of Zn_2GeO_4:Mn at UF is summarized in Table 3-2.

Table 3-2 Pulsed laser deposition parameters of Zn_2GeO_4:Mn at UF

PLD parameters	
Target material	Zn_2GeO_4:Mn
Target rotation	1 rotation/sec
Distance of substrate-target	10cm
Laser source	KrF 248nm
Laser energy	400 mJ 800 mJ
Laser focal size	0.25cm^2
Laser repetition rate	10 shots/sec.
Base pressure	$5*10^{-5}$ Torr
Ambient gas	O_2
Ambient gas pressure	200m Torr
Substrate material	Si glass/ITO/ATO
Substrate temperature	250^oC and 800^oC
Deposition time	30 min.

The pulsed laser deposition parameters for the samples prepared by NRL is listed in Table 3-3.

The laser deposition parameters shown in the two tables are slightly different. However, the following two formulas can be used for the conversion:

Laser energy density (J/cm^2) = Laser energy (J) / laser focal size (cm^2)

*Total laser shots = laser repetition (shots/sec) * deposition time (s)*

The film quality and thickness was dependent on the extrinsic parameter laser energy density rather than the intrinsic parameter laser energy. The film quality and thickness was dependent on the total laser shots rather than deposition time.

Table 3-3 Pulsed laser deposition parameters of Zn_2GeO_4:Mn at NRL

PLD parameters	
Target material	Zn_2GeO_4:Mn
Laser source	KrF 248nm
Laser energy density	0.8J/cm^2 1.6J/cm^2
Laser shots	10,000 shots
Base pressure	5*10^{-5} Torr
Ambient gas	O_2
Ambient gas pressure	150 mTorr 200 mTorr
Substrate material	Si glass/ITO/ATO, Al_2O_3/Au/PZT
Substrate temperature	R.T. 250^{o}C 800^{o}C

The samples prepared respectively by the two different facilities were not intended to use for comparison because the systems were different, despite the use of similar laser parameters.

3.3.3 RF Sputtering Deposition of Zn_2GeO_4:Mn

A schematic of the RF sputtering deposition of Zn_2GeO_4:Mn used for this research is shown in Figure 3-4. An RF power source was used to sputter the insulating Zn_2GeO_4:Mn target, which was placed 3.1 cm above the substrate. A gas mixture of Ar

and O_2 was supplied to the chamber during sputtering. Oxygen was added to reduce possible O deficiency in the Zn_2GeO_4 film growth.

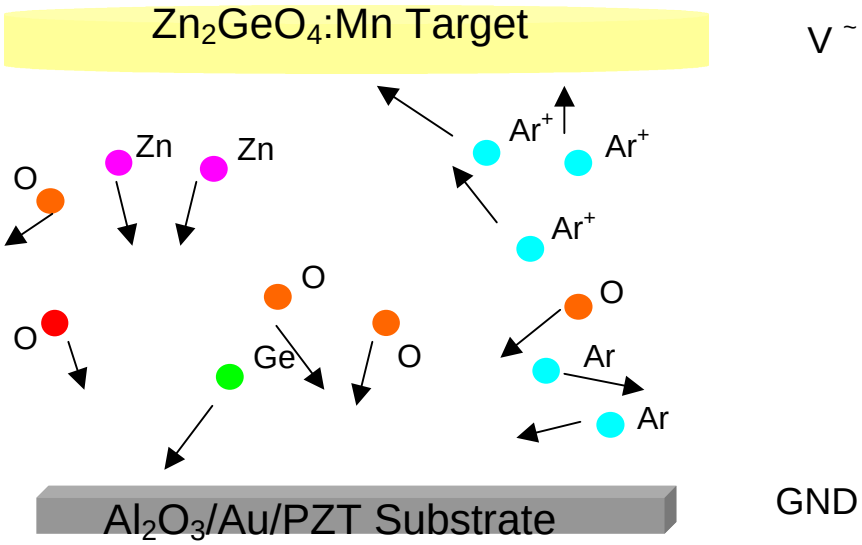

Figure 3-4 Schematic diagram of Zn_2GeO_4:Mn RF sputtering deposition

Argon atoms were ionized by the RF electric field into Ar^+ ions. Electrons from Ar ionization were accelerated and impacted other Ar atoms to form a self-sustaining Ar^+ plasma in the chamber. Ar+ ions bombarded the Zn_2GeO_4:Mn target to knock off atoms of Zn, Ge and O from the target by momentum transfer. Since no heating element was used during the sputtering deposition of Zn_2GeO_4:Mn, all the sputter deposited Zn_2GeO_4:Mn films used for this research were grown at room temperature. The RF sputtering deposition parameters used for Zn_2GeO_4:Mn growth are listed in Table 3-4. The target used for Zn_2GeO_4:Mn sputtering deposition was prepared in the same way as the one used pulsed laser deposition. Further details about the target preparation are referred to in Section 3.1.1.. This sputtering system was originally made at Materials Research Inc. It accommodated three large targets, one 6” and two 8”. One of the 8”

target sites was modified into three 1” target sites. The distance between the 1” Zn_2GeO_4:Mn target and the substrate plane was 3.1cm.

Table 3-4 RF sputtering deposition parameters of Zn_2GeO_4:Mn

Target	Sintered 1” Zn_2GeO_4:Mn
Substrates	Al_2O_3/Au/PZT NEG/ITO/ATO Si
Base pressure	$5*10^{-5}$ Torr
Ambient gas	pure Ar Ar 70 sccm /O_2 30 sccm Ar 50 sccm/O_2 50 sccm
Working pressure	7.2mT 15mT 25 mT
Target power	RF AC 25w (reflected 0w)
Substrate temp.	R.T.

Due to limitations of the size of the target and the target-substrate distance, 1”x1” substrates were used to ensure better film thickness uniformity. The three different substrates used for sputtering deposition of Zn_2GeO_4:Mn were Al_2O_3/Au/PZT, glass/ITO/ATO and Si. The PZT substrates and the glass/ITO/ATO substrates were used for ACTFEL Zn_2GeO_4:Mn devices. The Zn_2GeO_4:Mn films deposited on Si were used for microstructural characterization since the background interference from substrate Si is much less than that from substrate PZT.

3.3.4 Electron Beam Evaporation of ZnMgS:Mn

A schematic of the electron beam evaporation used for ZnMgS:Mn growth is shown in Figure 3-5. Electrons were emitted from a filament and accelerated by a 10KV supply. The current for accelerated electrons ranged from 0 ~10A, and the electrons were directed and focused by a pair of permanent magnets. A ZnMgS:Mn pellet was placed in a carbon crucible. When the energetic electrons bombarded the pellet, decomposition or evaporation or sublimation of the pellet occurred. The ZnMgS:Mn pellet sublimed and decomposed into atomic Zn, Mg, Mn and S. Upon sublimation S atoms could be formed as clusters of S_2 or S_4 before reaching the substrate. The substrate was heated up from room temperature to 200^{o}C. A ZnMgS:Mn film grown at elevated temperatures was expected to have better film crystallization than one grown at room temperature. Deposition rate was controlled by the filament current. Film thickness was monitored by a quartz crystal oscillator, and controlled by a shutter located over the substrate, which was operated manually. The distance between the pellet source and the substrate in the system was 15 cm. The E-beam evaporation parameters for ZnMgS:Mn growth are listed in Table 3-5. The glass/ITO/ATO substrates were used for the ZnMgS:Mn standard EL device structure. A base pressure of $5*10^{-6}$ Torr provided a mean free path of 1 cm for the background gas atoms. The mean free path is inversely proportional to the base pressure, therefore higher vacuum establishes a longer mean free path. Also, a low base pressure provides less contamination from background gas atoms during the ZnMgS:Mn growth. The ultimate base pressure of the high vacuum diffusion pump used was $1* 10^{-7}$ after 6 hours of pumping. Elevated substrate temperatures resulted in two things: a better ZnMgS:Mn crystalline growth and variation in the Mn doping in the film. The ZnS (or

ZnMgS) sticking coefficient is a strong function of substrate temperature. When the substrate temperature is over 250^{o}C, there is no ZnS growth on the substrate since the desorption rate is greater than the deposition rate.[66] The reduction of ZnS growth rate with substrate temperature indirectly changed the Mn concentration relative to the host ZnS (or ZnMgS).

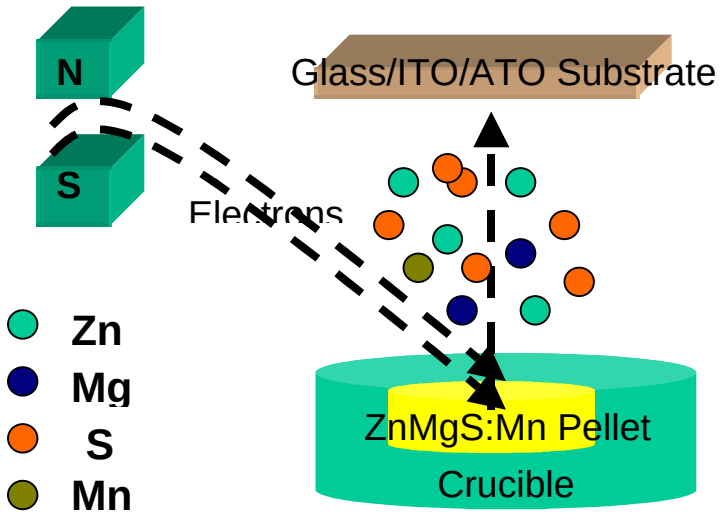

Figure 3-5 Schematic diagram of $Zn_{1-x}Mg_xS$:Mn E-beam evaporation

There is an optimal luminescent center concentration in the host. As explained in Section 2.5.4.2., either too low and too high luminescent center concentration will reduce the brightness. Therefore, an optimal deposition rate is preferred. If it is too high, it is obvious that the growth quality of ZnMgS:Mn is poor, since more defects and dislocations tend to be formed at high deposition rate. If the rate is too low, the incorporation of the background gas atoms into the ZnMgS:Mn films is more likely to occur. Generally, films of the same thickness are used for comparison since the brightness is a strong function of the thickness. One micron was typically used for the

standard thickness. However, the e-beam evaporation rate of ZnMgS:Mn was difficult to control since it was dependent on several parameters, including Mg replacing percentage, the electron filament current, the substrate temperature, etc. The e-beam evaporation of ZnMgS:Mn in this research was more focused on the quality of the film rather than the thickness of the film.

Table 3-5 E-beam evaporation parameters of $Zn_{21-x}Mg_xS$:Mn

Evaporation Parameters	
Substrate	glass /ITO/ATO
Base pressure	$5\sim8x10^{-6}$ Torr
Substrate temperature	R.T. ~200^oC
Deposition rate	1~20nm/s
Thickness	0.3~1.5um

3.3.5 Deposition of Conducting Layers

After the phosphor layer was finished, a top conducting layer was required to form an EL device. The majority of the EL devices used for this research were half cell structures, which do not require a top dielectric layer. In this case, the top conducting layer was deposited directly on the phosphor layer. For the standard EL devices in which the phosphor layer was deposited on transparent glass/ITO/ATO substrates, an opaque metal conducting layer was required to reflect back the emitted light. In this research, a 2000Å Al film was thermally evaporated onto the phosphor layer. The base pressure for Al coating was $5*10^{-4}$ Torr and the deposition rate was approximately 1Å/s, monitored by a quartz oscillator. The Al dots used for optical testing of the EL device were formed using a mechanical mask. For the inverted EL devices in which the phosphor layer was deposited on opaque Al_2O_3/Au/PZT substrates, a transparent conducting layer was

required on top of the phosphor layer. In this case, a 2000Å ITO film was grown by RF sputtering. It was deposited at a working pressure of 3.1 mTorr (base pressure $1*10^{-6}$ Torr), with an ambient of Ar 100sccm/ O_2 3 sccm and RF power 700 W (reflected power 0 W). The target was 8" in diameter so that a large quantity of samples could be deposited with ITO in the same run. The substrate temperature was room temperature. As measured by multimeter with two probes separated at a distance of 5 mm, the sheet resistance of 2000Å ITO ranged from $1\sim10^{6}$ Ω, depending on the degree of addition of O_2. The general rule is that as more O_2 is added, the ITO is less conductive and more transparent, since the mechanism of the ITO electrical conductivity is involved with O vacancies in ITO.[67, 68]

Since Zn_2GeO_4:Mn was deposited on opaque Al_2O_3/Au/PZT substrate. In order to form an ACTFEL device, the top conducting layer should be transparent. In this research, ITO transparent conducting layer was used. ITO sputtering deposition was done in sputtering system. The ITO target was 8" in diameter. To make ITO electrically conductive and optically transparent is of contradiction according to its solid state nature. More details about the electrical conductivity of ITO is referred to Section 2.5.2.1. In our RF sputtering system, the lowest O_2 flow rate can be reaches is 1.5% of full 200 s.c.c.m which is still too high for ITO deposition. Another way to further reduce O_2 in chamber is to reduce working pressure. After adjusted the open position of the throttle valve, the lowest working pressure which can be reached was 7.5 mT. Deposited at the working pressure, the ITO sheet resistance was still up to MΩ. In order to further reduce chamber pressure, the throttle valve was left completely open. The lowest pressure dropped to 3.1 mT. The sheet resistance was also reduced enormously. The resistance comparison at the

two different working pressures is listed in Table 3-6. The resistance was measured by multi-meter with two terminals at a distance of 1 cm. The ITO thickness is 2000 Å. The thickness 2000 Å was obtained at deposition conditions: base pressure $1*10^{-5}$ Torr, Ar 100 s.c.c.m. /O_2 3 s.c.c.m, working pressure 3.1 Torr, power 700 W for 10 minutes. The high deposition rate of 200 Å/min was reached by applying this large power. The reflected power for the 700 W supply was zero. Since oxygen pressure in the chamber should be minimized in order to obtain high ITO conductivity, the base pressure is preferred as low as possible accordingly to reduce oxygen partial pressure in the background.

Table 3-6 ITO sheet resistance at two different working pressures

Working Pressure (Ar 100sccm. / O_2 2%,*200sccm)	ITO sheet resistance (t = 2000Å and s=1cm)
8.1mT	10^5~$10^7\Omega$
3.1mT	10~10^2hΩ

3.4 Thin Film Heat Treatment

Heat treatment is required for re-crystallization of phosphor thin films in most cases. Phosphor thin films are normally grown at low temperatures, especially sulfide phosphor thin films since the substrate temperature is restricted by the high sulfur vapor pressure. Re-crystallization can be achieved upon annealing at high temperature.

Luminous efficiency and luminance is strongly dependent on phosphor film crystallinity [16, 1, 12] since these defects and grain boundaries are responsible for irradiative emission.

3.4.1 Lamp-based Rapid Thermal Annealing

In this research, phosphor thin films deposited on glass/ITO/ATO were annealed by a lamp-based furnace in Ar. High ramping rate is a big advantage of lamp-based furnaces. In this system, ramp up time was 1.5 min from R.T. to 700^{o}C and 2.5 min. from R.T. to 800^{o}C. We called this system rapid thermal annealing (RTA), even though the annealing time was much longer than that defined by the semiconductor industry. Annealing times from 1 min. to 30 min. were typically applied, using programmed recipes. The cooling rate was slow, normally taking 30 minutes to reduce temperature from 700~800^{o}C to 100^{o}C by water and N_2 cooling the lamps.

3.4.2 Box Furnace Annealing

Zn_2GeO_4:Mn films deposited on PZT substrate can be annealed at 800^{o}C for much longer times in air. A box furnace was used to anneal all Zn_2GeO_4:Mn films on PZT substrates. The ramping rate for the box furnace was low, taking 1.5 hrs to reach 700^{o}C and about 2 hrs to reach 800^{o}C.

3.4.3 In-situ Vacuum Annealing

Some of the ZnMgS:Mn films deposited on glass/ITO/ATO were in-situ annealed in vacuum after the evaporation was finished. A tungsten wire heater was placed under

the substrate. Maximum temperatures up to 500^{o}C could be reached for this in-situ annealing.

3.5 Characterizations

In this research, the information about the photoluminescence (PL), electroluminescence (EL) and its charge transfer is given in “Optical and Electrical Characterization”. The information about thin film structure and composition is given in “Microstructural and Chemical characterization”, which includes the following analytical techniques: XRD, SEM/EDX, XPS, SIMS and TEM.

3.5.1 Optical and Electrical Characterizations

3.5.1.1 Chromaticity

Chromaticity as defined in Section 2.3.2., is determined by the CIE coordinate nos x and y. In this research, the CIE coordinated x and y for both photoluminescence and electroluminescence were measured by a spectrometer. At the same time, the brightness and emission spectrum were measured. The model of the spectrometer was PR-550 Spectra Colorimeter. Before the optical data was collected, both the image of the interested sample area and the image of the dark dot in the camera were ensured clear by adjusting focal length of the lenses.

3.5.1.2 Photoluminescence

When a phosphor material is struck by a light source at a certain wavelength, an electron of a luminescent center in the phosphor material is excited to a higher energy state before it relaxes back to the ground state, emitting a photon. This process is called photoluminescence (PL) because the excitation source here is light. PL can be used to characterize both the transitions leading to excitation as well as emission.

3.5.1.2.1 PL/PLE Spectra Excited by Xe Lamp

PL is photoluminescence emission and PLE is photoluminescence excitation. The PL emission spectrum is defined as the emission intensity as a function of wavelength emitted for a constant excitation wavelength. The excitation spectrum is the emitted intensity at a fixed wavelength versus the excitation wavelength. For instance, in order to obtain an emission spectrum of Zn_2GeO_4:Mn, the excitation source was typically set at the wavelength 325 nm, which is close to the bandgap wavelength of Zn_2GeO_4 (4.68 eV).[46] The relationship between wavelength and photon energy is:

$$\boldsymbol{l}\,(nm) = \frac{1240}{E(eV)} \qquad (3\text{-}6)$$

The emitted intensity versus wavelength was measured from 300 nm to 800 nm, which covers the main peak of Zn2GeO4:Mn at around 540 nm. The maximum intensity was at 540 nm. To measure the excitation spectrum, the intensity of emission at 540 nm was measured as the excitation wavelength was scanned from 300 nm to 540 nm. The maximum intensity of the 540 nm emission was identified at an excitation wavelength of 340 nm. The emission spectrum was maximized by 340 nm excitation, which was used

for this study. Photoluminescence emission spectra and photoluminescence excitation spectra were collected using a Photon Technology International integrated PL system that used a 150 W Xe lamp source for excitation and double ¼ cm monochromators for both excitation and detection. This system was especially used for PL emission and excitation spectra of the Zn_2GeO_4:Mn target. The PL intensity from thin film samples was too low to be detected by this system, as the background noise intensity was higher than the sample peak intensity.

3.5.1.2.2 PL Spectra Excited by UV Lamp

A UV lamp was used to measure PL spectra of Zn_2GeO_4:Mn thin films. ZnS:Mn films do not demonstrate any PL at room temperature.[12] An ultra-violet lamp with broad wavelength range from 254 nm to 600 nm was used as the excitation source. The UV lamp incidence plane was placed at an angle of 45^o to the sample plane normal as shown in Figure 3-6.

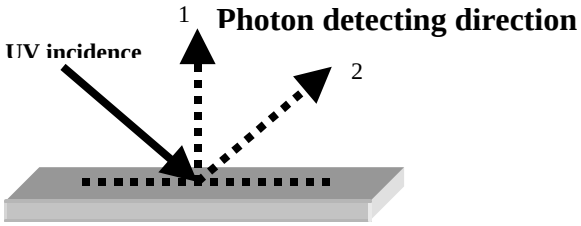

Position 1: Normal to sample plane
Position 2: 45^o to sample plane

Figure 3-6 Schematic diagram of photoluminescence spectrum measurement under excitation of ultraviolet lamp

UV lamp light is not collimated, but comes out in an angular distribution. The illustrated UV incidence direction is simply the UV lamp plane normal. Emitted photons from the sample are detected at an angle either normal to the sample plane or at an angle 45^o to the sample plane. Emitted light was detected by a Photoresearch 650 spectrometer and the detected sample area had a spot size of $0.675cm^2$. The UV source light reflected by the sample was collected together with the light emitted from the sample at the detecting angle 45^o. By placing the detector normal to the sample plane, the UV source reflection could be minimized. The PL spectrum peak shape was broader for the case of the detecting angle at 45^o than that of the angle normal to the sample plane.

3.5.1.2.3 PL Spectra Excited by Laser Source

A laser excitation source of 325nm wavelength (provided by Professor Hummel's group) was used to measure ZnMgS:Mn photoluminescence spectra. No detectable PL could be obtained from ZnMgS:Mn when excited by the above UV lamp. ZnS:Mn thin films do not give any photoluminescence at room temperature.[12] However, after Mg replaced Zn in ZnS:Mn, photoluminescence could be detected in ZnMgS:Mn when using high energy density laser excitation.

3.5.1.3 Electroluminescence (Luminance vs. Voltage)

Electroluminescent brightness is typically determined using a luminance vs. voltage curve (L-V curve). A typical L-V curve has been shown in Section 2.3.1.. Two important parameters obtained from the L-V curve are the threshold voltage (V_{th}) and the brightness 40V above the threshold (B_{40}). In most cases, the terms luminance and

brightness mean the same thing. In the literature, either L or B were used for the brightness. The method for determining V_{th} and B_{40} from L-V curves has been given in Section 2.3.1.. The L-V behavior for an ideal ACTFEL device shows zero brightness below the threshold voltage, since no light is emitted, and above the threshold voltage, the brightness increase dramatically with applied voltage. A real ACTFEL device has a "leaky" voltage process, which means below the threshold voltage the brightness increases slowly and at or above the threshold voltage the brightness increases rapidly.

The voltage driver used for EL measurement was provided by Planar Systems, Inc. and electroluminescence information including emission spectra, chromaticity and luminance was collected by a Photoresearch PR-650 spectrometer. The light emitting sample area was focused and the detected area was a 0.675cm^2 dot. The AC voltage driver was powered by a DC power supply at 300V and 0.025A. The voltage waveform was trapezoidal with a rise time of 5μs, stay time of 30μs, and a drop time of 5μs. The stay time could also be set for 10μs or 100μs. Generally, when longer stay time is used, higher brightness is obtained from the device. The frequencies available for the driver were 60Hz, 1kHz and 2.5kHz. Generally, higher frequencies produce higher brightness. All the Zn_2GeO_4:Mn ACTFEL devices were tested at 2.5kHz and all the ZnMgS:Mn ACTFEL devices were tested at 60Hz. Voltage waveforms seen in the literature also include sinusoidal and triangular.[69]

3.5.1.4 Q-V and C-V Curves

When measuring the L-V curve, information about charge transfer and the capacitance change can be obtained by collecting the device current. When a voltage *V(t)*

is applied to a TFEL device, the charge *Q(t)* accumulates in both sides of an EL device, one side negative with electrons, the other side positive with holes. Dynamic capacitance C(t) is defined as differentiation of charge by voltage, dQ(t)/dV(t). Dynamic capacitance is different from static capacitance, which is defined as charge over voltage. If the charge is linearly changed with the voltage, the dynamic capacitance becomes the same as the static capacitance. The test configuration for Q-V data and C-V data measurement is shown schematically in Figure 3-7. An AC voltage at a certain frequency is applied at terminal V_1 and V_4 as shown in Figure 3-7.

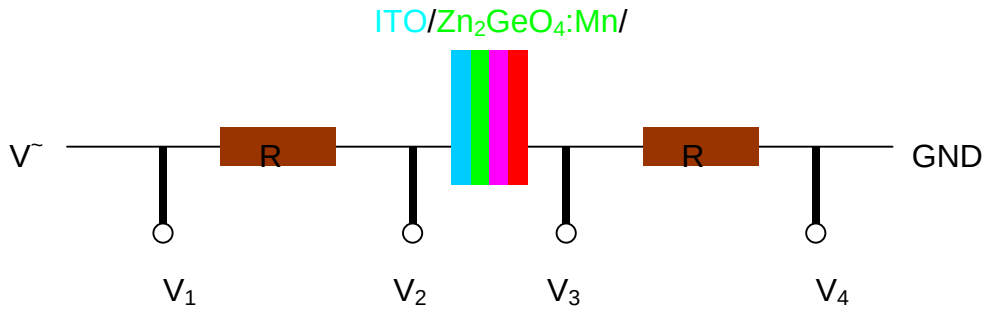

Figure 3-7 Schematic diagram of Q-V measurement for ACTFEL device

Voltage dropped on the TFEL device is given by the difference of terminal V_2 and V_3. Since the two resistors are connected to the EL device in series, current through each of the resistors should be the same as that through the TFEL device due to the charge conservation rule. The current flow through either one of the resistors, *I(t)*, is its voltage drop over its resistance, *V(t)/R*.. The resistors were 100Ω each. The voltage drop across the resistor, for instance, the one on the left side is therefore the voltage difference between terminal V_1 and V_2. The current flow through the resistor is $(V_1-V_2)/R$. The voltage and the current across the phosphor layer are given by the following equations:

(3-7)

$$V_{EL-device}(t) = V_3(t) - V_2(t)$$

$$I_{EL-device}(t) = \frac{V_2(t) - V_1(t)}{R}$$

The V(t) and I(t) is changed with time periodically. They are shown in Figure 3-8. Voltage waveform used for the Q-V curve was the same trapezoidal waveform described in the L-V curve, using 5μs rise time, 30μs stay time and 5μs drop time at each of positive and negative polarization cycle. The current, I(t), reaches its maximum when the voltage rises and drops since $I(t) \propto dV(t)/dt$.

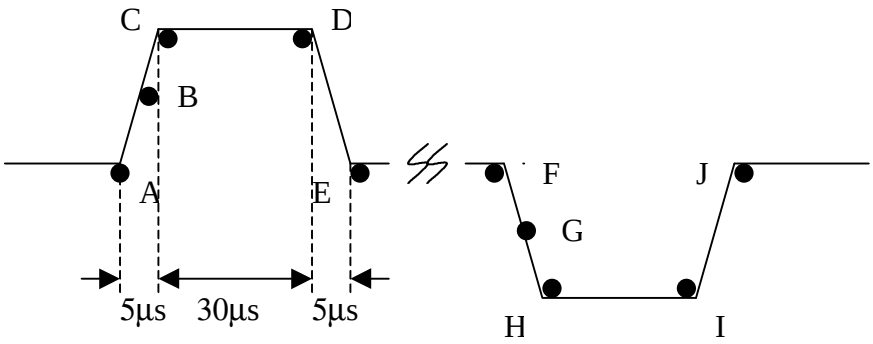

Figure 3-8 Trapezoidal voltage waveform shape of ACTFEL device

A frequency of 2.5KHz was used for the Q-V curve of all Zn_2GeO_4:Mn TFEL devices. The voltage at each of the four terminals was monitored using a Tektronix TDS 510A digitizing oscilloscope. The charge Q(t) is an integration of the current I(t) over time t and it is given by the following equation,

$$Q_{EL-device}(t) = \int I_{EL-device}(t) * dt \qquad (3\text{-}9)$$

Assuming all the charge is relaxed at the end of one polarization, before the next cycle starts, *Q(t)* is an integration of I(t) covering one polarization period. Dynamic capacitance *C(t)* is therefore given by the following equation,[70]

$$C_{EL-device}(t) = \frac{dQ_{EL-device}}{dV_{EL-device}} \qquad (3\text{-}10)$$

Since V(t), Q(t) and C(t) are determined, Q-V and C-V curves are obtained. A typical Q-V curve and C-V curve for Zn_2GeO_4:Mn device are shown in Figure 3-9. The Q-V behavior of the simple equivalent circuit was discussed in Section 2.3.3.. "Equivalent circuit" is shown in Figure 3-7 as the broken lines. The conduction charge and polarization charge discussed for an ideal device are also seen in the Figure 3-7 (broken lines). Two new features seen are the relaxation charge and leakage charge.

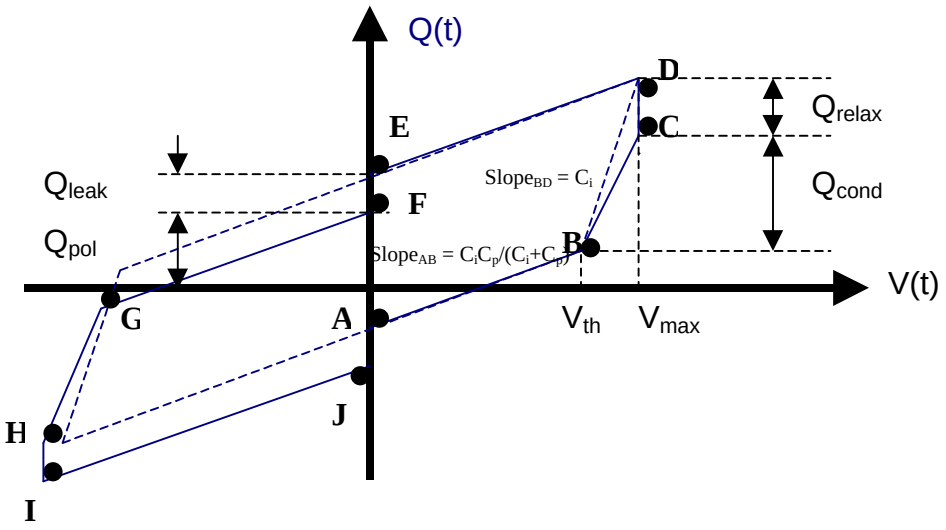

Figure 3-9 Ideal (broken line) and real (solid line) Q-V Curve of Zn_2GeO_4:Mn ACTFEL device

Relaxation charge occurs when the applied voltage reaches its maximum value (or near maximum value in the real case) and reflects current which flows during the dwell, or C-

D portion of the waveform. The name refers to the fact that at a constant applied voltage, conduction charge creates an opposing electric field that relaxes the field across the phosphor layer. The leakage charge occurs once the applied voltage reaches zero and refers to current that flows in the opposite direction as the previous pulse due to the polarization field present at the end of the pulse. For one pulse cycle (positive and negative), before the threshold voltage is reached, the capacitance of the device is the capacitance of the dielectric layer and the phosphor layer in series, which is CpCi/(Cp+Ci). After the threshold is reached, the phosphor layer is broken down and there is no capacitance contribution from the phosphor layer. At this point, the capacitance of the device is the capacitance of the dielectric layer, Ci, which is higher than the value measured before the phosphor layer is broken down. The capacitance is the slope of the Q-V curve. Wager, et al., did an extensive study on electrical characterization of ACTFEL devices using Q-V and C-V. More details about electric characterization is referred to. [70, 71, 72, 73, 74]

3.5.2 Microstructural and Chemical Characterizations

The microstructural and chemical characterizations will be discussed. Their fundamental mechanism and the experimental procedures will be are focused. More details about the microstructural and chemical characterizations can be referred to the books “Materials Characterization Encyclopedia[75] and the TEM technique can be referred to [76].

3.5.2.1 X-ray Diffraction

XRD is acronym of x-ray diffraction. X-ray diffraction is the result of the interference of the incidence x-ray and the reflected x-ray. When the phase of the two x-rays is synchronized, the intensity is added up, and when the phase of the two is 180^o shifted, the intensity is subtracted. A single crystal contains many crystal planes at a certain orientation that can be expressed by Miller indices, such as plane (001) and (111). When incident x-rays strike a single crystal, they are reflected from different crystal planes. Whether the reflected light from the crystal plane is added up or subtracted from the incident light depends on the light travelling distance between the same stacking planes. The added up intensity appears as a peak in the X-ray diffraction pattern. The diffraction occurs according to Bragg's Law, shown below,

$$2d * \sin \boldsymbol{q} = n \boldsymbol{l} \qquad (3\text{-}11)$$

$$d_{hkl} = \frac{a_o}{\sqrt{h^2 + k^2 + l^2}} \qquad (3\text{-}12)$$

where λ is wavelength of the incident x-ray, θ is the angle between the crystal plane normal and both incident and diffraction rays, h, k and l are the Miller indices of the crystal plane and a_o is lattice constant. In the above equation, the cubic crystal structure is assumed otherwise a, b, and c should be used instead of a_o. Information that can be obtained from x-ray diffraction includes crystallite size, crystallinity, strain and lattice constant. If the sample is polycrystalline and the crystallites in the sample are randomly oriented, the numerous diffraction peaks are characteristic of the crystal structure. The FWHM method is used to compare the crystallinity of crystalline samples. FWHM means

the full width at half maximum intensity, Δ(2θ). The Δ(2θ) for both a sharp and broad peak are shown in Figure 3-10. Better crystallinity is associated with a smaller Δ(2θ). The crystallite size *L* is generally inversely proportional to ***D(2q)*** and the relationship of the two is given by, (3-13)

$$L = \frac{\boldsymbol{l}}{\Delta(2\boldsymbol{q})*\cos\boldsymbol{q}}$$

where λ is the wavelength and θ is the angle between the incident x-ray and the crystal plane normal. The X-ray diffraction system used for this research was a Philips APD 3720. The x-ray source was Cu-Kα, which was generated from a Cu tube operated at 40kV and 20mA, with a wavelength of 1.54Å. The scanning angle 2 θ used for the research was from 10^o to 80^o, with a scanning step of 0.05^o. More details about x-ray diffraction are referred to [75].

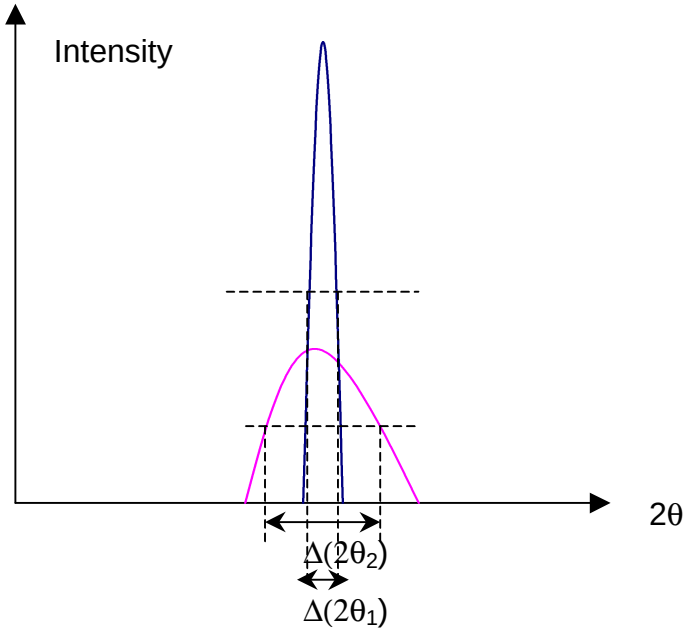

Figure 3-10 Schematic diagram of crystallity comparison using FWHM of x-ray diffraction patterns

3.5.2.2 Scanning Electron Microscopy/Energy Dispersive X-ray Spectroscopy

SEM is an acronym for Scanning Electron Microscopy and EDX is an acronym of Energy Dispersive X-ray Spectroscopy. SEM was used to obtain the film surface image at magnifications up to 20,000x. EDX was used for quantitative analysis of elemental composition in films. EDX is generally more sensitive to heavy chemical elements since the characteristic x-ray yield is increased with the atomic number. Theoretically, chemical elements with atomic number lower than 3 are undetectable by EDX. Practically, the chemical elements with atomic number lower than 5 are almost undetectable by EDX. The SEM functions using electrons emitted from a heated filament. These electrons are then accelerated by a voltage of 15KV before the electron beam size is reduced by a magnetic condenser lens. Magnetic lenses are used to reduce the spot size further to provide the appropriate magnification for secondary electron image. Secondary electron image provides information about sample surface morphology. The secondary electron collector is placed at a low angle close to the sample. A collector for the back-scattered electrons, which are strongly dependent on atomic number, is generally placed at a high angle almost normal to the sample plane. An EDX detector is also placed close to the sample to collect the characteristic x-rays. More details about SEM/EDX is referred to [75]. The mechanism of generation of characteristic x-ray by incident electrons is shown in Figure 3-11. Accelerated electrons from the scanning beam strike atoms in the sample. Generally, electrons in the K shell tend to be excited by these primary electrons into higher shells, such as the L shell. When a primary electron strikes an electron at K shell, an electron at K shell is excited to L shell in the same time.

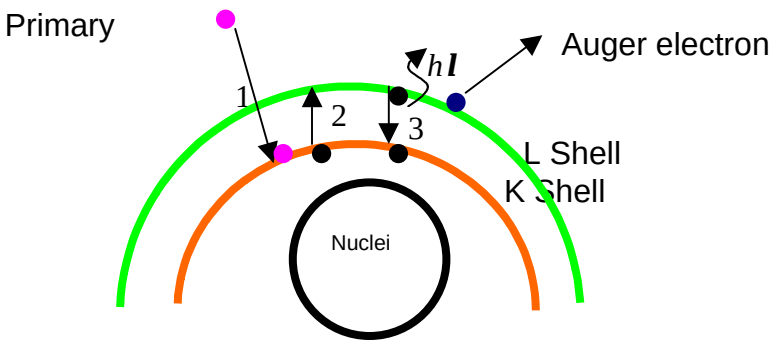

Figure 3-11 Schematic diagram of energy dispersive x-ray spectrum

When the excited electron in the L shell relaxes back to the K shell, either a photon or an Auger electron will be created. The photon, which has an energy equal to the difference between the K shell and L shell, is called a characteristic x-ray, given by the following equation:

$$h\boldsymbol{l} = E_{(L-shell)} - E_{(K-shell)} \qquad (3\text{-}14)$$

Each of the elements has its own set of characteristic x-rays that are used to identify chemical elements in a given sample. When a multilayered thin film sample is being quantitatively analyzed, penetration depth of the primary electrons becomes an issue. The penetration depth is determined by the primary electrons' energy, E, and is given by the following equation:

$$R(\boldsymbol{m}m) = \frac{4120}{\boldsymbol{r}(g/cm^3)} E(KeV)^{(1.265-0.0954*\ln E(KeV))} \qquad (3\text{-}15)$$

Assuming the density is 5g/cm^3 and the applied voltage is 15KV, the penetration depth is 1.23μm. The interaction volume of electrons in the sample is roughly pear shaped[75] and would not give accurate quantitative information of the top layer if the primary electrons penetrate into the layer adjacent to the top layer.

Insulating samples were coated with a thin layer of carbon or Au to make them conductive prior to SEM/EDX. Carbon coating is more often used for EDX analysis because it's characteristic x-ray peaks are less likely to interfere with those from the elements of interest. Au coating is better for SEM imaging. The SEM/EDX system used for this work was the JEOL 6400 and the SEM image and EDX quantitative analysis was processed by the software LinkISIS. SEM image resolution was improved by using a higher condenser lens current and a smaller aperture size. The condenser lens current at scale 11~12 was typically used for a fixed working distance of 15mm. The second smallest aperture was used of the four aperture sizes available for SEM imaging. For EDX analysis, a smaller condenser lens current was used to allow more x-rays to be detected. The typical condenser lens current setting used for EDX analysis was at scale 6~7.

3.5.2.3 X-ray Photo-electron Spectroscopy

XPS is an acronym for x-ray photo-electron spectroscopy. Details about XPS are referred to [75]. In summary, when the Mg source x-ray strikes a given sample, they may knock off inner shell electrons such as those in the K shell. Information about the given chemical element is provided by the energy of the secondary electron, according to the following equation:

$$E = h\boldsymbol{l} - E_{bonding} \qquad (3\text{-}16)$$

Inner shell electrons could also be excited to a higher shell such as the L shell and relax back from the L shell to the K shell to knock out another L shell electron, which is an Auger electron. Its energy is given by the following equation:

(3-17)

$$E_{Auger} = E_{(K-shell)} - E_{(L-shell)} - E_{L-shell}$$

The generation of the photoelectron and Auger electron is shown in Figure 3-12. XPS was used to analyze the chemical bond energy of Ge4+ in Zn2GeO4:Mn films. If the Zn2GeO4:Mn film contains ZnGeO3 or GeO2, the Ge4+ peaks in XPS spectrum should be different since the environment of Ge4+ in each of the three crystal structures (Zn2GeO4, ZnGeO3 and GeO2) is different.

3.5.2.4 Secondary Ion Mass Spectroscopy

SIMS is an acronym for secondary ion mass spectroscopy. Primary ions such as O^- or Cs^+ bombard the specimen to knock off atoms and ions from the specimen from the surface. The sputtered secondary ions are then separated out according to their mass over charge ratio (m/q) using a magnetic field.

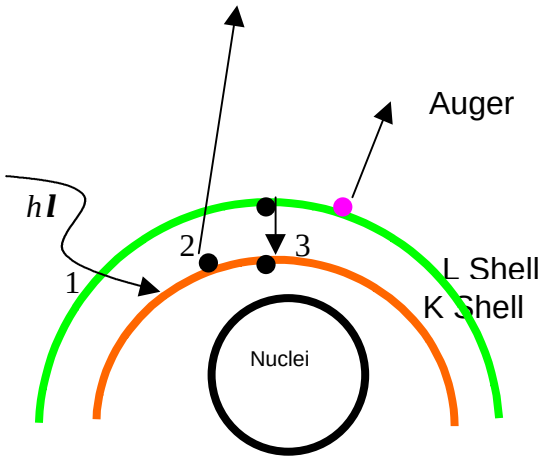

Figure 3-12 Schematic diagram of x-ray photo-electron spectrum

SIMS is especially used for doping profile analysis. The secondary ion yield of a dopant is dependent on yield sensitivity of doping in a given matrix material and it is given by the following equation:

$$\frac{I_{matrix}}{C_{matrix}} = RSF_{dopant-to-matrix} * \frac{I_{dopant}}{C_{dopant}} \qquad (3\text{-}18)$$

$$C_{dopant} = (RSF * C_{matrix}) * \frac{I_{dopant}}{I_{matrix}} \qquad (3\text{-}19)$$

where Cdopant is the dopant concentration, Cmatrix is the matrix element concentration (which can be normalized as 1), RSF is the relative sensitivity factor of the dopant relative to the matrix element, and Idopant is the dopant secondary ion yield and Imatrix is the matrix element secondary ion yield. In this case, a standard is required for absolute doping concentration analysis. SIMS was used to obtain ZnMgS:Mn film profile and to identify Mn2+ absolute doping concentration in ZnMgS.

3.5.2.5 Transmission Electron Microscopy

TEM is an acronym for transmission electron microscopy. This technique was used to analyze the microstructure of ZnMgS:Mn films in this research. A specimen for TEM should be at least 200Å thin so that electrons can effectively pass through. Specimens are normally ion milled to form a wedge where a sufficiently thin region can be used. Before the specimen is ion milled, the sample must first be cut into a square in the size of 0.3mm and glued face to face (in the case of a cross-section sample) with the film part in the middle, hand polished down to 1mm, and dimpled thinner to 20μm. The gluing step is critical. If the initial gluing fails in the later steps, the two pieces are

separated and the sample preparation must start all over again. The glue used for ZnMgS:Mn was G-bond epoxy. The glued sample was heated up to 150^{o}C and remained at that temperature for 30 minutes to ensure a good curing. Since ZnMgS:Mn was deposited on glass substrates, the ion milling time for thinning the glass specimens was much longer than that for silicon specimens. It took 10 hours to finish a 20μm ZnMgS:Mn specimen.

In the TEM, electrons are accelerated under a high voltage up to 400KV, which corresponds to a wavelength of 0.0016nm. Wavelength becomes shorter as higher voltage is applied. The TEM resolution r is restricted by the wavelength λ in accordance with the relationship below,

$$r \propto \boldsymbol{l}^{3/4} \qquad (3\text{-}20)$$

The wavelength can be deduced from the applied voltage, after the theory of relativity is considered for determining the effective electron mass. In this research, the microstructure of ZnMgS:Mn ACTFEL devices and the MgS segregation was identified using TEM cross section. The TEM system used was a JOEL 200CX, operated at 200KV. Two modes were used in the analysis: image mode and diffraction mode. The image mode included bright field mode and dark field mode. The bright field mode generally gives a lower resolution than the dark field mode since the chromatic and spherical aberration are minimized for the dark field mode. The diffraction mode included selected area mode (SAD) and microdiffraction mode. The beam used for diffraction should be parallel. However, when the interested sample area is larger than the beam size, the beam size has to be reduced by compromising that the beam is not parallel. This situation is called microdiffraction mode.

CHAPTER 4
PULSED LASER DEPOSITED Zn_2GeO_4:Mn

4.1 Introduction

Full-color ACTFEL displays require higher brightness of the green phosphors to match the high brightness of the available red phosphors.[17] So far, the best green phosphor for ACTFEL displays is ZnS:Tb^{3+}. Oxide phosphors doped with Mn^{2+} are among the promising green phosphor candidates for ACTFEL devices.[42] Oxide phosphors have the features: 1) larger band-gap than that of sulfide phosphors;[47] 2) chemically more stable than sulfide phosphors;[61] 3) less vacuum-restricted thin film growth;[69] and 4) high temperature processing required.[42] These features could be good and bad for the performance of ACTFEL devices. So far, the best green oxide phosphor is $Zn_2Ge_{0.5}Si_{0.5}O_4$:Mn.[42] In this dissertation, Zn_2GeO_4:Mn was investigated. Its processing temperature is the lowest among the available green oxide phosphors.[42] So far, the deposition techniques used for Zn_2GeO_4:Mn thin film growth include sputtering deposition[42] and sol-gel coating.[69] There have been no reports of pulsed laser deposition used for oxide ACTFEL devices. Pulsed laser deposition was used in an investigation of photoluminescence of $ZnGa_2O_4$:Mn on single crystal substrates such as $MgAl_2O_4$.[77] Pulsed laser deposition has been commonly used for oxide materials, especially for oxide superconducting materials for a while.[49] Pulsed laser deposition features the good stoichiometry of the film compared to the target, short down time and low cost compared

with MBE (molecule beam epitaxy), and non-equilibrium growth due to the interaction of the target with high laser energy.[54]

Experimental procedure of Zn_2GeO_4:Mn pulsed laser deposition has been given in Section 3.3.2.. The experimental results of Zn_2GeO_4:Mn pulsed laser deposition include the results from the Zn_2GeO_4:Mn target and from the Zn_2GeO_4:Mn films deposited at different deposition conditions including laser energy density, ambient pressure, substrate temperature and substrate material, and different annealing temperature and time. The pulsed laser deposited Zn_2GeO_4:Mn were characterized by optical, electrical, structural and chemical techniques.

4.2 Experimental Results

4.2.1 Zn_2GeO_4:Mn Target

4.2.1.1 X-ray Diffraction

The Zn_2GeO_4:Mn powder was pre-fired at 1150^{o}C for 24hrs. before hydraulically pressed into a target and post-fired at 1050^{o}C for 24 hrs. after pressing. The crystal structure of the Zn_2GeO_4:Mn target after firing was identified by x-ray diffraction. The x-ray diffraction pattern of the Zn_2GeO_4:Mn target is shown in Figure 4-1 together with one of the two reference Zn_2GeO_4 rhombohedral patterns. The x-ray diffraction pattern of the Zn_2GeO_4:Mn target indicates that the Zn_2GeO_4 crystal structure is formed since all the peaks from the target match well those of the Zn_2GeO_4 rhombohedral reference. However, some of the peaks from target are shifted compared with the Zn_2GeO_4 rhombohedral reference peaks. Especially, these peaks at high 2θ have a even larger shift

which is up to 2°. The Zn_2GeO_4 is well crystallized after the two firing processes at 1150°C and 1050°C before and after pressing since the intensity for all the peaks is relatively strong.

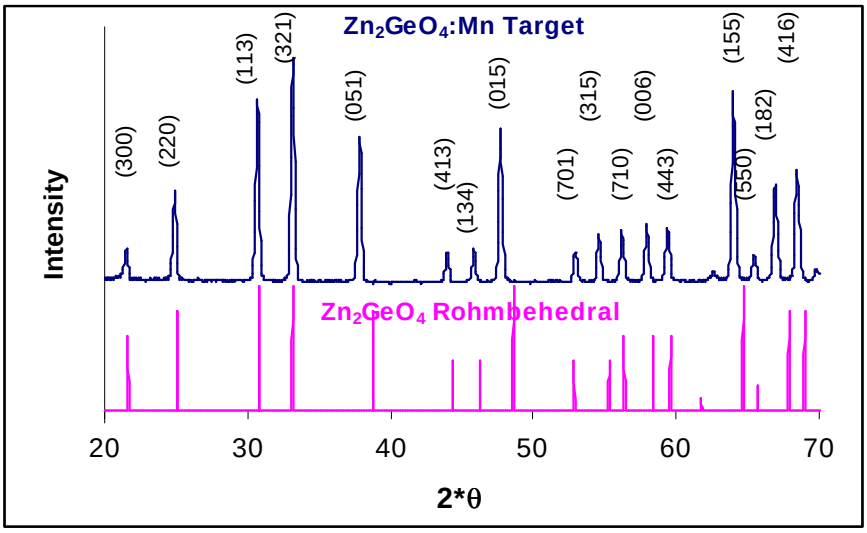

Figure 4-1 X-ray diffraction pattern of Zn_2GeO_4:Mn target compared with the pattern of Zn_2GeO_4 rhombohedral reference[36]

4.2.1.2 PL and PLE Spectra

Photoluminescence emission spectrum (PL) and photoluminescence excitation spectrum (PLE) of the Zn_2GeO_4:Mn target were measured. A monochromatized light source was available for the PL and PLE measurement which were completely automated. The PL spectrum is the emission spectrum at a constant excitation wavelength. The PLE spectrum is the excitation spectrum at a constant emission wavelength. Before an optimum excitation wavelength is identified, an excitation wavelength 325nm was applied initially. Excited by 325nm excitation wavelength, the Zn_2GeO_4:Mn target emits the green light and the PL emission spectrum was obtained

with a strong and broad peak at 540 nm. When the excitation wavelength is changed from 325nm to 540nm, the emission peak intensity at 540nm is changed accordingly. The excitation spectrum was therefore for the emission peak at 540nm. The excitation peak was seen at 340nm . The final PL emission spectrum was obtained at this optimum excitation wavelength 340nm rather than at 325nm. The PL and PLE spectrum of the Zn_2GeO_4:Mn target is shown Figure 4-2. One broad peak at 540nm is seen in the photoluminescence emission spectrum of the Zn_2GeO_4:Mn target and one broad peak at 340nm is seen in the photoluminescence excitation spectrum of the target. The emission peak wavelength and excitation peak wavelength is associated with the transition of the luminescent center Mn^{2+} in host Zn_2GeO_4.

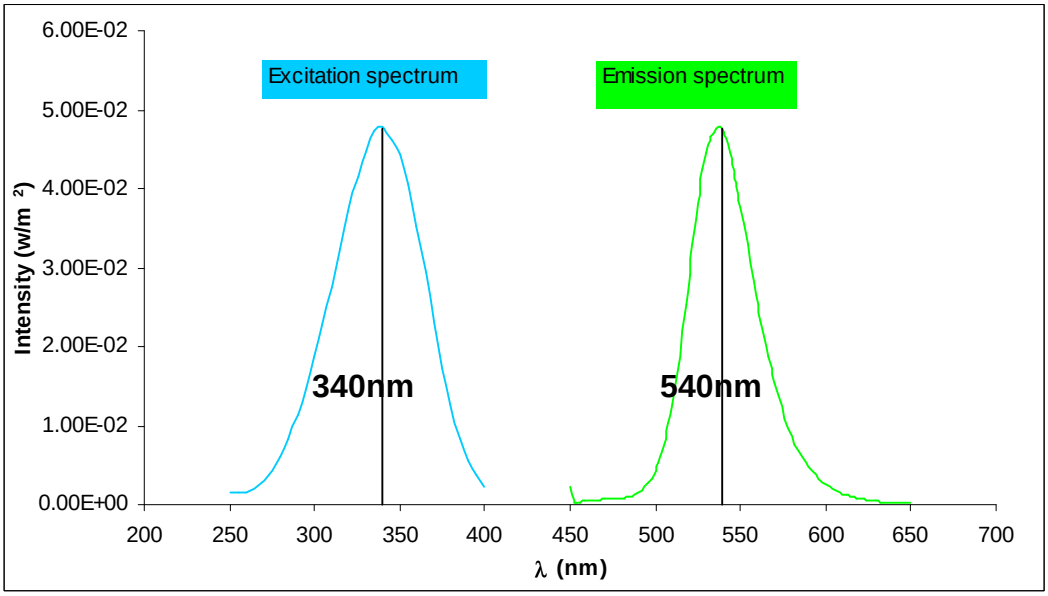

Figure 4-2 Photoluminescence emission and excitation spectrum of Zn_2GeO_4:Mn target

4.2.1.3 PL of Ablated Zn_2GeO_4:Mn Target

After ablation by the pulsed laser, the originally white Zn_2GeO_4:Mn target became dark. Oxygen loss at the target surface could be the reason for the color change. Excited by a UV lamp, the photoluminescence of the unablated (fresh) Zn_2GeO_4:Mn target was bright green color, while the PL of the ablated target was a dim green color. The PL spectra for the two cases are shown in Figure 4-3. Both the unablated and the ablated target show a broad peak at 540nm, which is in the green region. The peak from the ablated Zn_2GeO_4:Mn target is much lower than that from the unablated target . The small peak at 390nm is from the UV lamp background. The reduced PL intensity probably result from the oxygen loss on the target surface after ablation.[49]

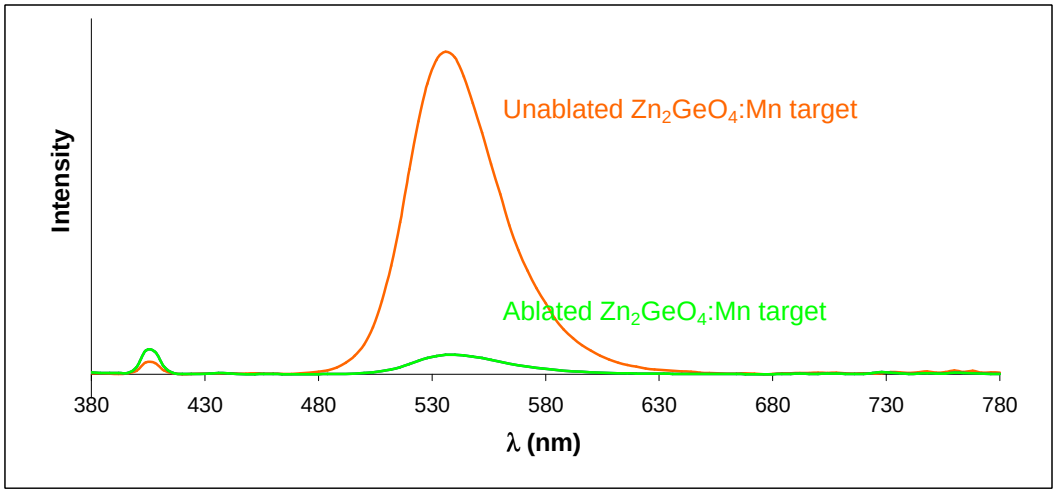

Figure 4-3 Photoluminescence emission spectrum of unablated and ablated Zn_2GeO_4:Mn target under excitation of ultra-violet lamp

4.2.2 PZT Substrate

4.2.2.1 SEM

A PZT substrate was used for the Zn_2GeO_4:Mn ACTFEL inverted device structure. This substrate is a 0.2mm Al_2O_3 ceramic sheet with a 2000Å Au layer and a

20μm $Pb(Zr_{0.5}Ti_{0.5})O_3$ (PZT) layer. The yellowish PZT layer is comprised of two layers: a thin bottom PZT layer prepared by spin-coating and a thick top PZT layer prepared by screen printing for a total thickness of 20μm. The screen printing PZT layer is expected to result in a rough surface. The plain view and cross section of the PZT substrate were obtained using SEM and they are shown in Figure 4-4. The thickness of PZT was first measured by profilometry and 20μm was measured from PZT layer step on Au layer. The cross section SEM image of the PZT substrate further confirmed that the thickness of PZT layer was 20μm. The cross section SEM image indicates that the PZT layer is porous. The Al_2O_3 substrate is even more porous. However, the Al_2O_3 substrate's physical properties except its refractory nature are almost irrelevant to the optical performance of Zn_2GeO_4:Mn ACTFEL devices. The primary reason to use Al_2O_3 as substrate for Zn_2GeO_4:Mn ACTFEL devices was that it could be heated up to high temperatures (up to 1150^oC). The top plain view SEM image of the PZT substrate indicates that the PZT substrate surface is not smooth at all. Many bumps and valleys are seen on surface of the PZT layer. Their average feature size is 5μm . Their depth however cannot be is identified from the plain view image. The rough surface is likely the result of the screen printing. The Au layer is not seen in the cross section of the PZT substrate probably because it is too thin to be seen or the patterned Au area did not cross this section of the cross section.

4.2.2.2 X-ray Diffraction

X-ray diffraction from the PZT substrate was obtained. Only part of the surface area of the 2"x 2" Al_2O_3 substrate was covered by the Au layer and the PZT layer. The x-ray

diffraction pattern of the PZT substrate together with the $Pb(Zr_{0.52}Ti_{0.48})O_3$ reference pattern[36] is shown in Figure 4-5.

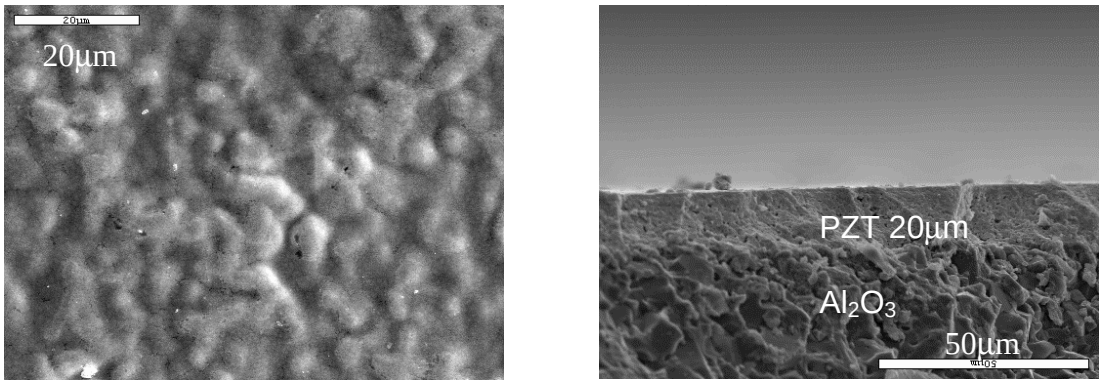

Figure 4-4 Plain view and cross-section of substrate Al_2O_3/Au/$Pb(Zr_{0.5}Ti_{0.5})O_3$

The x-ray diffraction pattern of the PZT substrate shows that the PZT layer is well crystallized since all the peaks from the PZT layer are strong; the PZT layer peaks match those from a $Pb(Zr_{0.52}Ti_{0.48})O_3$ crystalline reference. It should be noted that all the peaks from the PZT substrate come from the top 20µm thick PZT layer since its thickness is larger than the typical penetration depth of x-ray diffraction (10µm).[75] This means that x-ray don't penetrate into the PZT layer and no x-ray diffraction from the underlying Au or the Al_2O_3 substrate were detected.

4.2.2.3 Composition

The energy dispersive x-ray spectrum was used to confirm the composition of the PZT layer which was carbon coated before analysis. The EDX spectrum was obtained at electron acceleration voltage 15kV and is shown in Figure 4-6. This data indicate that the PZT layer contains Pb, Zr, Ti O and Si. The C is from the carbon coating. A Si peak is observed at around 2.5keV.

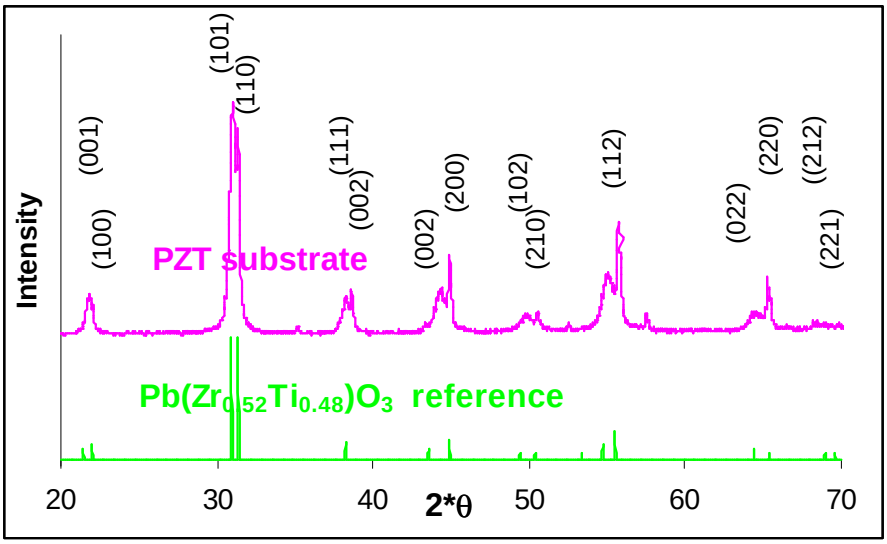

Figure 4-5 X-ray diffraction pattern of $Pb(ZrTi)O_3$, compared with $Pb(Zr_{0.62}Ti_{0.48})O_3$ reference crystal structure

The small amount of Si in the PZT layer could be from the Si-based organic binder which was typically used during screen printing.

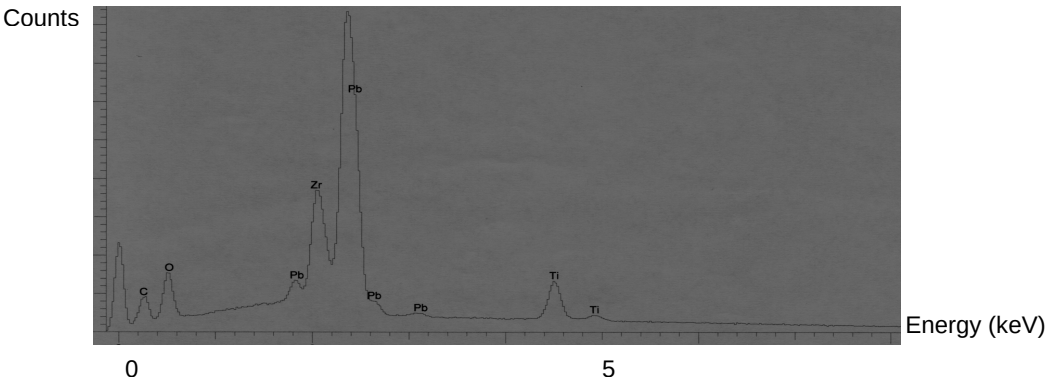

Figure 4-6 Energy dispersive x-ray spectrum of the PZT layer from substrate Al_2O_3/Au/PZT

4.2.3 Zn_2GeO_4:Mn Film Track-table

Zn_2GeO_4:Mn thin films were PLDed in two different systems, one at the University of Florida and one at the Naval National Lab. Pulsed laser deposited films from the University of Florida were primarily characterized by photoluminescence of Zn_2GeO_4:Mn on silicon. Pulsed laser deposition at NRL were primarily characterized by electroluminescence of Zn_2GeO_4:Mn on glass/ITO/ATO and on Al_2O_3/Au/Pb($Zr_{0.5}Ti_{0.5}$)O_3. The use of the PZT substrate was to withstand higher annealing temperatures up to 950^{o}C.([63]) All pulsed laser deposited films used in the chapter are listed in Table 4-1 for easy tracking.

4.2.4 Zn_2GeO_4:Mn on Si – Substrate Temperature Issue

Processing of Zn_2GeO_4:Mn at >= 800^{o}C is required for crystallization.[42] A single crystal (100) silicon wafer was initially used as substrate for Zn_2GeO_4:Mn thin film growth. Si can be heated up to 1100^{o}C without substantial degradation or diffusion. [78] Another advantage of using silicon substrate is that many x-ray diffraction peaks from the polycrystalline Zn_2GeO_4:Mn film can be easily isolated from the single crystal silicon background peak(s) rather than from the complicated and possibly overlapped polycrystalline PZT background peaks. It was expected that the film quality of Zn_2GeO_4:Mn deposited on silicon would be much better than if deposited on glass/ITO/ATO since the Zn_2GeO_4:Mn grows on the single crystal surface rather than on the ATO amorphous surface. Two different substrate temperatures were used for Zn_2GeO_4:Mn film growth, 250^{o}C (Sample UF-Si-1) and 800^{o}C (Sample UF-Si-2). All other deposition parameters and the detailed deposition parameters are referred to Table 4-1.

Table 4-1 Tracking table of pulsed laser deposited Zn_2GeO_4:Mn at UF and NRL

	Zn_2GeO_4 deposition	**Annealing**	**Characterization**
UF-Si-1	Si sub., 250°C $5*10^{-5}$T, 200mT O_2 1.6J/cm^2, 36,000 pulses	800°C, air, 24hrs	PL, XRD, SEM, EDX
UF-Si-2	Si sub., 800°C $5*10^{-5}$T, 200mT O_2 1.6J/cm^2, 36,000 pulses	No	PL, XRD, SEM, EDX
UF-ATO-2	Si sub., 800°C $5*10^{-5}$T, 200mT O_2 1.6J/cm^2, 36,000 pulses	No	SEM, EDX
NRL-PZT-1	PZT sub., 250°C $5*10^{-5}$T, 200mT O_2 0.8J/cm^2, 10,000 pulses	750°C, 2.5hrs N_2 and air	PL, EL*, XRD, SEM
NRL-PZT-2	PZT sub., 250°C $5*10^{-5}$T, 150mT O_2 0.8J/cm^2, 10,000 pulses	770°C, air, 10 min.	PL, EL*, XRD, SEM
NRL-PZT-3	PZT sub., RT $5*10^{-5}$T, 150mT O_2 0.8J/cm^2, 10,000 pulses	750°C, air, 2.5hrs.	PL, EL*, XRD, SEM
NRL-PZT-4	PZT sub., 800°C $5*10^{-5}$T, 150mT O_2 0.8J/cm^2, 10,000 pulses	No	PL, EL*, XRD, SEM
NRL-ATO-1	glass/ITO/ATO sub., 250°C $5*10^{-5}$T, 200mT O_2 0.8J/cm^2, 10,000 pulses	RTA, Ar, 1min.	PL, EL*, XRD, SEM
NRL-ATO-2	glass/ITO/ATO sub, 250°C $5*10^{-5}$T, 200mT O_2 1.6J/cm^2, 10,000 pulses	RTA, Ar, 1min.	PL, EL*, XRD, SEM
NRL-Si-1	Si sub., RT $5*10^{-5}$T, 150mT O_2 0.8J/cm^2, 10,000 pulses	800°C, air, 21hrs.	Thickness, XRD
NRL-Si-2	Si sub., 800°C $5*10^{-5}$T, 150mT O_2 0.8J/cm^2, 10,000 pulses	No	Thickness

*EL device is half-cell structure and the top conducting layer is either Al dot for glass/ITO/ATO substrate and or ITO for Al2O3/Au/PZT substrate.

Typically the number of the laser shots was given constant instead of laser repetition rate and deposition time. The film thickness is a function of laser energy density and the

number of laser pulses. The film crystallization is generally dependent on the substrate temperature. High substrate temperature dramatically enhances film crystallization during growth.[48] However, the film generally becomes less stoichiometric at high substrate temperatures, which is especially true for pulsed laser deposition.[48, 79,80] Zn_2GeO_4:Mn films deposited at low temperatures tend to be amorphous. Re-crystallization is expected upon an annealing at high temperatures. The films deposited at 250^oC and then annealed at 800^oC is compared with the film deposited at 800^oC.

4.2.4.1 Photoluminescence

Photoluminescence of the Zn_2GeO_4:Mn films deposited at 250^oC (UF-Si-1) and 800^oC (UF-Si-2) was obtained under excitation of UV lamp and their PL spectra are shown Figure 4-7. The film deposited at 250^oC was annealed at 800^oC in two different ambient gases N_2 and air. The PL spectrum of the Zn_2GeO_4:Mn target is plotted here for comparison. Since the intensity of the target is so much stronger that of the films, the insert shows intensity plotted on a larger scale to accommodate the whole PL spectrum of the target. The first observation from Figure 4-7 is that both the films, annealed and deposited at 800^oC, demonstrate a broad PL emission peak at 540nm. Another observation is that both films demonstrate a much lower PL intensity than that of the target. These observations can be explained by that 1) the target surface is much rougher than the films, which enhances light outcoupling; and 2) The amount of Zn_2GeO_4:Mn contained in the target is much greater than that in the films and 3) The target is much better crystallized than the films since it was fired at higher temperatures for a much longer time. The interesting evidence here is that the film annealed at 800^oC shows a stronger photoluminescence than that deposited at 800^oC. Crystallization of Zn_2GeO_4:Mn

deposited at 800°C should be definitely better than that deposited at 250°C. In this case, the better photoluminescence for the annealed film should be contributed by the post-annealing at 800°C for 24hrs which might have resulted in a good re-crystallization. Cystallinity is the critical structural parameter for PL and EL materials. If the film is poorly crystallized, the luminescent center is more likely to relax back to the ground state by giving out the energy non-radiatively through grain boundaries or defects.

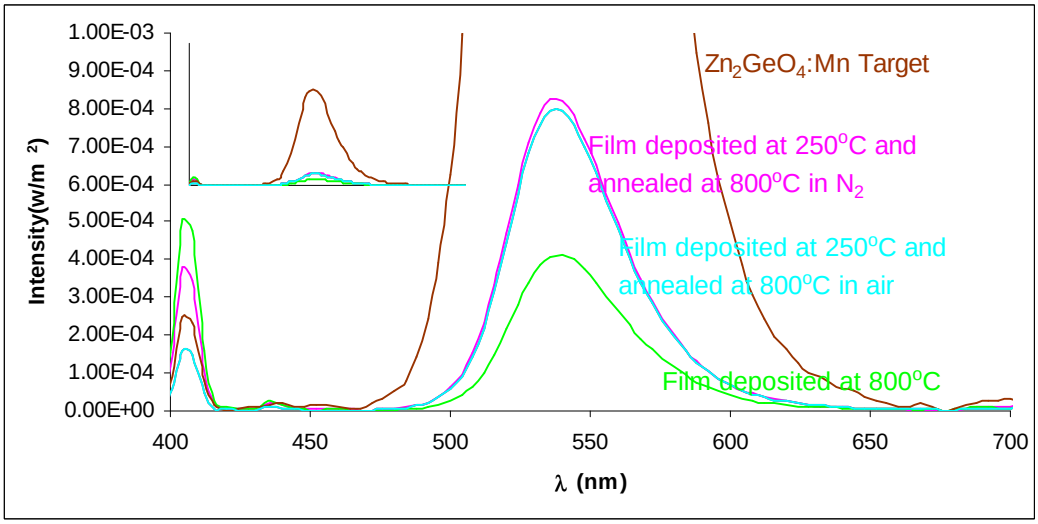

Figure 4-7 Photoluminescence emission spectrum of Zn_2GeO_4:Mn film deposited at 1) 250°C (followed by an annealing at 800°C) (UF-Si-1) and 2) deposited at 800°C without any annealing I(UF-Si-2)

The film annealed at 800°C in N_2 was annealed a second time in air at 800°C. It has been reported that oxygen vacancy played the shallow donor level to enhance excitation efficiency of the luminescent center,[73] which suggests that more oxygen in Zn_2GeO_4:Mn is not necessarily good for optical performance. However, there was no significant change in PL intensity after the second anneal in air.

There are several reasons that films annealed at 800°C demonstrate a much better PL intensity than those deposited at 800°C. The hypotheses include 1) possible thickness

difference; 2) possible crystallinity difference 3) and possible surface roughness difference. The x-ray diffraction can give a better picture how well a film is crystallized. Regarding surface roughness difference, the substrate temperature difference could make film surface roughness different. Re-crystallization during annealing would make the film surface much rougher, compared with the as-deposited film.

The first hypothesis is thickness difference. No direct information is available to compare the thickness of the two films Sample UF-Si-1 and UF-Si-2. The film deposited at 250^{o}C was 10,000Å given by profilometry using a step formed during deposition. No thickness data was available for the film deposited at 800^{o}C.

Zn_2GeO_4:Mn pulsed laser deposition on Si was also done at NRL. The substrate temperatures were room temperature (NRL-Si-1) and 800^{o}C(NRL-Si-2). In order to do comparison with sputter deposited Zn_2GeO_4:Mn films which were all grown at room temperature, the pulsed laser deposited Zn_2GeO_4:Mn film was especially grown at room temperature. The deposition condition was slightly different from those from UF. The system is different. The number of the laser shots here were 10,000 shots. While, UF laser pulses in term of the laser repetition (10Hz) and the deposition time (30 min.), the total laser shots should be 36,000 shots. This means even if the other parameters (the position and the distance of substrate relative to the target) are exactly the same, the film thickness should be only less than 1/3 of the UF films.

The photoluminescence was obtained from the films by using UV lamp excitation source. The Zn_2GeO_4:Mn film deposited at R.T. didn't show any PL. This result is not surprising. Since the x-ray diffraction of this film shown above is amorphous no crystallization of Zn_2GeO_4:Mn should have been obtained during film growth. The

photoluminescence was obtained after the film was annealed at 800°C for 21 hours and its PL spectra is shown in Figure 4-8. The broad peak at 540nm is seen in this film. The background UV lamp reflection is plotted as a reference.

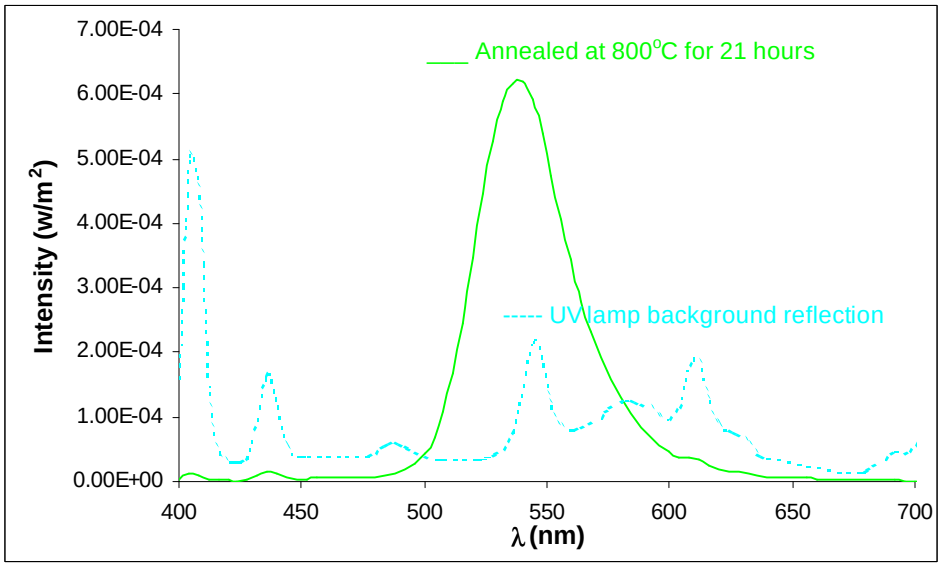

Figure 4-8 Photoluminescence spectrum of the Zn_2GeO_4:Mn film deposited on Si at R.T.(NRL-Si-1) and annealed at 800°C for 21hrs.

4.2.4.2 X-ray Diffraction

X-ray diffraction from the two films and the Si substrate is shown in Figure 4-9. The x-ray diffraction pattern of the Zn_2GeO_4:Mn target is shown for comparison. The film deposited at 250°C doesn't show any peaks except a huge peak at 69°, which is the Si (400) peak. This observation implies that Zn_2GeO_4:Mn deposited at 250°C is amorphous. After being annealed at 800°C for 24hrs, the 250°C deposited film exhibits all the rhombohedral Zn_2GeO_4 peaks when compared with the rhombohedral Zn_2GeO_4:Mn target. It should be noted that the x-ray diffraction peaks from the film are slightly shifted to the right compared with those from the target. The 2θ shift occurs probably because the sample height was when x-ray diffraction was being detected. It

should be noted as well that Si (400) peak disappears in the 800^{o}C annealed film, which implies that the Zn_2GeO_4:Mn layer might have reacted with part of its underlying Si substrate to form $Zn_2Ge_{1-x}SiO_4$:Mn which should demonstrate a much higher photoluminescence or electroluminescence.[42] The peaks from the film deposited at 800^{o}C are strong and match well the peaks from the target as well. This implies that Zn_2GeO_4:Mn was well crystallized at substrate temperature 800^{o}C. It is observed in this film that the peak at 34^{o} which is corresponding the Zn_2GeO_4 rhombehedral (321) crystal plane is much stronger than any other peaks. This implies that even if Zn_2GeO_4 grown at 800^{o}C is polycrystalline it is textured at (321) which is parallel to the wafer surface. It is clear that rhombohedral Zn_2GeO_4 crystal structure is formed in both the 800^{o}C annealed and the 800^{o}C deposited films. The FWHM defines of the $2\theta = 34^{o}$ (321) peak for crystallinity comparison. The $\Delta 2\theta$ for the film deposited at 800^{o}C is smaller than that for the film annealed at 800^{o}C. This implies that the film deposited at 800^{o}C is slightly better crystallized than that annealed at 800^{o}C. Therefore, in term of crystallinity, the film deposited at 800^{o}C should demonstrate a stronger PL than that annealed at 800^{o}C. However, the result is reversed. The x-ray diffraction pattern of the films on Si (Sample NRL-1) is shown in Figure 4-10. One large peak appears in the x-ray diffraction pattern of the film deposited at room temperature. The Zn_2GeO_4:Mn film deposited at 250^{o}C given in Figure 4-9 was amorphous. It is obvious that the film deposited at R.T. is amorphous too. This large peak should be from the single crystal Si substrate. Upon an annealing at 800^{o}C for 21hrs., the Si peak height is reduced and the new peaks appear. Compared with the peaks from the Zn_2GeO_4:Mn target which is in the Zn_2GeO_4

rhombehedral structure, the major Zn_2GeO_4 rhombohedral peaks appear in the annealed film.

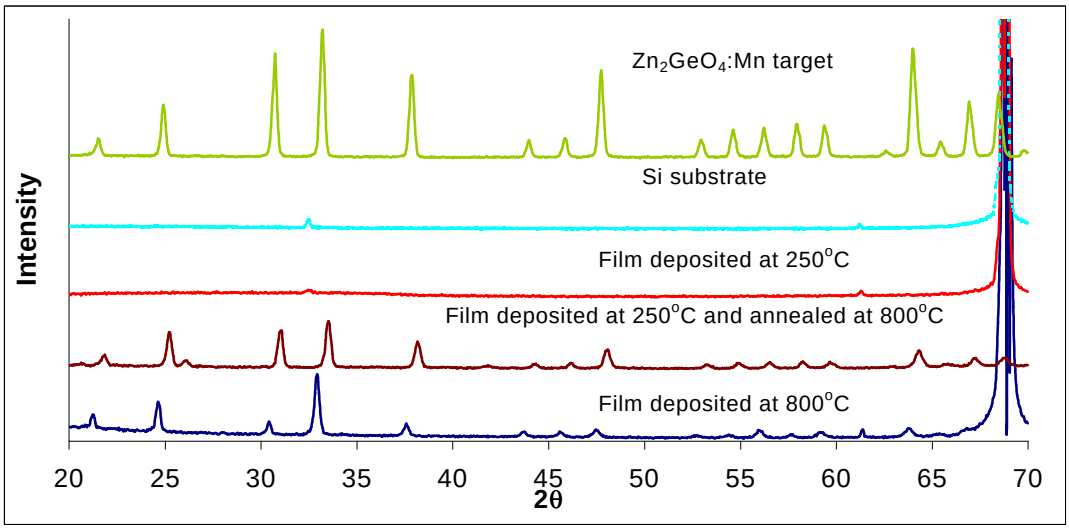

Figure 4-9 X-ray diffraction pattern of pulsed laser deposited Zn_2GeO_4:Mn at substrate temperature 1) 250°C (UF-Si-1) and 2) then annealed at 800°C, and 3) deposited at 800°C (UF-Si-2)

The reduced Si peak intensity implies that the underlying Si might have reacted with Zn_2GeO_4 during annealing. Re-crystallization during annealing definitely occurred since several new peaks appear. However, the re-crystallization is not thoroughgoing since the intensity of the new peaks appears not strong.

4.2.4.4 Surface Topography

Another possible reason for difference in PL intensity is difference of film surface roughness which would result in the difference of light out-coupling.[46] The surface morphology was imaged by SEM as shown in Figure 4-11. The film annealed at 800°C

for 24hr appears much more rough with islands of materials. The film deposited at 800°C appears smooth, but not continuous.

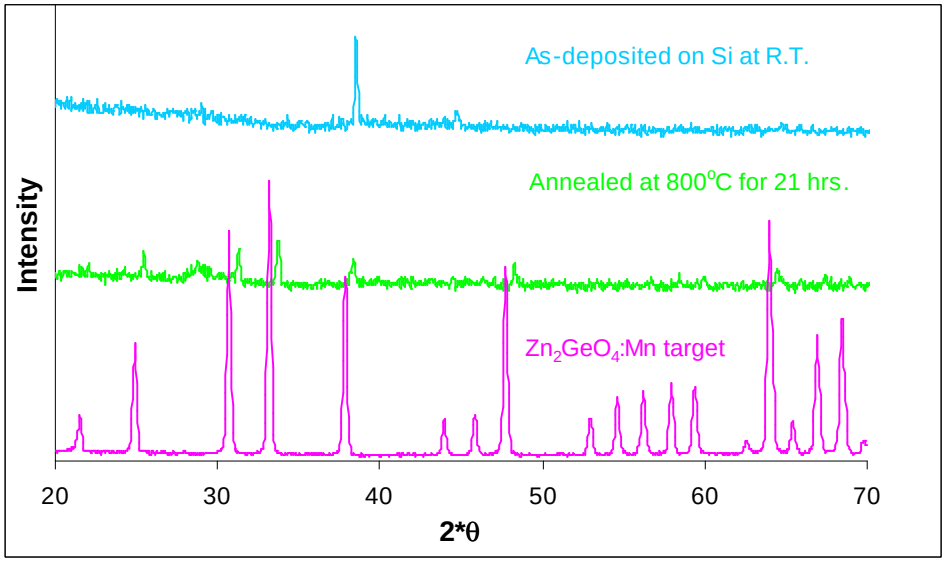

Figure 4-10 X-ray diffraction of pulsed laser deposited Zn_2GeO_4:Mn on Si 1) at substrate temperature R.T. (NRL-Si-1) and 2) followed by an annealed at 800°C

A large quantity of voids are seen on the surface. The non-continuous film surface refers that the film was growing by the islands growth mechanism instead of the layer-by-layer growth mechanism.[81] However, in general this film surface is smoother compared with that annealed at 800°C. Therefore, the rougher surface should be partially responsible for the increased PL intensity in the film annealed at 800°C.

4.2.4.5 Composition

Generally, films deposited at higher temperature tend to be less stoichiometric deposition due to higher vapor pressure at higher temperature. This is especially true for pulsed

laser.[52] The chemical composition of the two films was analyzed by Energy dispersive x-ray spectroscope.

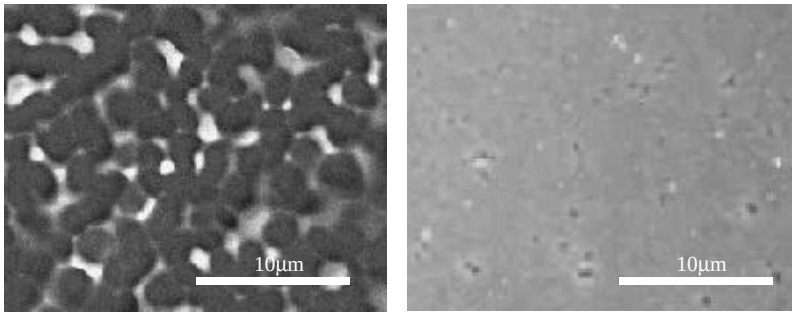

a) b)

Figure 4-11 SEM image of pulsed laser deposited Zn_2GeO_4:Mn film on silicon at two different substrate temperatures a) 250°C (followed by an annealing at 800°C)(UF-Si-1), and b) 800°C(UF-Si-2)

The EDX spectrum of the two films together with that of the target is shown in Figure 4-12. The 800°C annealed film was the one originally deposited at 250°C. The characteristic x-ray spectrum was obtained under excitation of 15KeV electrons. The characteristic x-ray peaks of Zn, Ge, O, Mn and C are seen. The carbon peak is from carbon coating which was used to improve the sample conductivity. Two strong peaks are identified as Zn. One is Zn-Kα at 1.25KeV and the other is Zn-Lα at 8KeV. The same is to the two Ge peaks. One is Ge- Kα at 1.3KeV and the other is Ge-Lα at 9.5KeV. A strong O peak and a small Mn peak was observed at 1.0KeV and 4.9KeV. The EDX software gave the atomic percentage of all the detected elements automatically. The Zn/Ge atomic ratio was therefore obtained according to the individual element atomic percentages. The EDX spectrum of the target powder indicates a Zn/Ge ratio of 3.27, which is much higher than the stoichiometric Zn/Ge ratio of 2.00 expected from Zn_2GeO_4. This Zn/Ge from the target might be not accurate since the target powder has a

much larger porosity density than the film's. The detected characteristic x-ray yield is dependent on porosity density. Therefore, the Zn/Ge ratio 3.27 is not recommended as the reference to compare with either of the films. The Zn/Ge ratio of the two films is 0.83 for substrate temperature 250^{o}C and 0.77 for substrate temperature 800^{o}C. According to the quantitative analysis results, both of the films are Zn-deficient and the film deposited at 800^{o}C is more Zn-deficient than that deposited at 250^{o}C and annealed at 800^{o}C.

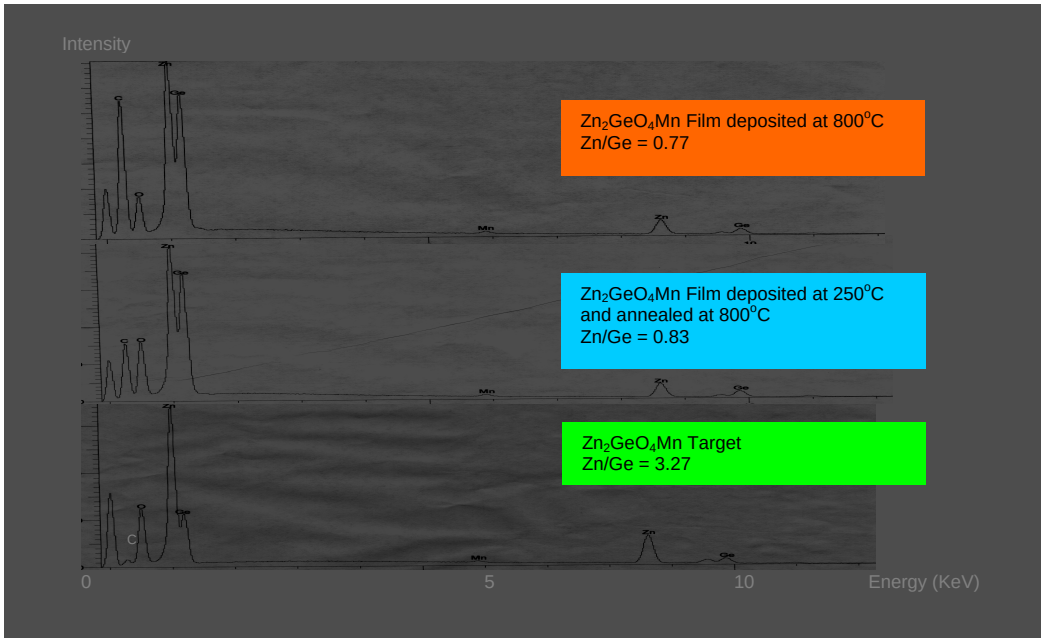

Figure 4-12 Energy dispersive X-ray spectrum of pulsed laser deposited Zn_2GeO_4:Mn deposited on silicon at 1) at 250^{o}C (UF-Si-1) and 2)800^{o}C (UF-Si-2)

4.2.5 Zn_2GeO_4:Mn on Glass/ITO/ATO – Substrate Issue

Zn_2GeO_4:Mn was also deposited on glass/ITO/ATO in order to form an EL device. It was grown at substrate temperature 800^{o}C. The deposition parameters were

same as the Zn_2GeO_4:Mn film deposited on Si at 800^oC: laser density 1.6J/cm^2, ambient O_2 200mT, laser repetition 10Hz and deposition time 30 minutes.

4.2.5.1. SEM

The information about film surface morphology was obtained from the SEM image (Sample UF-ATO-1). The SEM image of this film is given in Figure 4-13 and compared with the film deposited on Si (Sample UF-Si-2, Figure 4-11 (b). The dent parts on the surface of the film deposited on glass/ITO/ATO are the result of Al dot burning when it was being tested for EL performance. The crystallite grain size of this film appears larger than that deposited on Si. However, no voids are seen in the surface of the film deposited on glass/ITO/ATO. It is evident that continuous and dense Zn_2GeO_4:Mn crystallites are formed on glass/ITO/ATO at 800^oC.

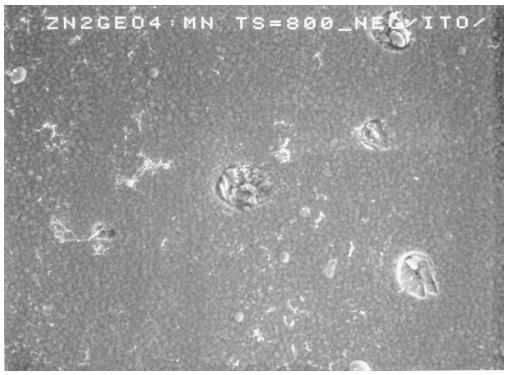

Figure 4-13 SEM image of Zn_2GeO_4:Mn deposited at substrate temperature 800^oC on glass/ITO/ATO substrate (UF-ATO-1)

4.2.5.2 Composition

The Zn/Ge ratios from these films obtained from EDX are listed in Table 4-2 and compared those from the film deposited at Si. As shown in Table 4-2, both films

demonstrate a Zn deficiency. The film deposited on glass/ITO/ATO is slightly more Zn-deficient than that deposited on Si which may be within experimental error.

Table 4-2 EDS quantitative analysis of pulsed laser deposited Zn_2GeO_4:Mn at 800^oC on two different substrates: 1) Si and 2) glass/ITO/ATO

Elements in Zn_2GeO_4:Mn(at.%)	Stoichiometric Zn_2GeO_4:Mn	1) Deposited at 800^oC on Si (UF-Si-2)	2) Deposited at 800^oC on glass/ITO/ATO (UF-ATO-1)
Zn		23.47	15.11
Ge		30.43	20.96
O		46.11	63.93
Zn/Ge ratio	**2.00**	**0.77**	**0.72**

4.2.6 Zn_2GeO_4 on glass/ITO/ATO – Laser Energy Density Issue

Zn_2GeO_4:Mn was deposited on glass/ITO/ATO and a top Al dot deposited to form standard half-stack ACTFEL device. Zn_2GeO_4:Mn was deposited at 250^oC, crystallinity was improved by rapid thermal annealing at 800^oC in Ar for 1 min. For standard EL device, the emitted light comes out of the transparent glass substrate side.

Zn_2GeO_4:Mn was deposited at two different laser power densities, 0.8 J/cm^2 (Sample NRL-ATO-1) and 1.6 J/cm^2(Sample NRL-ATO-2). Generally, the deposition rate is proportional to the laser density applied. This means that the higher deposition rate accompanies the higher laser density. Except for the laser density, other deposition parameters are the same. The laser energy density can be varied by changing two parameters either laser energy or laser focal size. When the laser energy is fixed, the laser energy density is inversely proportional to the focal size. This means that the smaller focal size, the larger laser density is. The laser waveform used here was triangle

waveform and its magnitude and pulse duration could be adjusted depending on the physical properties of the target used such as optical absorption coefficient, thermal conductivity and melting point etc . The triangle laser waveform is shown in Figure 4-14 . The area of the triangle area gives the laser energy. Sometimes, people are only interested in laser energy since the laser focal size is typically fixed. In our case, the laser energy for the two films was 800mJ and 1600mJ respectively based on the fixed focal size of 1.0cm^2. The laser duration time can range from 20ns to 200ns. In this case, the laser density by time is huge since the laser duration time is extremely short. For instance, the laser density by time is 4x10^8 J/cm^2-s for the laser density 0.8J/cm^2 and the laser duration time 20ns.

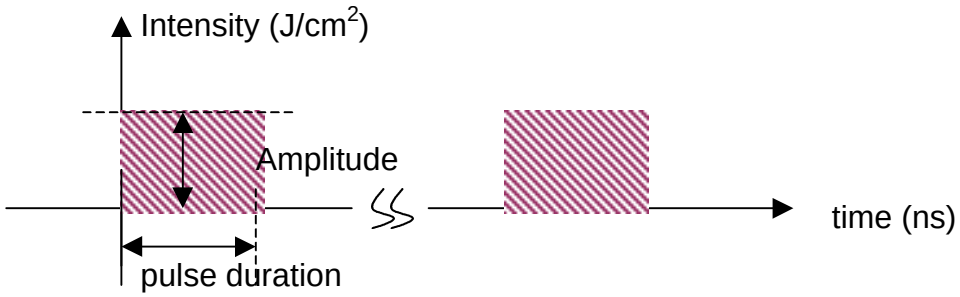

Figure 4-14 Schematic diagram of laser pulse shape

The two films were annealed by lamp-based furnace at 800^{o}C in Ar ambient for 1 min. The annealing temperature and time applied for films deposited on glass/ITO/ATO were restricted by the transition temperature of the substrate glass NEG to <= 850^{o}C and the substantial degradation of ITO at 850^{o}C.[46] The annealing temperature vs. time for this lamp-based furnace is shown in Figure 4-15.

The ramping time from room temperature to 800^{o}C was set for 3 minutes. The ramping time was restricted by the power of the pair of lamps. Generally, it takes 2 minutes to reach 700^{o}C and 3 minutes to reach 800^{o}C at the lamps' full power. The lamp-based furnace allowed a much faster ramping rate than the box furnace.

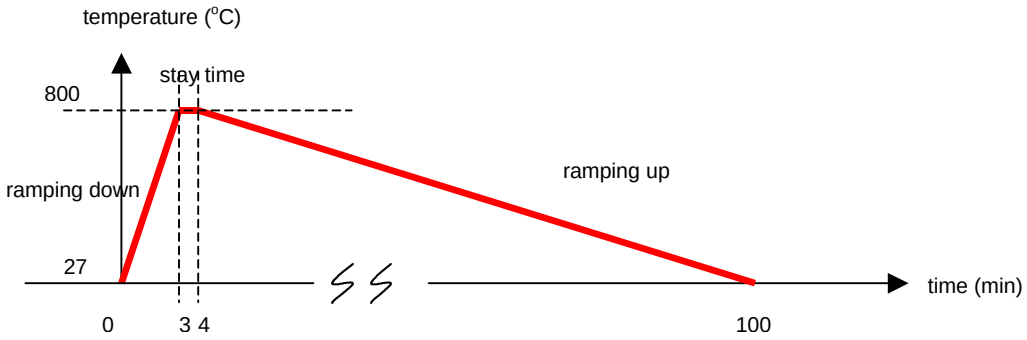

Figure 4-15 Temperature vs. time curve of lamp-based furnace

4.2.6.1 Photoluminescence

Photoluminescence spectrum for the two films deposited on glass/ITO/ATO were measured by UV lamp at major wavelength 254nm and are shown in Figure 4-16. Both PL spectra demonstrate a broad peak at 540nm, which is the transition of Mn^{2+} in host Zn_2GeO_4 from ^4T to ^6A. The one deposited at laser density 1.6J/cm^2 is brighter than that at 0.8J/cm^2. This observation is obvious since the former one is almost double thicker than the latter one. The doubled laser density 1.6J/cm^2 resulted in a doubled deposition rate.

4.2.6.2 Electroluminescence (Luminance vs. Voltage)

Electroluminescence was measured for the two films at a voltage pulse frequency of 2.5KHz. The luminance vs. voltage (L-V) curve was obtained only from film deposited at

0.8J/cm^2, because the film deposited at 1.6J/cm^2 burned out after emitting the light. When the heat is accumulated by high frequency voltage, the Al dot is first burned out before any other layers are burned.

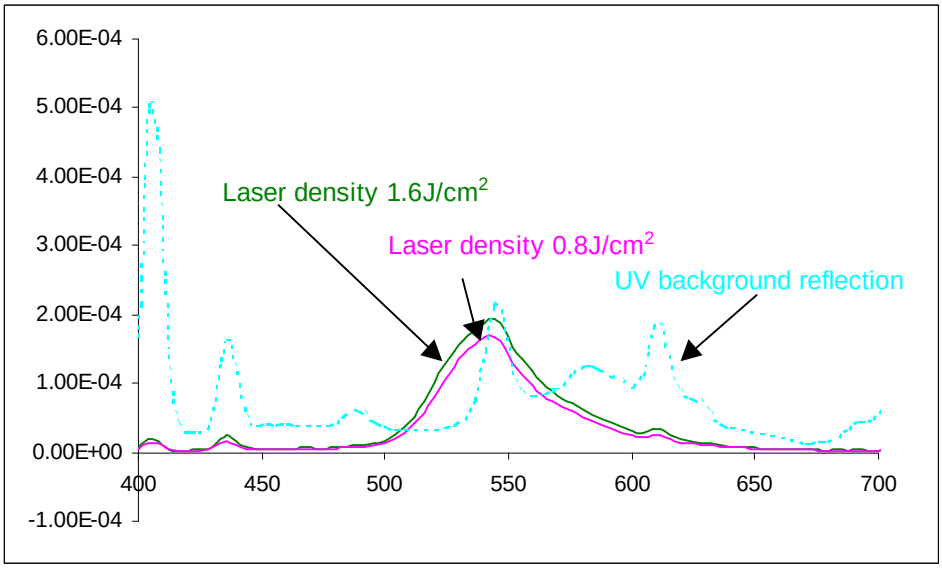

Figure 4-16 Photoluminescence emission spectrum of pulsed laser deposited Zn_2GeO_4:Mn on glass/ITO/ATO. The films were deposited at laser density 1.6J/cm^2 (NRL-ATO-2) and 0.8J/cm^2 (NRL-ATO-1)

The reason of using 2.5KHz for the two films is because they can be compared with the films deposited on PZT which were all measured at 2.5KHz. The one deposited at 1.6J/cm^2 was coated with Al after a longer time when the Zn_2GeO_4:Mn. layer was deposited. The Zn_2GeO_4:Mn could be contaminated or covered with a large density of dirt which made Al tend to be shorted.

4.2.6.3 X-ray Diffraction

Poor crystallinity of the two films are expected since they were just annealed at 800^{o}C for 1 min. X-ray diffraction of the two films were obtained as shown in Figure 4-17. Compared with the peaks from Zn_2GeO_4:Mn the target, the two films don't show any

new peaks after annealing. All the peaks from these two films are those from background glass/ITO/ATO. To be specific, the peaks are only from polycrystalline ITO layer and no peaks are possibly from either amorphous glass or amorphous ATO.

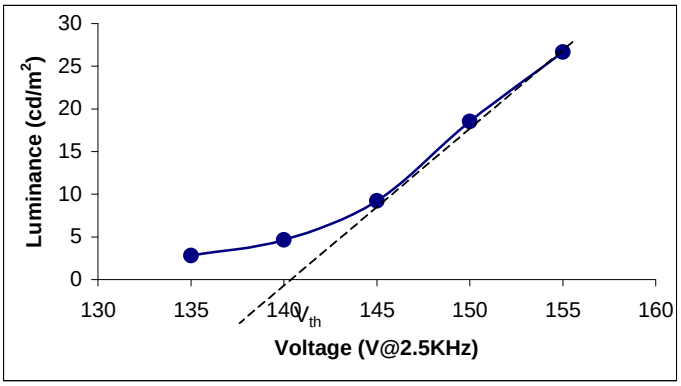

Figure 4-17 Brightness vs. voltage curve of glass/ITO/ATO/Zn_2GeO_4:Mn/Al ACTFEL devices using pulsed laser deposition. The Zn_2GeO_4:Mn film was deposited at 0.8J/cm^2, R.T. and annealed at 800^{o}C in Ar for 1min (NRL-ATO-1)

Compared the peak intensity of the two films with those of the glass/ITO/ATO, the peak intensity from the glass/ITO/ATO in the film deposited at 1.6J/cm^2 is much weaker than that in the film deposited at 0.8J/cm^2, which implies that the former film is much thicker since the thicker top layers the weaker x-ray can be detected from the underlying layer ITO. This supports again that the film deposited at 1.6cm^2 is much thicker than that deposited at 0.8J/cm^2. Since there is not direct thickness measurement for the two films, the thickness of the two films is estimated by different ways.

4.2.6.4 SEM

The surface morphology of the two films are the same and features as shown in Figure 4-19. However, the one deposited at 0.8J/cm^2 appears to have a larger crystallite grain size if it still can be called as crystallite size.

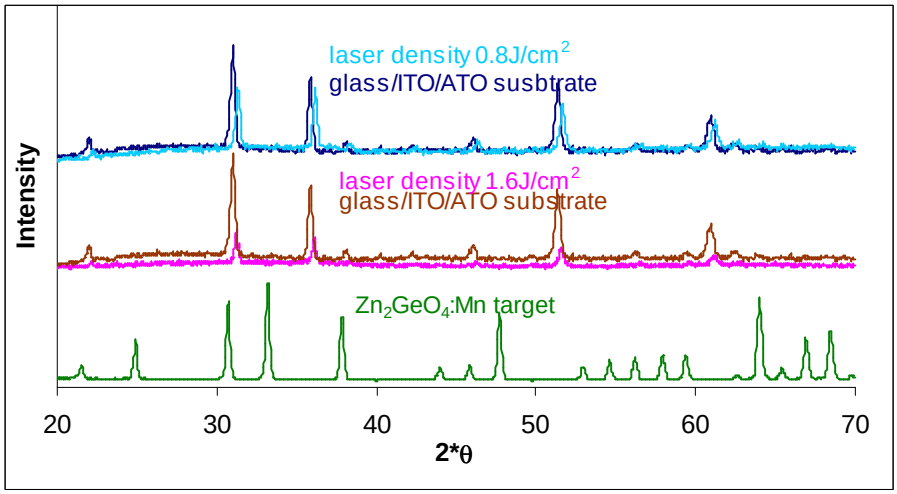

Figure 4-18 X-ray Diffraction pattern of pulsed laser deposited Zn_2GeO_4:Mn on glass/ITO/ATO. The two films were deposited at 250^{o}C and at 0.8J/cm^2 (NRL-ATO-1) and 1.6J/cm^2 (NRL-ATO-2) respectively. They were both annealed at 800^{o}C for 1min.

4.2.7 Zn_2GeO_4:Mn on PZT – Annealing Issue

The films were deposited on PZT substrate at two different ambient O_2 pressures: 150 mT(NRL-PZT-2) and 200 mT (NRL-PZT-1). Other deposition parameters were the same: laser density 0.8J/cm^2, substrate temperature 250^{o}C, laser pulses 10,000(laser repetition(shots/s) x deposition time (s)). After deposited at Ts = 250oC, they were annealed at 750^{o}C for 2.5hrs and 800^{o}C for 10 min.

4.2.7.1 Annealing Temperature vs. Time

The film deposited at 200mT and 150mT was annealed in box furnace in air at750^{o}C for 4 hrs or at 800^{o}C for 1.5 hrs respectively. The effect of O_2 pressure variation between 150 and 200 mTorr have been reported to be negligible.[50] Here it's more focused on the possible influence of post annealing on the two films. The temperature vs. time curve at two different temperature settings 700^{o}C and 800^{o}C was measured and is shown in Figure 4-20.

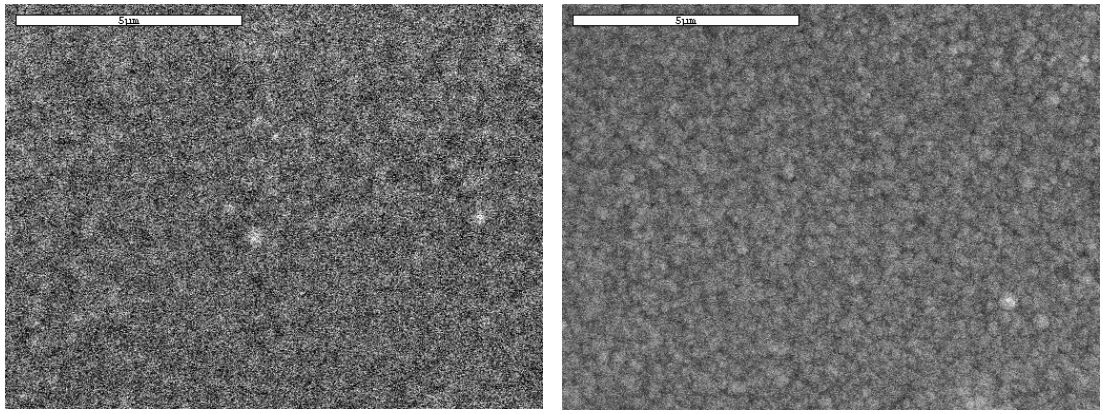

Figure 4-19 SEM image of pulsed laser deposited Zn_2GeO_4:Mn on glass/ITO/ATO. The films were deposited at laser density 1.6J/cm^2 (NRL-ATO-2) and 0.8J/cm^2 (NRL-ATO-1) respectively. Both of them were annealed at 800^{o}C for 1 min.

As shown in Figure 4-20, it takes about 90 min. (1.5hr) to reach 700^{o}C when the temperature is initially set at 700^{o}C, and it takes 100 minutes (1hr 40min) to reach 800^{o}C when the temperature is initially set at 800^{o}C. This implies that the film annealed at 800^{o}C for 1.5hrs barely stayed at 800^{o}C for any minute. After considered the furnace ramping rate, the 750^{o}C 4hrs. annealing should be 750^{o}C for 2.5hrs and the 800^{o}C 1.5hrs. annealing should be 770^{o}C for 10min.

4.2.7.2 Photoluminescence

Photoluminescence was measured for the two films under excitation of UV lamp at major wavelength 254nm. The PL spectra for the two films are shown in Figure 4-21. The photoluminescence spectrum of the UV lamp was obtained by collecting its reflection light from a $BaSO_4$ reflection standard.

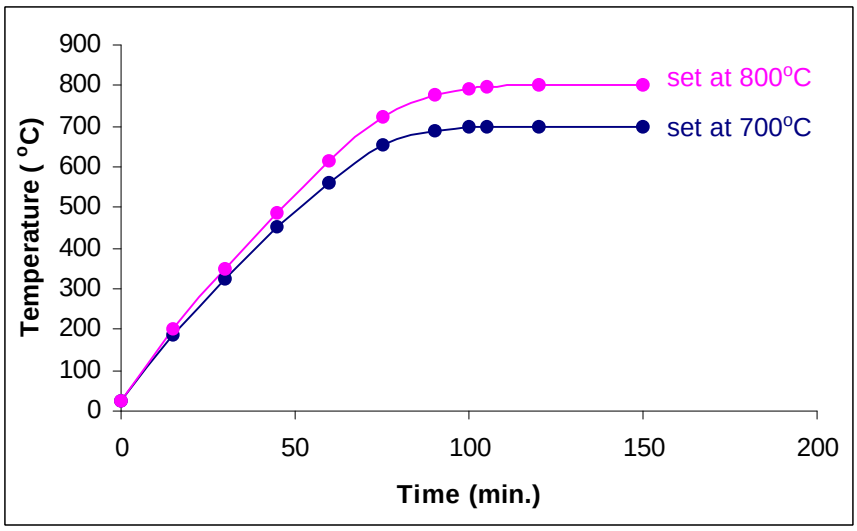

Figure 4-20 Temperature vs. time curve for box furnace at setting 700°C and 800°C

The film annealed at 750°C for 2.5hrs. shows a much larger PL intensity than that annealed at 770°C for 10min.. The temperature difference 20°C is not the primary reason to make PL intensity difference since the film annealed at 770°C was actually annealed for 10 min. due to the furnace slow ramping up rate. It has been explained above that the box furnace was not able to reach 800°C within 1.5hrs. Therefore, annealing time difference might be the primary reason to make PL intensity difference even if the deposition ambient O_2 pressure is slightly different. The UV lamp source was placed at an angle 45° to the film plane. The detecting spectrometer was placed normal to the film

plane. As described in Section 3.6.1.2., the detecting direction was intentionally placed away from the reflection angle. However, the reflection from the UV lamp light source is still strong as shown in Figure 4-21. Therefore, strictly speaking, the PL intensity of the films is contributed from the UV lamp source too. Before the PL intensity of the two films are compared, the UV lamp background spectrum should be extracted.

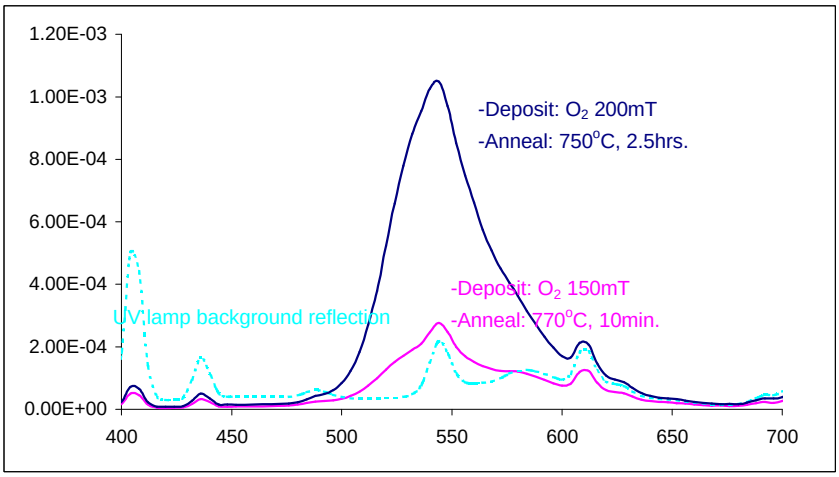

Figure 4-21 Photoluminescence emission spectrum of pulsed laser deposited Zn_2GeO_4:Mn on PZT annealed at 1)750°C 2.5hrs. (NRL-PZT-1) and at 2)770°C for 10min (NRL-PZT-2)

4.2.7.3 Electroluminescence

The dielectric layer used for the Zn_2GeO_4:Mn ACTFEL device was 20μm $Pb(Zr_{0.5}Ti_{0.5})O_3$(PZT). The whole EL device structure was the inverted structure with the multi-layer sequence Al_2O_3 substrate/Au/PZT/Zn_2GeO_4:Mn/ITO. This is not a full-cell EL structure since no top dielectric layer is used. It's a half-cell structure and its brightness should be approximately half of the full cell structure.[12]

The EL emission spectrum shown in Figure 4-22 is from the 750°C annealed film. One way to evaluate the uniformity of Mn^{2+} doping in the host Zn_2GeO_4 is to examine

whether the EL emission peak shifts with increase of the voltage.[1] As shown Figure 4-22, the emission spectra at all the voltage values from 150V to 230V give a broad peak at 536nm and no peak wavelength shift is observed. This implies that Mn^{2+} has been incorporated into the Zn_2GeO_4 host uniformly.

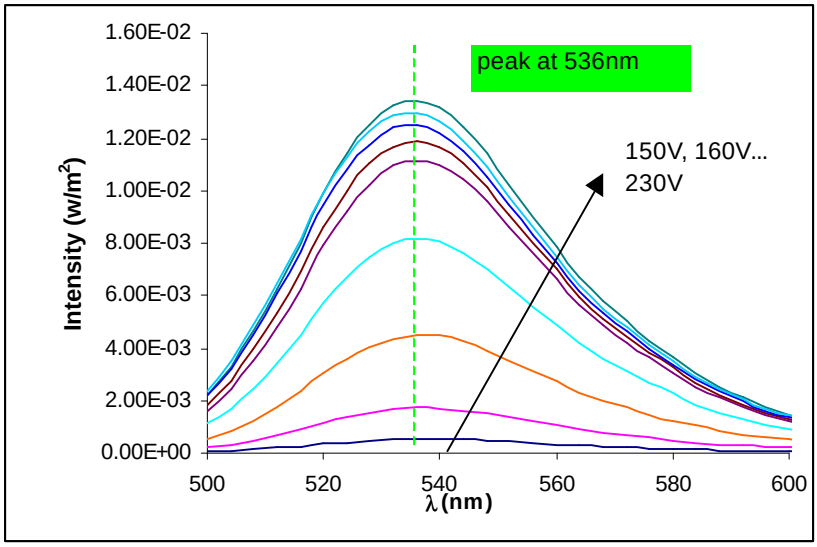

Figure 4-22 EL emission spectrum at each of the voltages applied for pulsed laser deposited Zn_2GeO_4:Mn on PZT substrate. This film was deposited at laser density 0.8J/cm^2 and O_2 pressure 200mT and annealed at 750^{o}C for 2.5hrs (NRL-PZT-1)

The electroluminescence of the two films is shown in Figure 4-23. The EL brightness of the film annealed at 750^{o}C for 2.5hrs (400cd/cm^2) is much higher than that annealed at 770^{o}C for 10min (40cd/cm^2, B_{40}, at 40V above threshold B_{40}). The B-V slope for the 750^{o}C annealed film is also much sharper than that for the 770^{o}C annealed film. This implies that the former one turned on quicker than the latter one. The threshold voltage for both is the same at 160V. This implies that their thickness is the same since the threshold voltage is dependent on the phosphor layer thickness and it is generally proportional to the thickness.[12]

4.2.7.4 X-ray Diffraction

As-deposited films on PZT are amorphous, even if they were deposited at substrate temperature 250°C. X-ray diffraction from amorphous films is not shown in Figure 4-24. The films are expected to re-crystallize upon annealing.

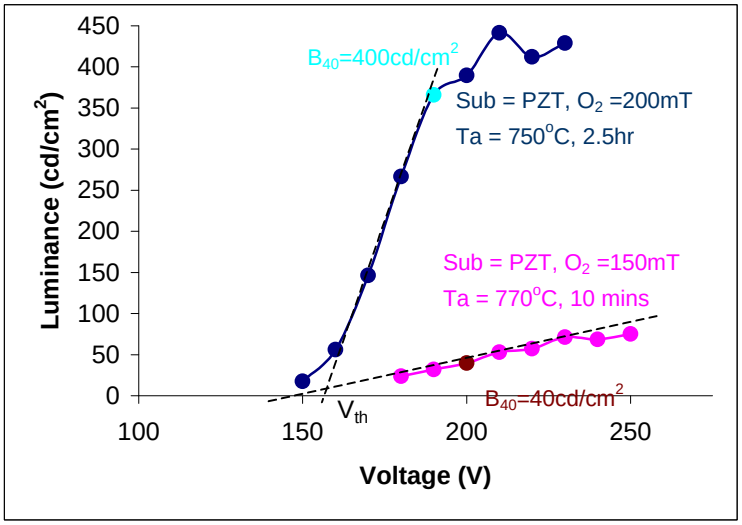

Figure 4-23 Electroluminescent brightness vs. voltage of Al_2O_3/Au/PZT/Zn_2GeO_4:Mn/ITO devices respectively 1)annealed at 750°C for 2.5hrs. (NRL-PZT-1) and 2) annealed at 770°C for 10min. (NRL-PZT-2)

XRD pattern from films annealed at 750°C 2.5hrs and 770°C for 10min. are shown in Figure 4-24 along with the spectra from the polycrystalline PZT background and Zn_2GeO_4:Mn target. The X-ray diffraction pattern of the Zn_2GeO_4:Mn target and the PZT substrate is also plotted here to compare. The film annealed at 750°C for 2.5 hours is definitely much better re-crystallized that that annealed at 770°C for 10 mins since the intensity of the peaks from the former one is much stronger than that from the latter one. Not all the new peaks upon annealing match the peaks of the target. The possible reaction of Zn_2GeO_4:Mn with PZT at high temperature will be discussed in Chapter 5. The peaks from the PZT substrate are much stronger upon annealing at 750°C for 2.5 hours. This

gives a sign that the PZT has been re-crystallized too upon the annealing. However, some of the increased PZT peaks overlapped with the peaks of the Zn_2GeO_4:Mn target such as the peak at 31°, 38°, 54°, 66°. The PZT peak at 57° is much stronger after annealing. Seven peaks other than those peaks from PZT appear upon annealing, located at 25°, 34°, 53°, 57°, 61°, 65°, and 67°. None of them match very well the peaks of the Zn_2GeO_4:Mn rohmbehedral target. The one at 34° and 61° even don't match either the peaks from PZT or those of the target. The film annealed at 770°C for 10mins doesn't demonstrate strong new peaks which implies that it was not well re-crystallized during the10min annealing time.

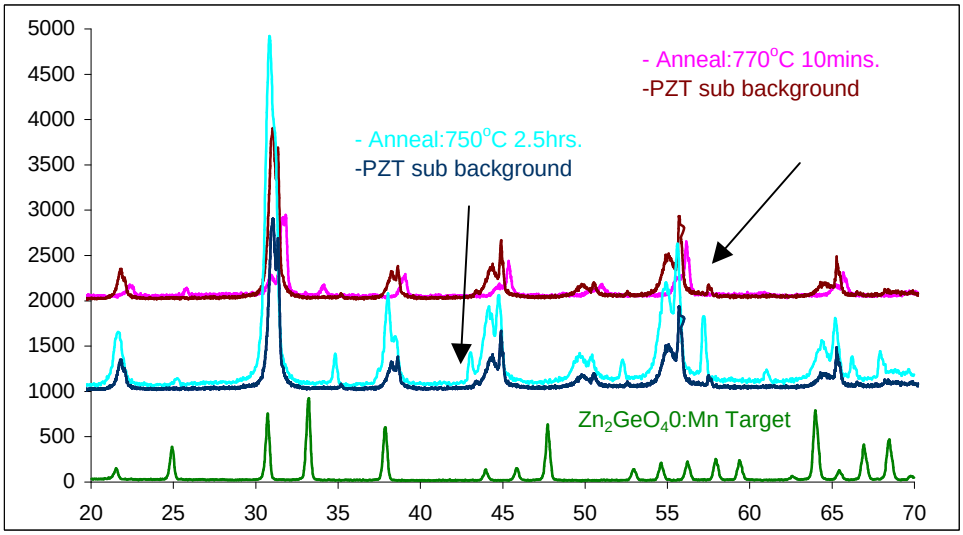

Figure 4-24 X-ray diffraction pattern of pulsed laser deposited Zn_2GeO_4:Mn on Al_2O_3/Au/PZT substrate annealed 1) at 750°C for 2.5hrs (NRL-PZT-1) and 2) at 770°C for 10 min. (NRL-PZT-2)

4.2.7.5 SEM

SEM plain view images were obtained for the two films as shown in Figure 4-25. Obviously, the film annealed at 750°C for 2.5hrs demonstrates a much larger grain size,

compared with that annealed at 800^{o}C for 1.5hrs. Re-crystallization upon annealing generally resulted in a rougher film surface, which might help PL and EL intensity due to the enhanced light out-coupling.

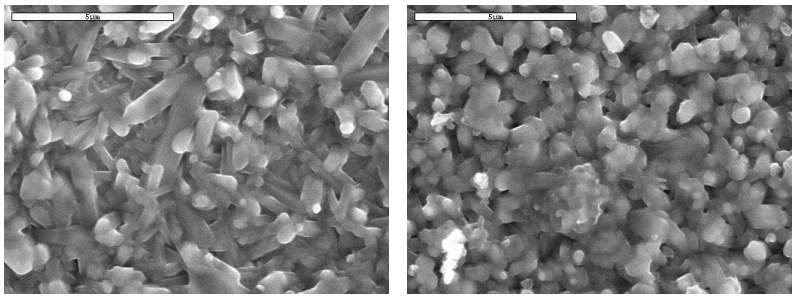

a) b)

Figure 4-25 SEM image of pulsed laser deposited Zn_2GeO_4:Mn on PZT, annealed a) at 750^{o}C for 2.5 hrs. (NRL-PZT-1) and b) at 770^{o}C for 10min (NRL-PZT-2)

4.2.7.6 Charge vs. Voltage Curve

The electric field formed inside the phosphor layer is proportional to the voltage dropped across the phosphor layer and as described in Section 2.3.3., the field across the phosphor increased as the dielectric constant of the dielectric layer is increased (ε = 300~1500 for PZT, compared to 15 for ATO) . The dynamic capacitance represents how fast the charge changes with the voltage as described in Section 3.6.1.4.. The C-V curve for the two films were measured as described in Section 3.6.1.4.. The measurement and the data processing of Q-V curve and C-V curve is referred to Sec. The Q-V curve for the film annealed at 750^{o}C for 2.5hrs. at each of the maximum voltage values is plotted in Figure 4-26. Each of the Q-V curves measured at different maximum voltages (150V, 190V and 230V) corresponds each of the brightness points on the B-V curve. As

expected, the area of the QV loop increases with the maximum voltage applied. The area of the QV is the input power to the device. The slope of the Q-V curve before the phosphor layer breaks down is the capacitance from both the phosphor layer and the dielectric layer, which is C_iC_p/C_i+C_p. C_i represents the capacitance of the dielectric layer and C_p the capacitance of the phosphor layer. After the phosphor layer breaks down, light is emitted from the phosphor layer and the capacitance now is only from the dielectric layer, which is C_i. Figure 4-26 shows that at voltages over 190V, all the charge is neutralized before the next waveform cycle comes. For V_{max} = 150V, some charge remains trapped in the matrix after electrical breakdown.

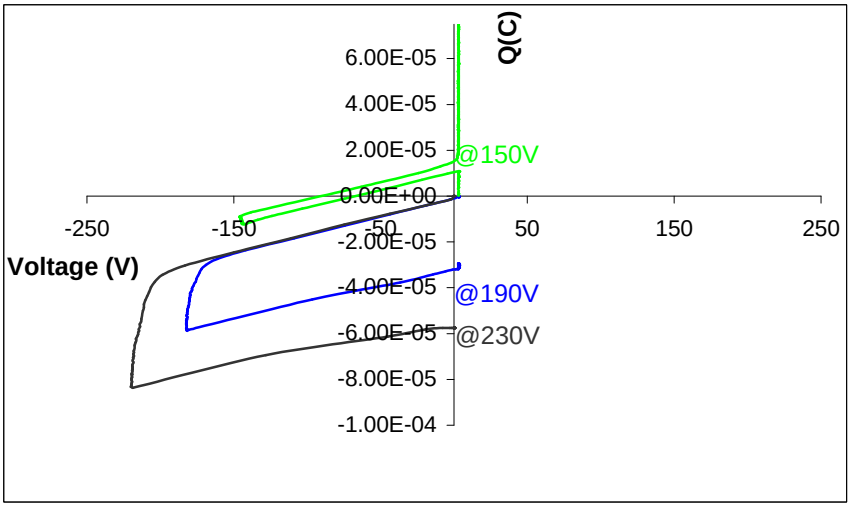

Figure 4-26 Charge (coulomb) vs. voltage (V) curve for pulsed laser deposited Zn_2GeO_4:Mn at maximum voltage 1)150V, 2) 190V and 3) 230V. This film was annealed at 750^{o}C for 2.5hrs (NRL-PZT-1)

The Q-V curve of the two films at voltage 230V is plotted in Figure 4-27. The charge in the film annealed at 750^{o}C for 2.5 hr accumulates much faster when the threshold voltage is reached, than that annealed at 770^{o}C for 10min, which implies that the electron ionization and multiplication occurs in a much more effective way in the 750^{o}C 2.5hr

anneal film. The luminous efficiency is defined as the brightness over the QV loop area. Q-V area for the two films are almost the same. But brightness is substantially lower by a factor of 10 for the 770^{o}C 10min anneal film. for the two films as presented above is substantially different at a factor of 10. The luminous efficiency for the 750^{o}C 2.5hr annealed film is much higher than that for the 770^{o}C 10 min annealed film.

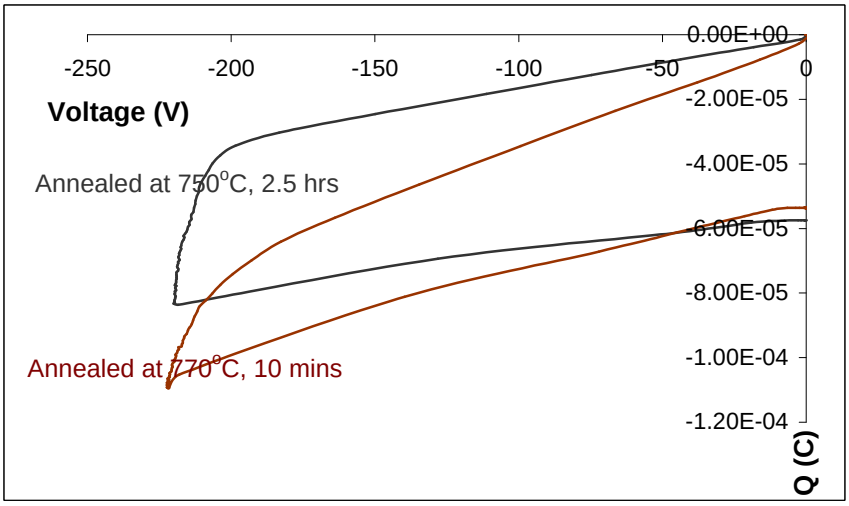

Figure 4-27 Q-V curves for pulsed laser deposited Zn_2GeO_4:Mn ACTFEL devices at maximum voltage 230V. The films were annealed respectively 1) at 750^{o}C for 2.5 hrs. (NRL-PZT-1) and 2) at 770^{o}C for 10mins (NRL-PZT-2)

4.2.7.7 Capacitance vs. Voltage Curve

The charge increase with the voltage can be better expressed in capacitance vs. voltage (C-V) data in which C is equal to dQ/dV. The C-V curves for these two films are plotted in Figure 4-28. The curvature of the C-V for the film annealed at 770^{o}C for 10mins indicates that the electric field not uniform within the phosphor. Instead it bends over the phosphor thickness.[46] Electric field bending is believed to be associated with charge trapped by defects in the film [46]. Electric field bending is not observed in the film

annealed at 750°C for 2.5hrs, which further supports that the crystallinity of the film annealed at 750°C for 2.5hrs is better than that annealed at 770°C for 10mins.

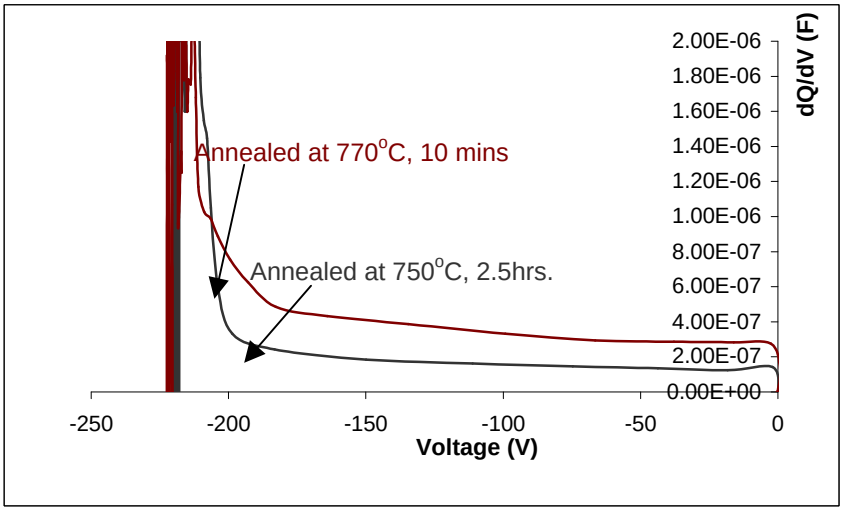

Figure 4-28 C-V curve of pulsed laser deposited Zn_2GeO_4:Mn ACTFELL devices at maximum voltage of 230V. The two films were annealed 1) at 750°C for 2.5hrs. (NRL-PZT-1) and 2) at 770°C for 10mins (NRL-PZT-2)

4.2.8 Zn_2GeO_4:Mn on PZT – Substrate Temperature Issue

Two Zn_2GeO_4:Mn films were deposited on PZT by pulsed laser deposition at room temperature (Sample NRL-PZT-3) and 800°C (Sample NRL-PZT-4) with other deposition parameters remaining the same. Film deposited at room temperature was 6800Å and the thickness for the one deposited at 800°C was 2800Å. The substrate temperature reduced the deposition rate dramatically. The film deposited at room temperature was annealed at 750°C for 4hrs to re-crystallize Zn_2GeO_4:Mn.

4.2.8.1 Photoluminescence

The photoluminescence results for the two films are shown in Figure 2-29. No photoluminescence was seen in the film deposited at R.T. even if it was annealed at 750°C. The L-V curve of the film deposited at 250°C and annealed at 750°C is also plotted together for comparison. The film deposited at 250°C and then annealed at 750°C demonstrates a much higher PL than the film deposited at 800°C. The PL peak for all the films appears at 540nm.

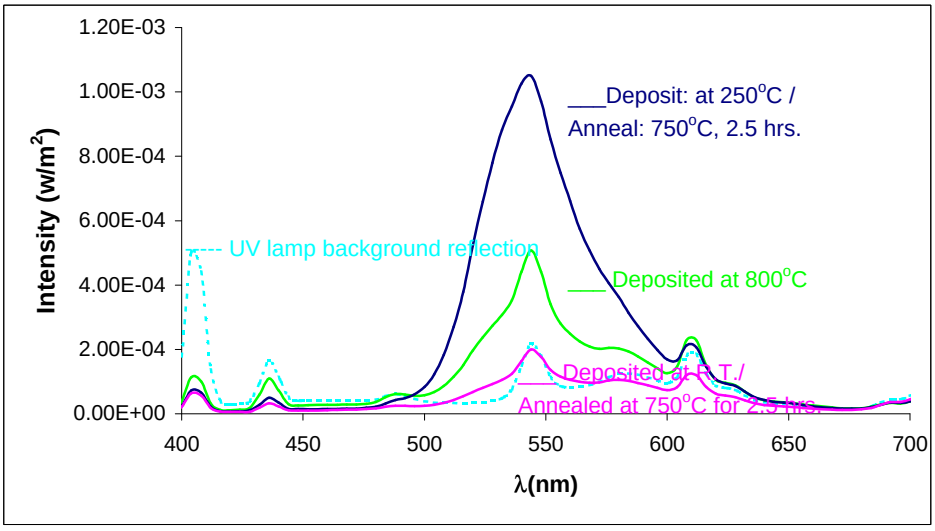

Figure 4-29 Photoluminescence spectrum of Zn_2GeO_4:Mn deposited on PZT at substrate temperature 1)R.T. (NRL-PZT3), 2) 250°C (NRL-PZT-1) and 3) 800°C (NRL-PZT-4). The films deposited at R.T. and 250°C were annealed at 750°C for 4hrs.

4.2.8.2 Electroluminescence (Luminance vs. Voltage)

The electroluminescence of the above two films were measured. The one deposited at room temperature and then annealed at 750°C didn't show any electroluminescence. The film deposited at 800°C showed EL luminance 84cd/cm^2 at the voltage 40V above the threshold voltage 110V. The film deposited at 250°C and then

annealed at 750°C is plotted together for comparison. The latter one demonstrates a much higher EL luminance and sharper turn on slope.

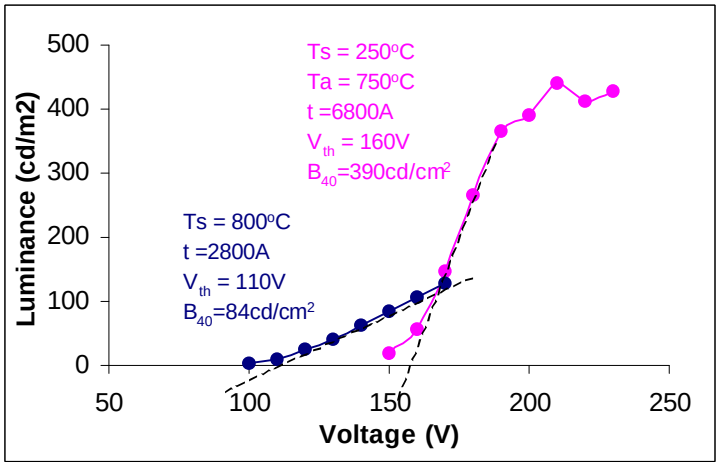

Figure 4-30 Electroluminescence L-V curve for the film deposited at 250°C and then annealed at 750°C for 2.5hrs. (NRL-PZT-1) and 2) the film deposited at 800°C(NRL-PZT-4).

4.2.8.3 X-ray Diffraction

X-ray diffraction patterns from the Zn_2GeO_4:Mn films deposited at R.T., 250°C and 800°C were obtained as shown in Figure 4-31. For the film Zn_2GeO_4:Mn deposited at RT, no new peaks appear after annealing at 750°C for 2.5hrs and the PZT peaks in this film became slightly larger after annealing. The observation that no new peaks appear implies that the 750°C 4hr annealing didn't re-crystallize RT deposited films fo Zn_2GeO_4:Mn . For the film deposited at 250°C, many new peaks appear after annealing at 750°C for 4hrs and their intensity is strong. To determine whether these new peaks are from Zn_2GeO_4 re-crystallization or from PZT re-crystallization is difficult since some of the peaks for both PZT and Zn_2GeO_4 are located at the same 2θ. The film deposited at 800°C demonstrated many new peaks compared with the x-ray diffraction pattern of the PZT substrate and these peaks' intensities are substantially strong. Some of these new

peaks are obviously Zn_2GeO_4 rhombahedral structure, by comparison with the rhombohedral Zn_2GeO_4:Mn target peaks. Some of these new peaks do not match either PZT or Zn_2GeO_4 rhombohedral peaks.

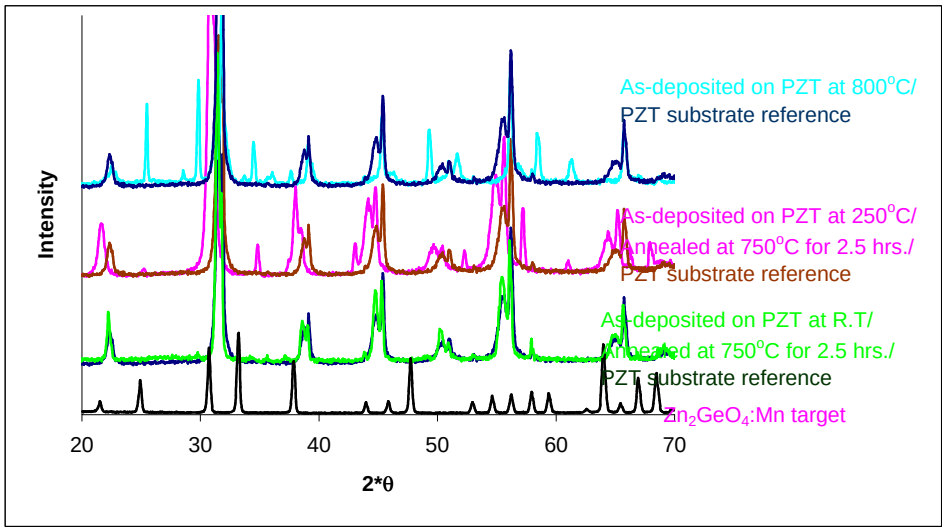

Figure 4-31 X-ray diffraction of pulsed laser deposited Zn_2GeO_4:Mn on PZT substrate at substrate temperature 1) R.T.(NRL-PZT-3) , 2)250°C (NRL-PZT-1) and 3) 800°C (NRL-PZT-4). The films deposited at R.T. and 250°C were annealed at 750°C for 2.5hrs.

4.3 Summary and Discussions

4.3.1 Zn_2GeO_4:Mn Target

The x-ray diffraction pattern of the Zn_2GeO_4:Mn target (Figure 4-1) shows that the Zn_2GeO_4:Mn target is well crystallized and it is in the Zn_2GeO_4 rhombohedral crystal structure. However, the shift of some of the peaks especially, of those at high 2θ might indicate that the Zn_2GeO_4:Mn target consists two similar rhombohedral structures, but at different lattice constant. When the lattice constants (a, b and c) are changed, the peak position is changed according to the equation 3-11 and equation 3-12. Four x-ray

diffraction pattern references are available for Zn_2GeO_4 crystal structures. They are cubic (a =5.937Å), tetragonal (a = 5.937Å, c = 8.254Å), rhombohedral I (a = 14.231Å, c = 9.530Å) and rhombohedral II (a = 14.22Å, c =9.49Å). The Zn_2GeO_4 rhombohedral I is slightly smaller in *c* than the Zn_2GeO_4 rhombohedral II. The reference rhombohedral shown in Figure 4-1 is rhombohedral I which has a slightly larger *a* and *c*.

The PL emission peak of the Zn_2GeO_4:Mn target was observed at 540nm and the PL excitation peak was observed at 340nm (Figure 4-2). The photon energy at 340nm is 3.7eV and the photon energy at 540nm is 2.3eV according to the equation $\boldsymbol{l}(nm) = \frac{1240}{E(eV)}$.

According to the emission and excitation energy, the Mn^{2+} transition in Zn_2GeO_4 can be expressed as shown in the following energy level diagram (Figure 4-32),

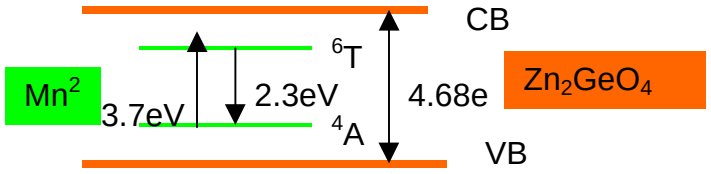

Figure 4-32 Optical transition of luminescent center Mn^{2+} in Zn_2GeO_4 host

For photoluminescence of Zn_2GeO_4:Mn, luminescent center Mn^{2+} is excited from the ground state ^4A by a photon from light source. The excitation energy for Mn^{2+} in Zn_2GeO_4 is 3.7eV, while the emission energy is 2.3eV. This implies that Mn^{2+} relaxation is two levels. In first level, the excited Mn^{2+} relaxes at the energy difference 3.7eV and 2.3eV, which is 1.4eV (885nm). This relaxation might be from irradiative emission. Even if it is radiative emission, it can't be seen in the emission spectra which only covers from wavelength 325nm to 800nm. In second level, the 2.7eV (540nm) relaxation should occur

since a broad large peak is seen at 540nm in the emission spectra. Since the bandgap of the host Zn_2GeO_4:Mn is 4.68 eV (265 nm),[46] the excitation wavelength 340 nm can't be from the band-to band excitation of Zn_2GeO_4. Because the atoms (ions) surrounding Mn^{2+} are changed, the emission wavelength of Mn^{2+} is change. For the case of ZnS:Mn, Mn^{2+} is surrounded by S^{2-} ions, while for the case of Zn_2GeO_4:Mn, Mn^{2+} is surrounded by O^{2-} ions. The crystal field of Mn^{2+} can be modified by the host material due to its unshielded 3d electrons.[28] Mn^{2+} transition energy is larger when the crystal field strength is increased, which corresponds a shorter wavelength. The energy of the only allowed transition ^6T to ^4A in Mn^{2+} can be changed depending on what the host ions Mn^{2+} is surrounded by. The crystal field strength of Mn^{2+} is determined by its environment of including the closest atoms (ions) and their distance away from Mn^{2+} etc. It's worth to emphasize that the ^6T - ^4A transition is only allowed when Mn^{2+} is in symmetric octahedral position. No such transition is allowed when Mn^{2+} is in non-symmetric tetrahedral.[16] The evidence that only one broad peak at 540nm is seen in the Zn_2GeO_4:Mn emission spectrum indicates that 1) Mn^{4+} has been converted into Mn^{2+} during firing; 2) Mn^{2+} has replaced Zn^{2+} octahedral position rather than Zn^{2+} tetrahedral position. The original Mn^{2+} doping source was from MnO_2. There was a concern whether Mn^{4+} of MnO_2 was converted into Mn^{2+} in Zn_2GeO_4:Mn. If Mn^{4+} exists in Zn_2GeO_4:Mn, it should replace Ge^{4+} in term of its valence number. However, according to compatibility of the size and electronegativity, $Ge^{4+}$and Mn^{4+} is completely different. Therefore, the assumption that Mn^{4+} substitutes for Ge^{4+} is unlikely to be true. Another concern was whether Mn^{2+} replaced Zn^{2+} octahedral or tetrahedral. Zn_2GeO_4 is the reverse spinel structure.[82] If Zn_2GeO_4:Mn is the regular spinel structure it should look

like $(Zn_AZn_A)Ge_BO_4$ where A stands for the octahedral position and B stands for the tetrahedral position. This Zn_2GeO_4 reverse spinel structure is $Zn_B(Zn_AGe_A)O_4$ in which the octahedral positions are equally shared by Zn^{2+} and Ge^{4+} and the tetrahedral positions are all occupied by Zn^{2+}. The 540nm green emission indicated clearly that the Mn^{2+} transition occurs. Therefore, it must have replaced Zn^{2+} octahedral position rather than Zn^{2+} tetrahedral position because the symmetric octahedral position somehow release the forbidden ^6T-^4A transition in Mn^{2+} .[16]

4.3.2 PZT Substrate

The thickness of 20μm was identified by SEM image (Figure 4-4) for the screen printed PZT layer. The PZT layer surface is extremely rough due to the inherent characteristics of the screen printing technique. X-ray diffraction identified that the PZT layer was $Pb(Zr_{0.52}Ti_{0.48})O_3$ polycrystalline.

4.3.3 Photoluminescence and Electroluminescence of Zn_2GeO_4:Mn Films

Zn_2GeO_4:Mn films grown by pulsed laser deposition exhibited a as single broad photoluminescence and electroluminescence peak at 540nm. The Zn_2GeO_4:Mn ACTFEL devices fabricated using pulsed laser deposition was first achieved. The highest brightness on Al_2O_3/Au/ PZT was 425 cd/cm^2 and the highest brightness on glass/ITO/ATO was 28 cd/cm^2 at a drive frequency 2.5 kHz.

4.3.4 Zn_2GeO_4:Mn on Si – Substrate Temperature Issue

Zn_2GeO_4:Mn film deposited on Si were used especially for study of photoluminescence of Zn_2GeO_4:Mn. It was found that Zn_2GeO_4:Mn deposited at 250 ^oC,

following by an annealing at 800 ^{o}C demonstrated a much higher photoluminescence. Several hypotheses are brought up for the observation. The hypotheses are 1) The deposition rate might be reduced at substrate temperature 800^{o}C resulting in a reduced thickness for the fixed deposition time; 2) The annealing at 800^{o}C for 24hrs might enhance Zn_2GeO_4:Mn crystallinity dramatically, compared with the film as-deposited at 800^{o}C. 3) The annealing at 800^{o}C for 24hrs.might make the film surface rougher resulting in a better light coupling. 4) The Zn_2GeO_4:Mn film might be more Zn deficiency at substrate temperature 800^{o}C.

First, regarding the first hypothesis - thickness difference, no direct information is available about the thickness difference of the two films. The film deposited at 250^{o}C was 10,000 Å given by profilometry using a step formed during deposition. No thickness data was available for the film deposited at 800^{o}C. However, the film thickness deposited at substrate temperature R.T and 800^{o}C was provided by NRL. It is shown in Figure 4-33.

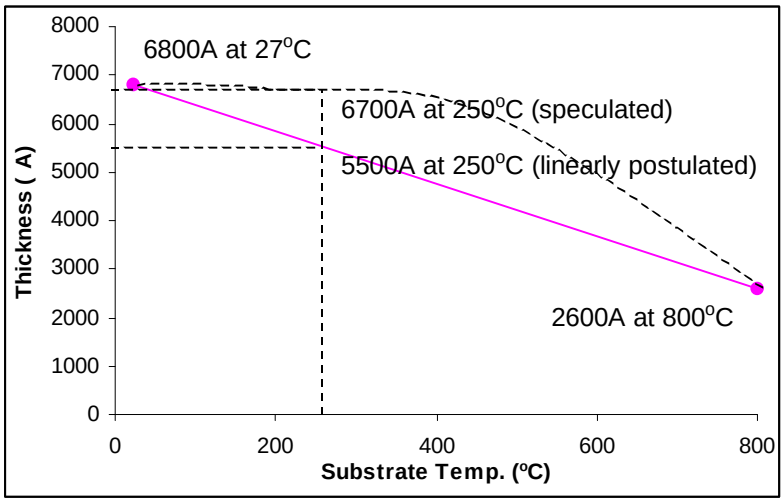

Figure 4-33 Thickness vs. substrate temperature curve for pulsed laser deposited Zn_2GeO_4:Mn

The film deposited at R.T. is 6800Å. Without changing any other parameters, the film deposited at 800^{o}C is reduced to 2600Å, which is only 2/5 of the thickness of the film deposited at R.T. Normally, the oxide deposition rate isn't changed much in the temperature range below 250^{o}C.[83] In this case, the deposition rate at 250^{o}C is assumed the same as that at R.T. Therefore, the film deposited at 800^{o}C is also only 2/5 of that deposited at 250^{o}C. Based on the thickness is 10,000Å when it is deposited at 250^{o}C. The film deposited at 800^{o}C should be 4000Å. It is obvious that the large thickness difference should contribute to the photoluminescence intensity difference. Whether it is an dominating factor is not confirmed yet. Crystallinity and surface roughness could influence photoluminescence intensity enormously as well.

Second, the crystallinity difference. According to the x-ray diffraction (Figure 4-9), both the films are rhombehedral Zn_2GeO_4:Mn structure and both were well crsytallized. The film deposited at 800^{o}C demonstrates a more textured structure than the film deposited at 250^{o}C. For a randomly distributed polycrystalline, all the possible peaks should appear. The film deposited at 800^{o}C demonstrates a strong peak at 34^{o} and other peaks are weak. The film deposited at 250^{o}C shows all the peaks and the intensity ratio of the peaks match well that of the peaks from the polycrystalline Zn_2GeO_4:Mn target powder. If we use the major peak at 34^{o} to do the crystallinity comparison, the film deposited at 800^{o}C has a better crystallinity. However, other peaks are relatively weak. On the average, the crystallinility for both films is the same. Therefore, crystallinity should not be responsible for the enhanced PL in this case.

The third assumption is the surface roughness. The SEM images for the two films (Figure 4-9) do show a much rougher surface for the film annealed at 800^{o}C. This is probably also responsible for the enhanced PL.

The fourth assumption is the Zn-deficiency. The EDX results (Figure 4-10) show that both of the films appear Zn-deficient, but the film deposited at 800^{o}C appears slightly more Zn-deficient. This difference could be from the substrate temperature difference or from the EDX analysis error. The EDX results for the films deposited at the same conditions but on different substrates (Figure 4-10) show that the Zn/Ge ratio difference (0.05) is the same as the Zn/Ge ratio difference (0.05) due to the substrate temperature difference. It is difficult to believe that the Zn_2GeO_4:Mn film deposited at 800^{o}C is more Zn deficient.

In general, the enhanced PL intensity for the film deposited at 250^{o}C, followed by an annealing at 800^{o}C for 24hrs is the result of the thickness difference and the surface roughness difference.

4.3.5 Zn_2GeO_4:Mn on PZT – Ambient O_2 Pressure Issue

Ambient O_2 was used for Zn_2GeO_4:Mn to restore O in Zn_2GeO_4:Mn. Higher ambient pressure tends to better block the ablated target particles before they drop on the substrate surface.[54] Two different ambient O_2 pressures 150 and 200 mTorr were used for the Zn_2GeO_4:Mn pulsed laser deposition. The ambient O_2 pressure change from over 200mTorr to down to 10mTorr would make a big difference in film microstructure, thickness, morphology etc [83] But, it is not the case for the 50mTorr difference from 200mTorr to 150mTorr.[83] The L-V curve for the two films (Figure 4-22) does show a big difference both in brightness and turn-on slope. However, it is believed that it is more

associated with annealing temperature and time difference rather than ambient gas pressure difference. The threshold voltages shown in the L-V curves for both films are the same. This implies that the thickness of the two films should be the same since the threshold voltage is strongly dependent on the phosphor layer thickness. This evidence is consistent with the assumption that the 50mTorr pressure difference wouldn't make any difference in film thickness etc.

4.3.6 Zn_2GeO_4:Mn on Glass/ITO/ATO – Laser Energy Density Issue

Higher laser density higher deposition rate is achieved. Generally, the deposition rate is proportional to the laser density.[49] Two different laser densities 0.8J/cm^2 and 1.6J/cm^2 were used for Zn_2GeO_4:Mn deposition on glass/ITO/ATO. The two films were annealed at 800^{o}C for 1 minute in Ar. Both the films demonstrated a photoluminescence peak at 540nm (Figure 4-16) under excitation of UV lamp. The photoluminescence intensity for the film deposited at 1.6J/cm^2 is higher than that for the film deposited at 0.8J/cm^2. This result is what was expected since the laser density increased the film thickness. The half-cell EL devices were formed by coating an Al dots on Zn_2GeO_4:Mn layer. Both the films demonstrated green electroluminescence. The film deposited at 1.6J/cm^2 burned immediately upon emitting EL light. No L-V curve was obtained for this film. The film deposited at 0.8J/cm^2 demonstrated the highest EL brightness 28cd/m^2 at the voltage 155V seen from the L-V curve (Figure 4-17). The voltage drive for this film was 2.5kHz. The reason that no electroluminescence was obtained from the film deposited 1.6J/cm^2 is probably because the interface between the Zn_2GeO_4:Mn and the Al layer was not clean enough and the Al was shorted instantly when the voltage is applied. This film had stayed in air for at least six months before it was coated with Al dots.

According to the x-ray diffraction patterns (Figure 4-18), both films are amorphous even if they were annealed. This is because the annealing time of 1 minute was too short for Zn_2GeO_4:Mn re-crystallization. The annealing temperature and time for Zn_2GeO_4:Mn deposited on glass/ITO/ATO was restricted by glass transition temperature (800^oC) and ITO degradation temperature (850^oC). The annealing recipe 800^oC for 1~2 minutes was the best we could use for films deposited on glass/ITO/ATO. According to the SEM images (Figure 4-19), the film deposited at $0.8J/cm^2$ shows a larger grain size than the film deposited at $1.6J/cm^2$. This implies that the higher laser density slightly reduced the grain size. The grain size of the two films was too small to be detected by x-ray diffraction. That is why no peaks were observed from the Zn_2GeO_4:Mn layer. The EDX analysis results (not presented in this dissertation) show that the 15kV electron penetrated into the underlying ATO layer. This implies that the two films were too thin and their thickness is estimated less than 1μm. The thickness for the two films were not able to be measured by profilometry since no step was made during the deposition for this thickness measurement.

4.3.7 Zn_2GeO_4:Mn on PZT – Annealing Issue

The films annealed at 750^oC for 2.5hrs demonstrated a much higher EL brightness and faster EL turn-on than the film annealed at 770^oC for 10 min.. There are several mechanisms leading this enhanced EL. They are 1) Long annealing time might result in a better crystallinity. 2) Longer annealing time might result in a rougher surface. 3) Longer annealing time might result in a higher luminous efficiency due to the defect reduction. Two annealing parameters could lead to a better crystallinity. They are temperature and

time. For this two films, it is difficult to compare since both the annealing temperature and time are different. However, because of the low ramping rate for the furnace (Figure 4-20), the film annealed at 800^{o}C for 1.5hrs practically was annealed at temperature less than 800^{o}C (770^{o}C) for 10 mins. In this case, the annealing time is a dominating factor of enhancing crystallinity. The film annealed at 750^{o}C at 2.5hrs. should be better crystallized than the film annealed at 770^{o}C for 10 min.. The x-ray diffraction patterns of the two films (Figure 4-24) confirm this assumption. The EDX surface images of the two films (4-25) shows that the grain size for the film annealed at 750^{o}C at 2.5hrs is larger than that annealed at 770^{o}C for 10 mins. This further confirms that the crystallinity for the film annealed at 750^{o}C for 2.5hrs is better and also implies that this film surface is rougher upon annealing for a longer annealing time. The Q-V curves for the two films show that the luminous efficiency for the film annealed at 750^{o}C for 2.5hrs.is 10 times higher. The C-V curve shows that the defects are probably responsible for the decreased EL brightness and efficiency in the film annealed at 770^{o}C for 10mins.

In summary, the enhanced EL brightness in the film annealed at 750^{o}C for 2.5hrs, compared with the film annealed at 770^{o}C for 10 mins, was the result of the longer annealing time rather than annealing temperature. This longer annealing time resulted in a better crystallinity, rougher surface and less defects, all of the factors that lead to higher brightness and higher efficiency.

4.3.8 Zn_2GeO_4:Mn on PZT – Substrate Temperature Issue

Zn_2GeO_4:Mn films were deposited at room temperature, 250^{o}C and 800^{o}C. The films deposited at room temperature and 250^{o}C were amorphous. Upon annealing at 750^{o}C for 4hrs, the re-crystallization and PL emission is expected. However, the film

deposited at room temperature doesn't show any PL even after it is annealed. The film deposited at 250^{o}C, then annealed at 750^{o}C demonstrated a even higher PL and EL than that deposited at 800^{o}C. Several reasons could contribute to the decreased brightness in the film deposited at 800^{o}C. First is the thickness difference. As explained above, the deposition rate at 800^{o}C is only 2/5 of that at 250^{o}C (Figure 4-33). Therefore, the thickness difference is the big reason for the brightness difference. The reaction of Zn_2GeO_4:Mn and PZT at 800^{o}C is another possible reason. The x-ray diffraction patterns of the three films deposited at room temperature, 250^{o}C and 800^{o}C show that more unknown new peaks appear for the film deposited at 800^{o}C, which are not either from PZT re-growth or from Zn_2GeO_4 re-crystallization. The reason that the EL brightness is decreased for the film deposited at 800^{o}C could be associated with the interface of Zn_2GeO_4:Mn and PZT. The Zn_2GeO_4:Mn layer grown at 800^{o}C is only 2800Å. This thickness could be even smaller than the PZT surface roughness. The interface charge and the charge transportation could be effected by this situation.

4.3.9 Comparison of Zn_2GeO_4:Mn Deposition on PZT and Glass/ITO/ATO

4.3.9.1 Electroluminescence (Luminance vs. Voltage)

Electroluminescence was obtained in pulsed laser deposited Zn_2GeO_4:Mn both on PZT and glass/ITO/ATO. The brightness in the film on PZT is much higher than that in the film on glass/ITO/ATO as shown in the Figure 4-34.

4.3.9.2 X-ray Diffraction

The first parameter needed to examine the enhanced EL brightness is the film crystallinity. The film deposited on PZT, which was annealed at 750°C for 2.5hrs is expected to demonstrate a much better crystallinity than that on glass/ITO/ATO, which was annealed at 800°C for 1min due to the big difference in annealing time.

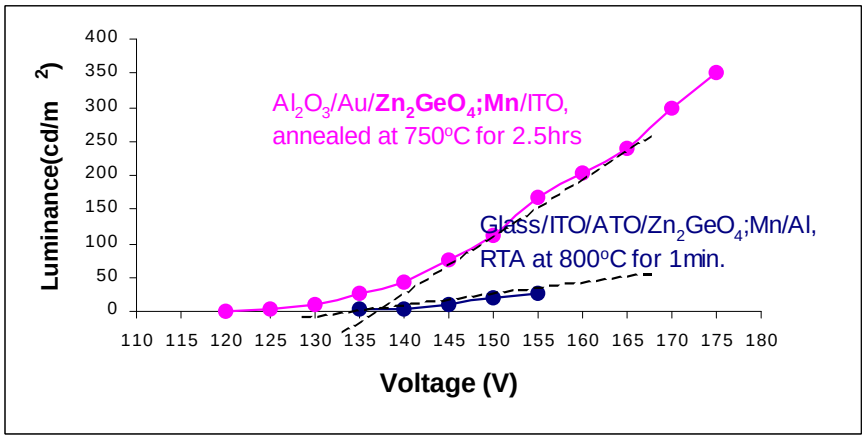

Figure 4-34 Electroluminescence luminance-voltage from Zn_2GeO_4:Mn film deposition on two different substrates PZT and glass/ITO/ATO

The x-ray diffraction of the two films is given in Figure 4-35. As shown in the figure, compared with the substrate peaks, new peaks appear in the film deposited at PZT upon annealing, which refers the film has been re-crystallized during annealing. While, the film deposited on glass/ITO/ATO doesn't show any new peaks upon annealing, which refers that the Zn_2GeO_4:Mn is not re-crystallized at all.

4.3.9.3 SEM

The SEM image of the two films can give a better view of the grain size. As shown in the images, the film on glass/ITO/ATO doesn't demonstrate any reasonably

large grain size. Therefore, the annealing time really makes a big difference in crystallinity of Zn_2GeO_4 layer.

4.3.9.4 Capacitance

Another difference for the two Zn_2GeO_4:Mn EL device is dielectric layer. The voltage drop across the phosphor layer is determined by capacitance of the phosphor and the dielectric, given by $V_{phosphor} = C_{dielectric}/(C_{dielectric}+C_{phosphor})V_{total}$ as discussed in the Section 2.3.3.

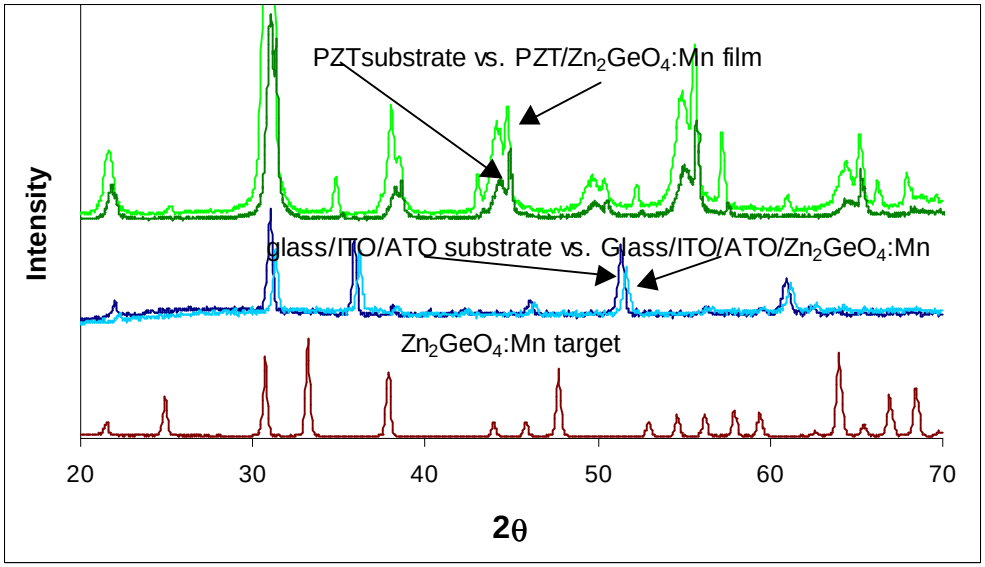

Figure 4-35 X-ray diffraction pattern of Zn_2GeO_4:Mn film deposited on two different substrates: 1) PZT(annealed at 750°C for 3hrs.) and 2) glass/ITO/ATO (annealed at 800°C for 1 min.)

The higher capacitance the dielectric layer is, the larger voltage drop cross the phosphor layer will be. The capacitance of dielectric layers by area is determined by dielectric constant and film thickness. It is proportional to dielectric constant and inversely proportional to film thickness. The PZT layer is 20μm and the ATO layer is only 2000Å. The thickness difference of the two dielectric layers is a factor of 100. Typically

dielectric constant of ATO is 7.5. The dielectric constant of PZT is unknown. It could be ranged from 100~1000. The capacitance of the two dielectric layers was obtained. The capacitance of the phosphor layer is difficult to be measured directly. However, it is convenient to measure the capacitance of the phosphor layer together with the dielectric layer. The capacitance of the phosphor can be deduced from the two capacitances according to the following equation:

$$\frac{1}{C_{phosphor}} = \frac{1}{C_{phosphor\,/\,dielectric}} - \frac{1}{C_{dielectric}}$$

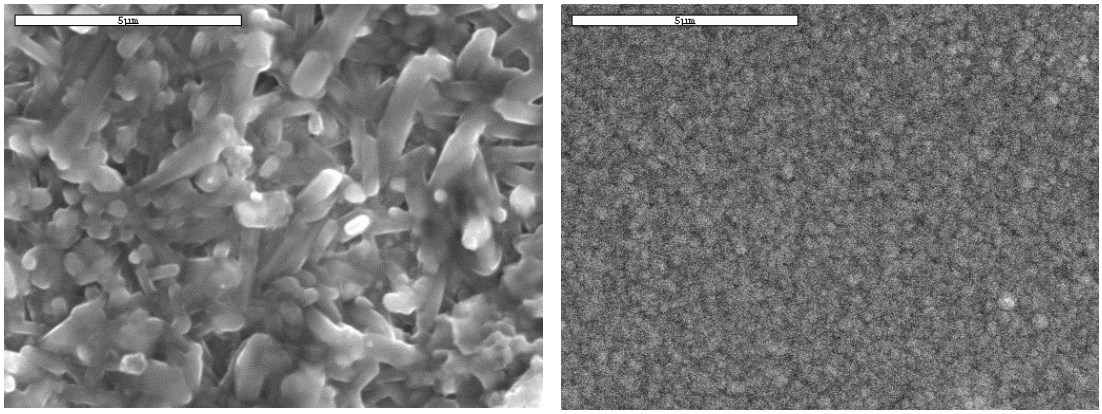

Figure 4-36 SEM image of Zn_2GeO_4:Mn film deposited on two different substrates: 1) PZT (annealed at 750^{o}C for 2.5hrs) and 2) glass/ITO/ATO (annealed at 800^{o}C for 1min.)

All the three capacitances for the two films are listed in Table 4-3,

Table 4-3 Capacitance of Zn_2GeO_4:Mn on glass/ITO/ATO and on PZT

Capacitance (nF/cm^2)	Phosphor + Dielectric	ATO	PZT	Phosphor	$C_{ph}/(C_{ph}+C_{dielectric})$
Zn_2GeO_4:Mn/ATO	10	61		12	0.84
Zn_2GeO_4:Mn/PZT	7		47	8	0.86

As shown in Table 4-3, the capacitance of the two different dielectric layers is different. But, the capacitance factor $C_{ph}/(C_{ph} + C_{dielectric})$ for the voltage drop through the phosphor layer is surprisingly almost the same, 0.84 and 0.86. Therefore, even if the two dielectric layer is different in dielectric constant and thickness, the voltage through the phosphor remains unchanged.

In the L-V curves, the Zn_2GeO_4:Mn on glass/ITO/ATO burned out at 155V, while the Zn_2GeO_4:Mn on PZT ddin't burn out even at the highest voltage 300V. Two mechanisms are responsible for the early burning in the film on glass/ITO/ATO: 1) dielectric layer breakdown; 2) the metal Al dot melting. The breakdown field E is determined by applied voltage and the dielectric layer thickness, given by E = V/t. The thickness difference of the two dielectric layers PZT and ATO is a factor of 100 as discussed above. The intrinsic breakdown strength for PZT and ATO is 150MV/mil and 300MV/mil. According to these data, a simply mathematics calculation can tell that the 20μm PZT can tolerate a much higher voltage than 2000Å ATO. Another burning mechanism is the Al melting. The Al melting point is 660^{o}C. The local temperature of the device could be much higher when a high frequency voltage like 2.5KHz is applied. At this point, the Al dots will be melt and burned out first.

4.3.9.5 Summary

In conclusion, the real reason that Zn_2GeO_4:Mn on PZT substrate demonstrated high EL and faster turn on than that on glass/ITO/ATO is that longer annealing time resulted in a better crystallization which enhances EL emission efficiency and the larger PZT thickness which withstands a higher voltage applied.

4.3.10 Zinc Deficiency of Zn_2GeO_4:Mn Films

The EDX results (Figure 4-12) show that the Zn/Ge ratio of the Zn_2GeO_4:Mn films grown by pulsed laser deposition was from 0.72~0.83 depending on substrate temperature applied. The Zn/Ge ratios are far lower than the stoichiometric Zn/Ge ratio 2.00 for Zn_2GeO_4. If the EDX results are accurate, the phases other than Zn_2GeO_4 and containing Ge oxides should be in the film, such as $ZnGeO_3$ or GeO_2 to make the overall Zn/Ge ratio less than 2.00. However, the x-ray diffraction of the films either deposited at 250^{o}C or 800^{o}C clearly indicate a Zn_2GeO_4 rhombohedral structure formed only. In this point, the accuracy of the EDX results is in doubt. The conclusion that the Zn_2GeO_4:Mn films are Zn-deficiency might be not true. The Zn/Ge ratio for the Zn_2GeO_4:Mn film deposited at 800^{o}C (0.73) is more Zn deficient than that for the film deposited at 250^{o}C (0.78). However, the EDX results for the films deposited at same temperature but different substrate show an EDX error of 0.05. In this point, the Zn/Ge ratio for the film deposited both at 250^{o}C and at 800^{o}C should be almost the same and therefore the Zn/Ge ratio is independent of substrate temperature.

CHAPTER 5
SPUTTER DEPOSITED Zn_2GeO_4:Mn

5.1 Parametrics of Zn_2GeO_4:Mn Sputtering Deposition

As mentioned in Section 2.6, Zn_2GeO_4:Mn ACTFEL devices have been investigated by Minami et al using sputtering deposition.[47] In his research, the Zn_2GeO_4:Mn was directly deposited on 0.2mm dielectric sheet $BaTiO_3$. The Zn_2GeO_4:Mn ACTFEL device was formed by depositing a transparent conducting layer of ZnO:Al on top of the Zn_2GeO_4:Mn layer and depositing a metal conducting layer Al on the backside of the $BaTiO_3$. Therefore the Zn_2GeO_4:Mn ACTFEL device structure sequence was a Al/$BaTiO_3$ substrate/Zn_2GeO_4:Mn/ZnO:Al and it was half-cell inverted EL device structure. In the currrent research, Zn_2GeO_4:Mn was sputter deposited on an Al_2O_3/Au/Pb(ZrTi)O_3 substrate, and this half-cell inverted structure was formed by depositing an ITO transparent conducting layer on top. This half-cell device structure was Al_2O_3 substrate/Au/Pb(ZrTi)O_3/ITO. The ceramic Al_2O_3 was used simply as substrate, therefore it was different from Minami's $BaTiO_3$ sheet which served as a substrate and a dielectric layer.

5.1.1 Deposition Repeatability

The deposition repeatability was investigated by comparing photoluminescence for films deposited in different runs with the same condition, or from different sample areas. The films were deposited at exactly same condition: base pressure: $5x10^{-6}$Torr, Ar:

70 sccm / O_2 30 sccm, working pressure: 15mTorr, power: 25W, substrate temperature: R.T., deposition time: 100 minutes and substrate: PZT. The thickness for the films was 4750Å which varied across the substrate by +/-10%. All the films were annealed at 700^{o}C in air for 2.5hrs. The films discussed in the following sections were all deposited with these conditions otherwise specified. The photoluminescence of the films is shown in Figure 5-1.

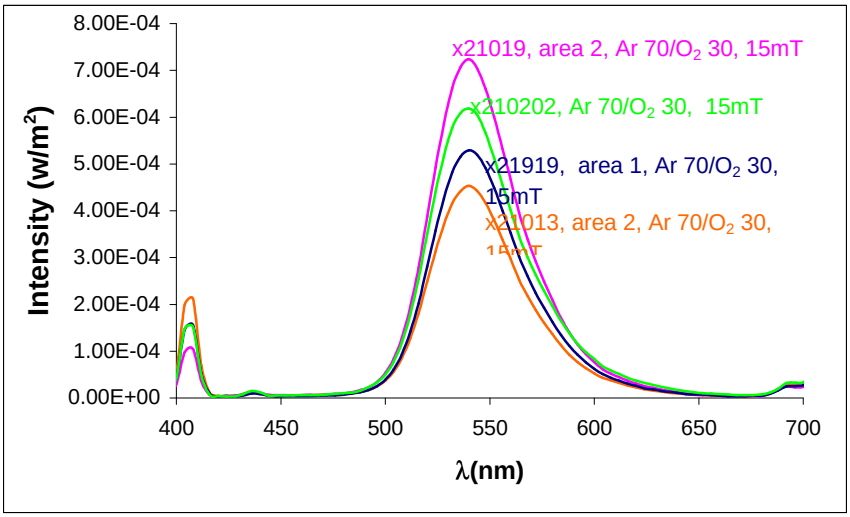

Figure 5-1 Photoluminescence spectrum of sputter deposited Zn_2GeO_4:Mn films on PZT at thickness 4750Å

Sample x21019 was a film deposited on 2”x2” PZT substrate and was cut into four 1”x 1” samples. The photoluminescence was measured at the center part of each of the four 1”x1” samples (marked as area 1 and area 2). Sample x21020 and x21013 were deposited on 1”x1” PZT substrate. Generally, The smaller substrate gives a better thickness uniformity. The largest photoluminescence change for all the films deposited at this condition is 2.69E-04 W/cm^2 (+/- 20%). The thickness variation (+/- 10%) might be the primary reason to make the photoluminescence intensity different. The PL measurement error might be also responsible for the PL difference.

5.1.2 Working Pressure

For sputtering, the deposition rate is strongly dependent on working pressure.[61] A maximum deposition rate is generally reached at a moderate working pressure. Pressures between 7.2 and 25 mTorr were investigated for Zn_2GeO_4:Mn deposition as shown in Figure 5-2, with other parameters held constant at the values described above and Chapter 3. The deposition rate was obtained by dividing film thickness by deposition time where thickness was measured by profilometry on a step. The deposition rate vs. working pressure curve is given in Figure 5-2.

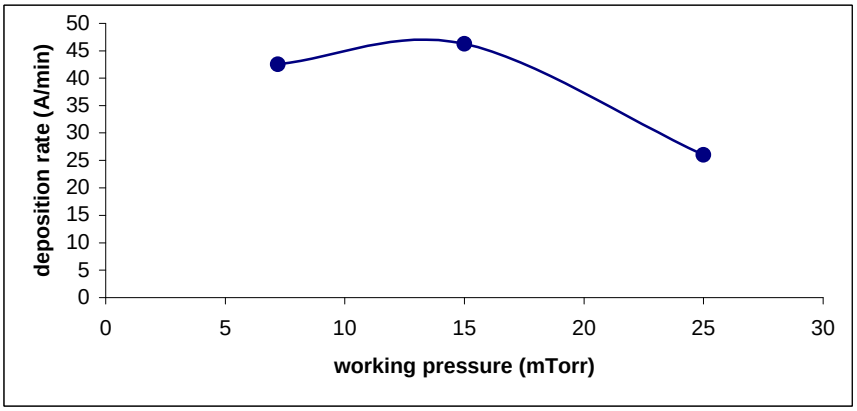

Figure 5-2 Deposition rate vs. working pressure for RF sputtering deposition of Zn_2GeO_4:Mn on PZT substrate

As shown in Figure 5-2, the deposition rate was lower at 7.2 and 25 mTorr than for 15 mTorr where the deposition rate was 48Å/min. The relationship of deposition rate to working pressure shown in Figure 5-2 is as expected. At low working pressure, the Ar partial pressure is low and the Ar ion density in the plasma is low, therefore the deposition rate is low. At high working pressure, the Ar density is high and there the probability of multiplication of Ar ions is higher resulting in a low deposition rate. High deposition rates are preferred to reduce deposition time which reduces incorporated

residual gas impurities. The highest deposition rate obtained in the system was 48Å/m at 15mT working pressure. At this deposition rate, 200 minutes would required to obtain a 1μm thick Zn_2GeO_4:Mn film.

Photoluminescence was measured by UV lamp for Zn_2GeO_4:Mn films deposited at conditions described for Figure 5-3. "sccm" is the unit for gas flow rate and it is "standard cubic center-meter /minute". To maintain a constant thickness of 5000Å, the deposition time was changed depending on the working pressure. A post deposition annealing at 700^{o}C for 2.5 hrs. in air was applied to the films.

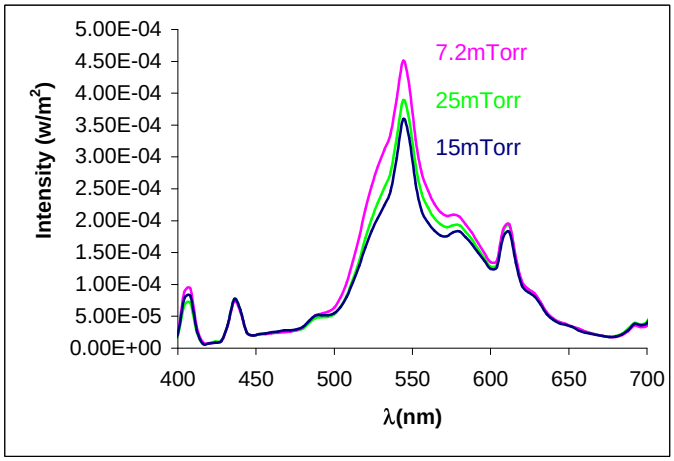

Figure 5-3 Photoluminescence spectra of sputter deposited Zn_2GeO_4:Mn on PZT substrate at three different working pressures: 1) 7.2mTorr, 2) 15mTorr and 3) 25mTorr

As shown in Figure 5-3, photoluminescent intensity varied +/-12% dependent upon deposition pressure being highest for 7.2mTorr and lowest for 15mTorr. This PL intensity variation is smaller than the photoluminescence variation +/- 20% associated with the deposition repeatability discussed above. Therefore, the photoluminescence of Zn_2GeO_4:Mn film on PZT is almost independent of the working pressure.

5.1.3 Ar /O_2 Ratio

Since Zn_2GeO_4:Mn is an oxide, introduction of O_2 during deposition was studied to evaluate its effects on Zn_2GeO_4:Mn film. The total flow rate was maintained constant, with Ar flow rate being increased as the oxygen rate was decreased. When an Ar atom is ionized into an ion Ar^+, an electron is removed from the Ar atom. Accelerated in a voltage potential, the electron possibly impacts another Ar atom to ionize it. This is called multiplication process and it is self-sustained eventually. This ionization and multiplication process can be illustrated as below,

$$Ar + \bar{e} \rightarrow Ar^+ + 2\bar{e}$$

The charged Ar^+ ions are accelerated under the voltage potential towards the target. O_2 molecules (atoms) could be ionized too. But, it's difficult to be ionized into O^+ due to its large electronegativity. Generally, O_2 doesn't contribute to the plasma. That means, maintained at a constant working pressure, the more O_2 is introduced the less Ar partial pressure is in chamber and the lower deposition rate is achieved. The films were deposited at various Ar/O_2 ratios. They were pure Ar, Ar 70 sccm /O_2 30 sccm, and Ar 50 sccm / O_2 50 sccm. Other deposition parameters remained the same. The deposition rate vs. Ar/O_2 ratio for Zn_2GeO_4:Mn shown in Figure 5-4 was 30Å/min at 50% Ar and increased to 48 and 65Å/min for 70 and 100% Ar. In our system, the Ar/O_2 was from two separate Ar and O_2 cylinders and they were independently controlled by flow mass controller to reach a certain Ar/O_2 ratio before they were mixed and introduced into the chamber. The partial pressure ratio is the same as the flow rate ratio in value. PL (Figure

5-5) was measured from films deposited with 50%, 70% and 100% Ar where the thickness was constant at 5000Å.

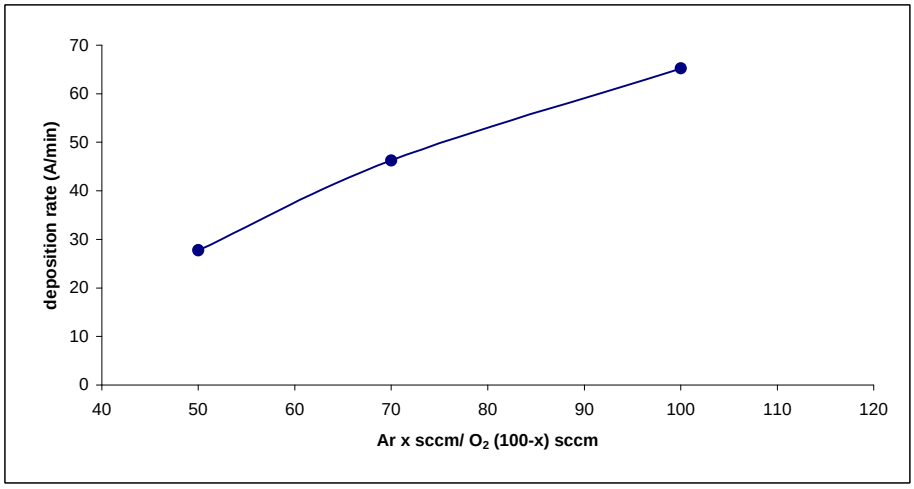

Figure 5-4 Deposition rate vs. Ar flow rate for Ar + O_2 mixtures during sputtering deposition of Zn_2GeO_4:Mn on PZT substrate. Total flow rate was 100 sccm for all depositions.

The film deposited in pure Ar gave the highest photoluminescent intensity (4.20E-04 W/cm^2) while Ar 50 sccm/O_2 50 sccm mixture gave the lowest (3.30E-04 W/cm^2). This represents a +/- 12% spread which is lower than the repeatability demonstrated in Section 5.1.2., therefore lower than experimental error, the photoluminescence intensity of Zn_2GeO_4:Mn film on PZT is independent on Ar/O_2 ambient pressure ratio.

5.1.4 Dependence of Photoluminescence on Film Thickness

Generally, the larger thickness the stronger photoluminescence intensity is since a larger number of luminescent centers contribute to the photoluminescence. Empirically, the PL intensity is proportional to the thickness, however, some layers are not contribute

to PL and are known as “dead layers”.[12] Therefore, the PL intensity *I* is given by the following equation:

$$I = K*(t - t_{DL}) \qquad (5\text{-}1)$$

where t_{DL} is the factor from the dead layer, K is proportional constant, t is the phosphor layer thickness. However, the UV lamp light source background also possibly contributes to the PL intensity. In this case, c which is the factor from light source is also introduced into this equation, and the modified photoluminescence intensity I is given by,

$$I = c + K*(t - t_{DL}) \qquad (5\text{-}2)$$

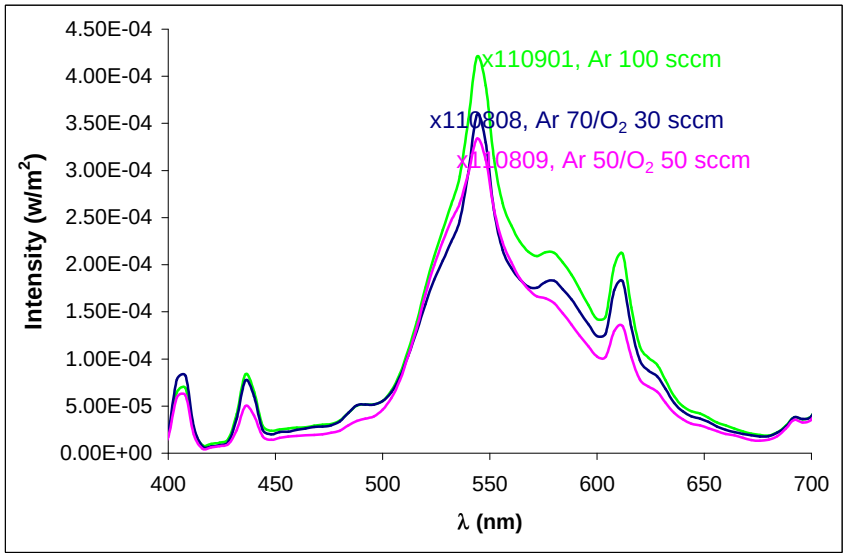

Figure 5-5 Photoluminescence spectra of sputter deposited Zn_2GeO_4:Mn films at three different Ar/O_2 ambient gas pressure ratios, 1) Ar 100sccm; 2) Ar 70 sccm/O_2 30sccm; and 3) Ar 50 sccm/O_2 50 sccm

The photoluminescent intensity and brightness vs. Zn_2GeO_4:Mn film thickness were obtained and are shown in Figure 5-6 in units of both W/cm^2 and with the photonic response of the eye to yield luminance in cd/m^2, respectively. The brightness versus

thickness is plotted in Figure 5-7, and based on the PL intensity vs. thickness curve, an empirical linear fitting function is deduced. The constant ($c-K*t_{DL}$) is obtained by extrapolating the linear trend line to the PL brightness axis. The constant K is the slope of the linear trend line. The fitting function is obtained eventually, expressed as,

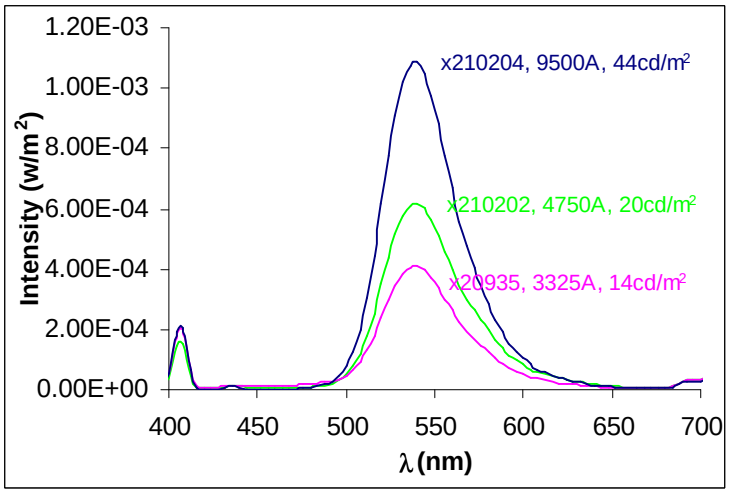

Figure 5-6 Photoluminescence spectra and brightness of sputter deposited Zn_2GeO_4:Mn at different thicknesses 1) 3325Å; 2) 4750Å; and 3)9500Å.

The above equation shows that even if the thickness goes down to zero, 3.5 cd/m^2 PL is seen. This refers that the PL gain from UV lamp background outweighed the PL loss from the "deadlayer". Since the UV lamp background PL is 7.5 cd/m^2, the above equation can be expressed as,

$$I(cd/m^2) = 7.5 + 0.0032*(t - 1250)(\overset{o}{A}) \qquad (5\text{-}4)$$

5.2 Annealing of Zn_2GeO_4:Mn on PZT

5.2.1 Initial Study

Zn_2GeO_4:Mn films sputter deposited at room temperature on a PZT substrate with the conditions above were amorphous as identified by x-ray diffraction. Re-crystallization occurred upon annealing.

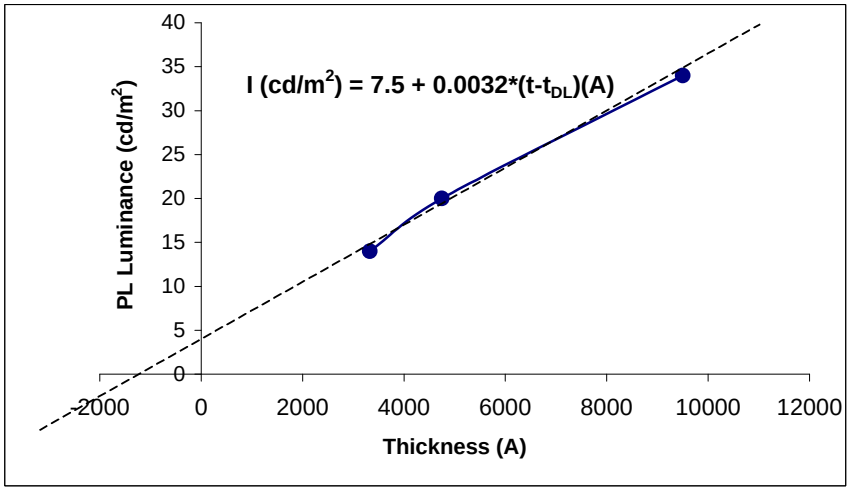

Figure 5-7 PL brightness vs. thickness for sputter deposited Zn_2GeO_4:Mn on PZT substrate

A deposition time of 5hrs. resulted in a film 1.3μm thick, The annealed samples were in box furnace in air at 700°C for 3.5 hrs, or 800°C for 20 mins. Photoluminescence was excited by the UV lamp, and the PL spectra are given in Figure 5-8. The data show that the PL intensity from the Zn_2GeO_4:Mn film annealed at the low temperature 700°C for 3.5hr is higher than the film annealed at 800°C for 20mins. Electroluminescence was also

obtained for the two films after deposition of an ITO top contact. The L-V data are shown in Figure 5-9.

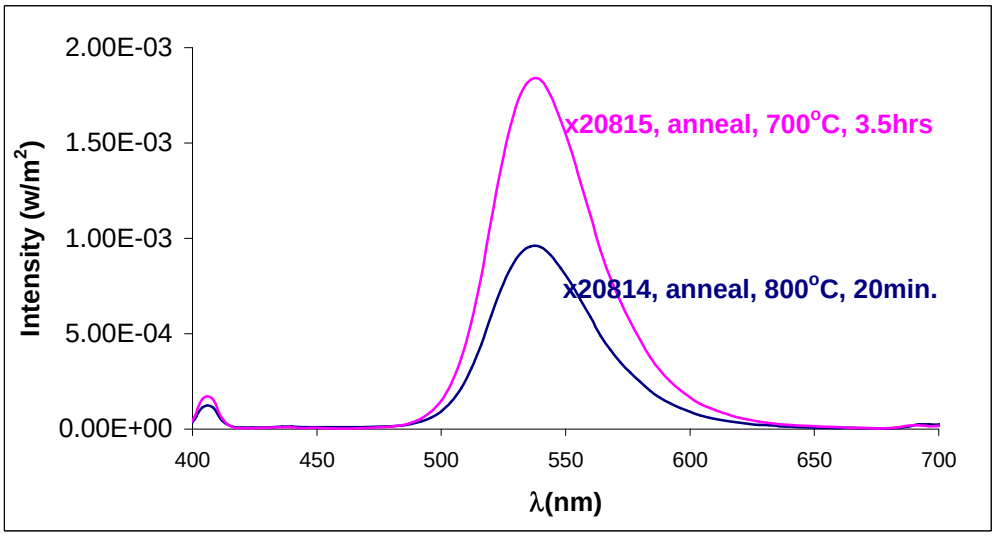

Figure 5-8 Photoluminescence emission spectrum of sputter deposited Zn_2GeO_4:Mn films on PZT at two different annealing recipes: 1) 700°C for 3.5hrs and 800°C for 20mins.

As for PL, the film annealed at 700°C for 3.5hrs exhibits a much higher EL brightness and much higher dL/dV than than that annealed at 800°C for 20 mins. The grain size of the films might give indirect information of how the films were re-crystallized. The SEM image of the two films are shown in Figure 5-10. The grain size of the film annealed at 800°C does are larger than for the film annealed at 700°C. This suggests that thermal diffusion limits re-crystallization. Diffusion is a function of temperature and time, given by the following equation:

$$J = \sqrt{D*t} * e^{-\frac{Q}{kT}} \qquad (5\text{-}5)$$

where D is diffusion coefficient, t is time, Q is thermal diffusion energy, and k is Boltzman constant, T is temperature at kelvin.

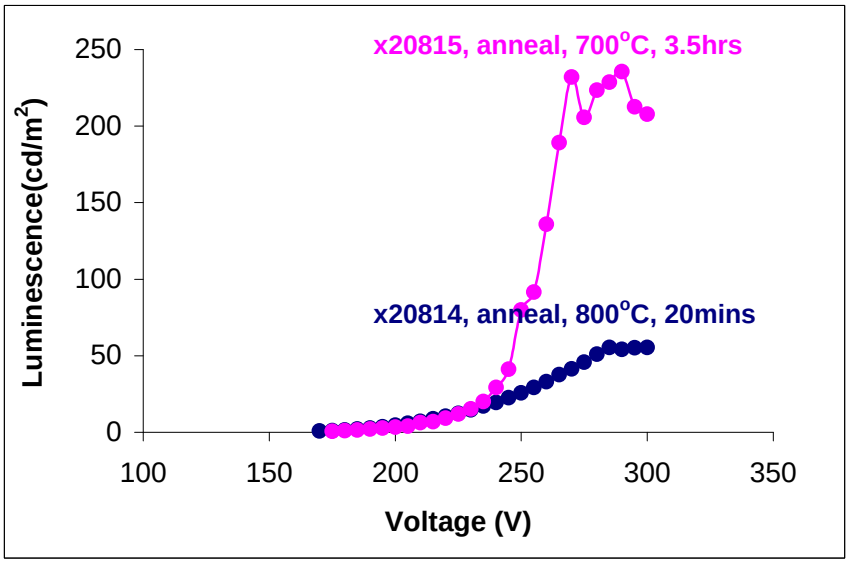

Figure 5-9 EL brightness vs. voltage curve of Al_2O_3/Au/PZT/Zn_2GeO_4:Mn/ITO ACTFEL devices for sputter deposited Zn_2GeO_4:Mn film annealed respectively at 700°C 3.5hrs and 800°C for 20mins.

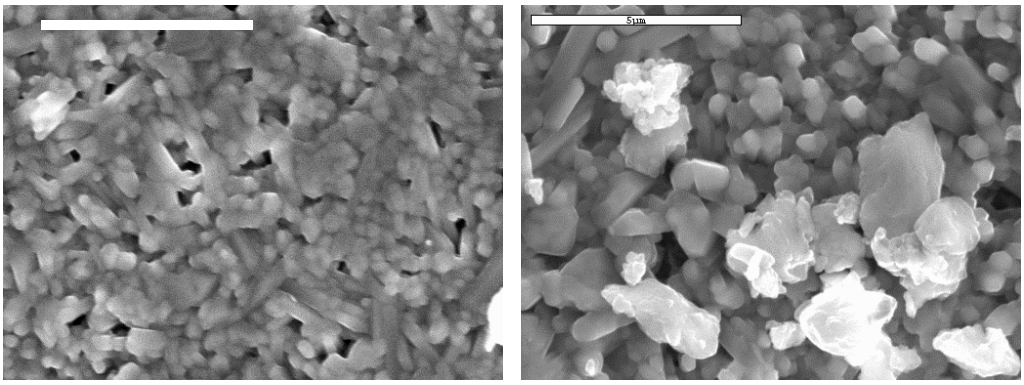

a) b)

Figure 5-10 SEM surface morphology image of sputter deposited Zn_2GeO_4:Mn on PZT substrate for annealing at two different recipes: 1) 700°C for 3.5hrs (x20815) and 1) 800°C for 20 mins (x20814)

The thermal diffusion is changed much faster with temperature than with time since the diffusion is exponentially dependent on temperature, while it is only square root linearly dependent on time. This theory is consistent with the above result and the annealing at 800°C for 20 mins should result in a better thermal diffusion than that the annealing at 700°C for 3.5hrs. X-ray diffraction patterns from the films are shown in Figure 5-11. Both films exhibit many new peaks after annealing in addition to peaks similar to those from the polycrystalline PZT substrate. The peaks which match the peaks of the Zn_2GeO_4:Mn target are labeled as Zn_2GeO_4 RB where RB refers to the Zn_2GeO_4 rhombohedral crystal structure of the target, as discussed in Section 4.3.1.

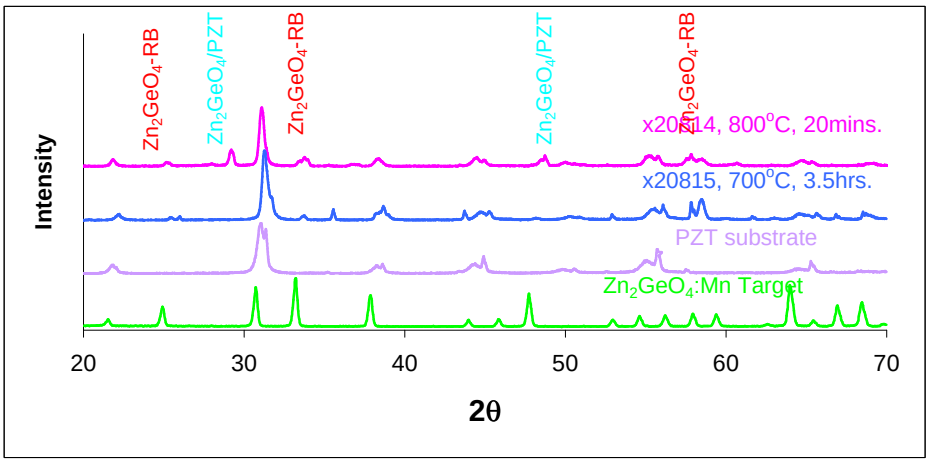

Figure 5-11 X-ray diffraction pattern of sputter deposited Zn_2GeO_4:Mn films on PZT for annealing respectively at 700°C for 3.5hrs. and 800°C for 20 mins, compared with the peaks from the Zn_2GeO_4:Mn target and from the PZT substrate.

The unknown new peaks are labled as Zn_2GeO_4/PZT where a reaction of the Zn_2GeO_4 layer with the adjacent PZT is hypothesized. The strongest Zn_2GeO_4:Mn peak from the films appears at 58°. This Zn_2GeO_4 peak intensity in the film annealed at 700°C for 3.5hrs appears higher and sharper than that in the film annealed at 800°C for 20 mins. This observation can partially support the enhanced PL and EL in the film annealed at

700°C for 3.5hrs. Comparison of the intensity and the position of each of the new peaks produced from the two annealed films is difficult and unpractical. The unknown new peaks could be from the re-crystallization of PZT layer. It's necessary to identify the unknown peaks which could be 1) from the Zn_2GeO_4 phase transformation from rhombohedral to cubic or tetrahedral, or 2) from PZT phase transformation, or 3) from the reaction of Zn_2GeO_4 and PZT. Next is going to identify them one by one.

The phase transformation of Zn_2GeO_4 could take place during annealing. Typical Zn_2GeO_4 crystal structures are rhombohedral, cubic and tetrahedral. As shown in Figure 5-12, it's unlikely that the new unknown peaks are either from tetrahedral or cubic Zn_2GeO_4:Mn crystallites. The target Zn_2GeO_4 sintered at 1050°C~1150°C was a perfect rhombohedral structure.

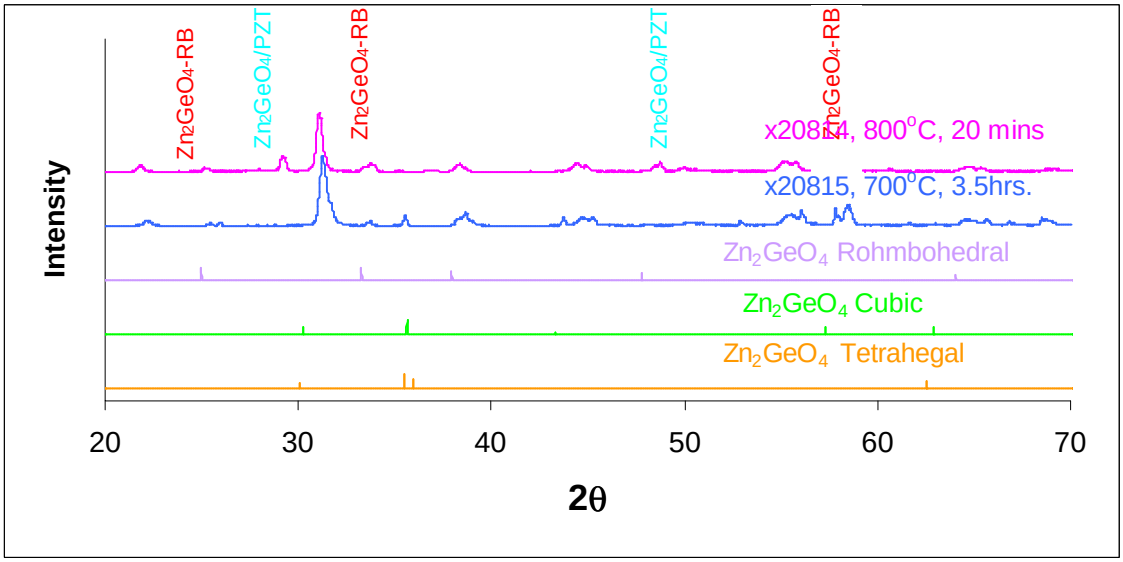

Figure 5-12 X-ray diffraction pattern of sputter deposited Zn_2GeO_4:Mn films on PZT substrate for annealing at 700°C for 3.5hrs. and 800°C for 20 mins, compared with the peaks of the standard Zn_2GeO_4:Mn romhbohedral, tetrahedral and cubic structure.

The film deposited from the target and re-grown from the amorphous during annealing is more likely to form the same phase structure rhombohedral as the target does. The hypothesis that Zn_2GeO_4 is transformed from rhombohedral to cubic or tetrahedral during annealing at 800^{o}C seems invalid.

5.2.2 Annealing Mechanisms

Morpholoy shown in Figure 5-10 is dominated by the particles of the PZT layer rather than the 1.3μm thick film of Zn_2GeO_4:Mn. This suggests that PZT layer itself could have recrystallized or have experienced a phase transformation. In order to prove it, the PZT substrates were annealed at three different recipes: 700^{o}C for 1 hr, 700^{o}C for 4.5 hrs and 800^{o}C for 1 hr.

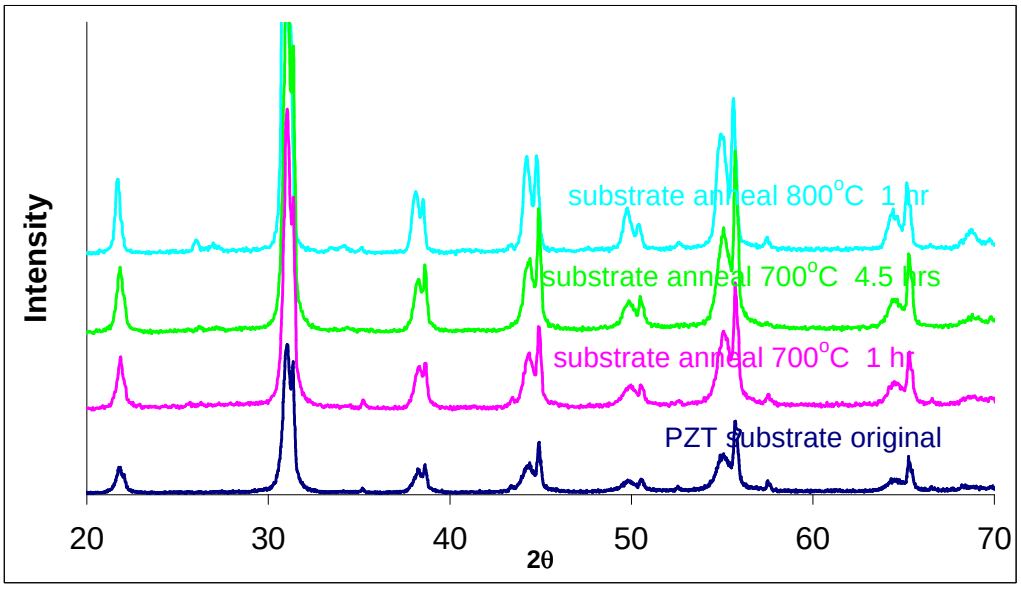

Figure 5-13 X-ray diffraction pattern of PZT substrate at structure Al_2O_3(0.5mm)Au(2000Å)/Pb(ZrTi)O_3(20μm) for annealing at three different recipes: 1) 700^{o}C for 1 hr, 2) 700^{o}C for 4.5hrs; and 3) 800^{o}C for 1 hr.

These annealing recipes allow the comparison of the temperature effect and the annealing time effect on the film performance independently. The x-ray diffraction pattern of the three PZT substrates is shown in Figure 5-13. No new peaks for any of the three substrates after annealing suggests that no phase transformation has taken place. The intensity of the peaks appears to increase upon annealing as expected.

To further investigate the new peaks observared when Zn_2GeO_4:Mn deposited on PZT was annealed , XRD pattern from Zn_2GeO_4:Mn annealed at the three annealing conditions are shown in Figure 5-14.

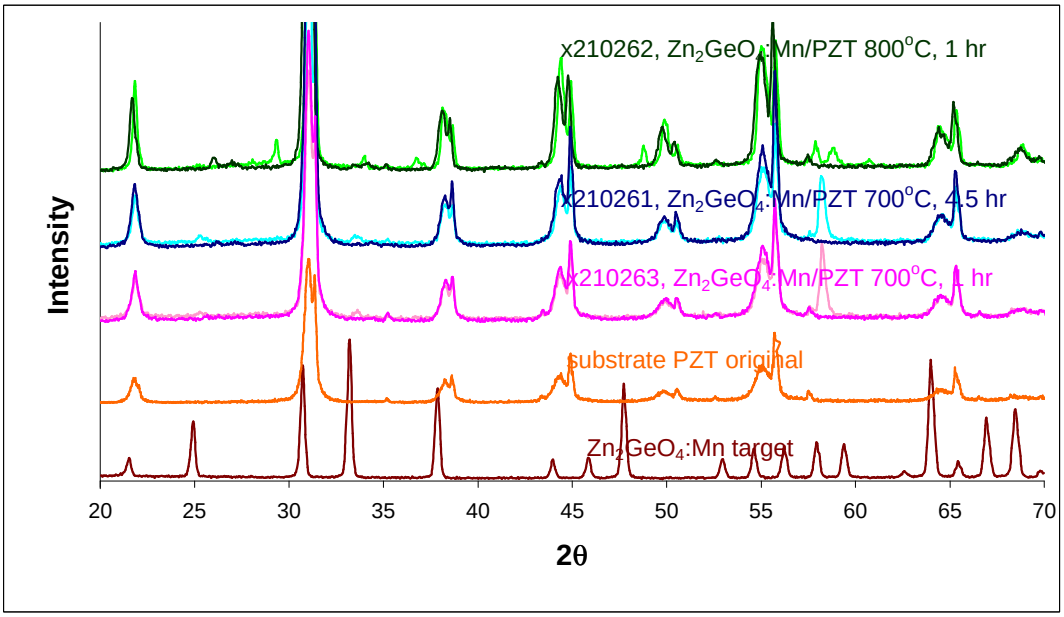

Figure 5-14 X-ray diffraction pattern of sputter deposited Zn_2GeO_4:Mn films on Al_2O_3/Au/Pb(ZrTi)O_3 substrate for annealing at three different recipes: 1) 700°C for 1hrs.; 2) 700°C for 4.5hrs and 3) 800°C for 1hrs.

XRD pattern from each of the films were compared with the pattern from the PZT substrate. From Figure 5-14, Annealing at 800°C for 20 mins created new peaks at 28 of 28°, 37°, 48°. A strong peak from rhombohedral Zn_2GeO_4 appears at 58° for all the three

films, and the two films annealed at 700°C for 1 hr and 3.5 hrs give a much stronger peak intensity at 58° than that at 800°C. It's clear that the annealing at 800°C definitely resulted in a better crystallization overall according to the number and the intensity of the new peaks produced after annealing. However, the re-crystallization is more the result of the reaction of Zn_2GeO_4:Mn and PZT. This reaction probably is the primary reason that the PL and EL is much lower in the film annealed at 800°C compared with that in the film annealing at 700°C.

The photoluminescence spectra provides further evidence supporting the conclusion that annealing at 700°C for long time is better than at 800°C for 10 mins. The PL spectrum for the three films are shown in Figure 5-15,

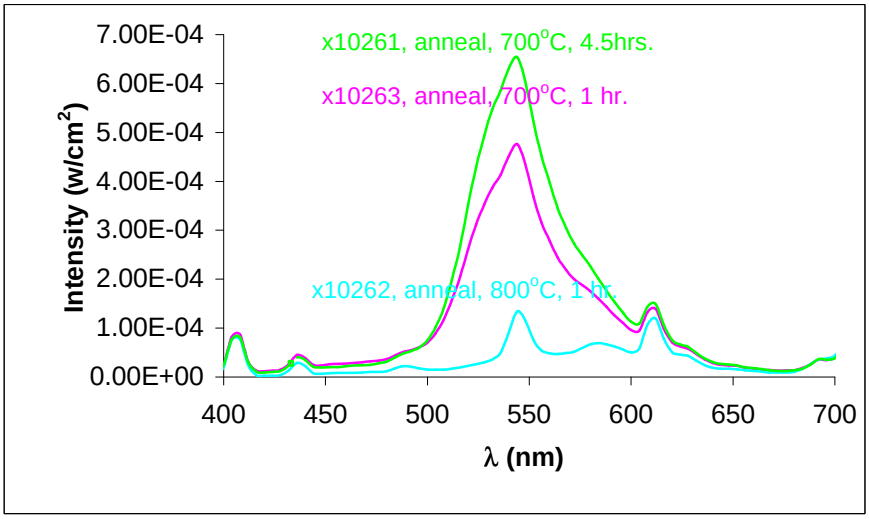

Figure 5-15 Photoluminescence emission spectrum of sputter deposited Zn_2GeO_4:Mn films on PZT substrate for annealing at three different recipes: 1) 700°C for 1 hrs.; 2) 700°C for 4.5hrs and 3) 800°C for 1 hrs.

As shown in Figure 5-15, the films annealed at 700°C demonstrate stronger photoluminescence than films annealed at 800°C. In addition, the film annealed at 700°C for 4.5hrs even gives a slightly better PL than that annealed at the same temperature for 1

hour. This 700°C anneals shows that longer times did enhance the PL intensity. Enhanced PL intensity could be the result of better crystallinity or rougher film surface, both of which should result from the longer annealing time.

To further investigate the parameter of annealing time, the film annealed at 700°C for 4.5 hrs was annealed for another 6.5 hrs for a total of 11 hrs. The PL spectra are compared in Figure 5-16,

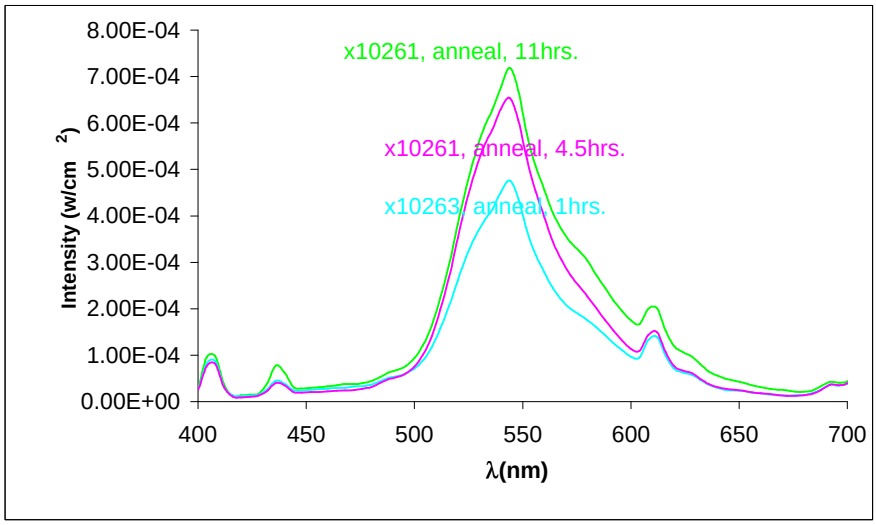

Figure 5-16 Photoluminescence spectrum of sputter deposited Zn_2GeO_4:Mn films on PZT substrate for annealing at 700°C for three time periods:1)1 hr. 2)4.5hrs; and 3)11hrs.

The film annealed for 11 hours (4.5hrs + 6.5 hrs.) exhibited a PL intensity much and slightly higher than films annealed for 1 hr or 4.5hrs respectively. X-ray diffraction pattern from the three films are plotted in Figure 5-17. As shown in the x-ray patterns, the intensity of Zn_2GeO_4:Mn RB peaks from the 700°C , 4.5hrs don't changed after annealing for another 6.5 hours. The PZT peaks do increase after another 6.5 hrs annealing. In addition, x-ray diffraction pattern of the film annealed for 4.5+6.5hrs. is shifted to the right, compared with that from the other two films. This shift might be

caused by the difference of the sample position relative to the x-ray detector position. When the sample height is different, or the sample is placed tilted, the angle 2θ will change, that is the reason why the whole x-ray diffraction pattern is shifted.

Four Zn_2GeO_4:Mn films were deposited on single crystal silicon to study the effect of Si versus PZT on Zn_2GeO_4:Mn during annealing. One of the as-deposited films was used as a reference.

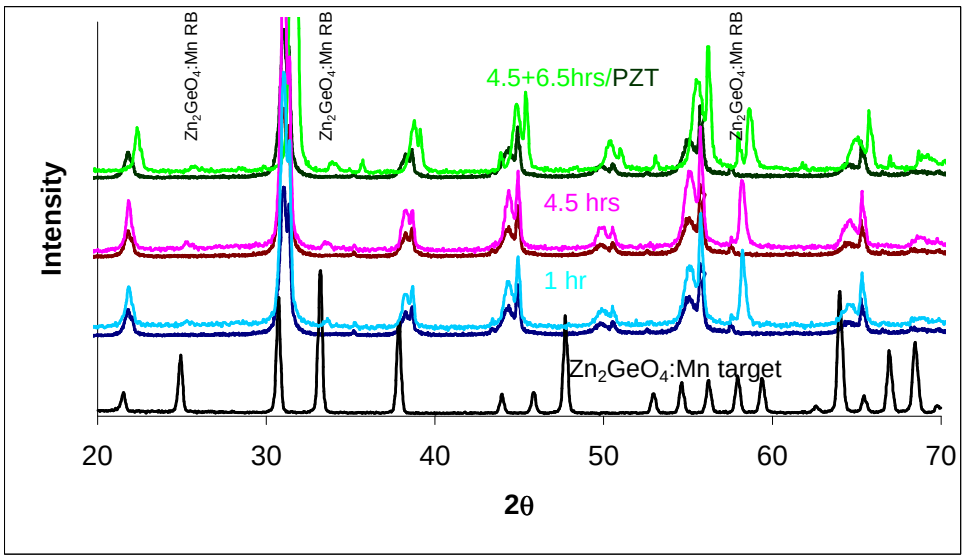

Figure 5-17 X-ray diffraction pattern of sputter deposited Zn_2GeO_4:Mn films on PZT substrate for annealing at 700°C for three time period: 1)1 hr; 2) 4.5hrs; and 3)11 hrs

The other three were annealed at three annealing recipes: 1) 700°C for 1 hr. 2) 700°C for 4.5hrs; and 3) 800°C for 1.5hrs. The x-ray diffraction patterns are shown in Figure 5-18. The as-deposit film was amorphous, similar to those on PZT. The peak at 28° is from the Si (100) substrate. In the film annealed at 700°C for 1 hr., three major Zn_2GeO_4 rhombohedral peaks at low angles appear. For the film annealed at 700°C for 4.5hrs, the same three major peaks were increased and the other Zn_2GeO_4 rhombehedral peaks appear too. For the film annealed at 800°C for 1.5 hrs, additional re-crystallization of

Zn_2GeO_4:Mn is observed. Both higher annealing temperature and annealing time results in a better crystallization, but the annealing at 700°C for 4.5hrs slightly outweighed the annealing at 800°C for 1.5 hrs in term of the peak intensity. This latter result is consistent with the result obtained of annealed Zn_2GeO_4:Mn on PZT discussed above.

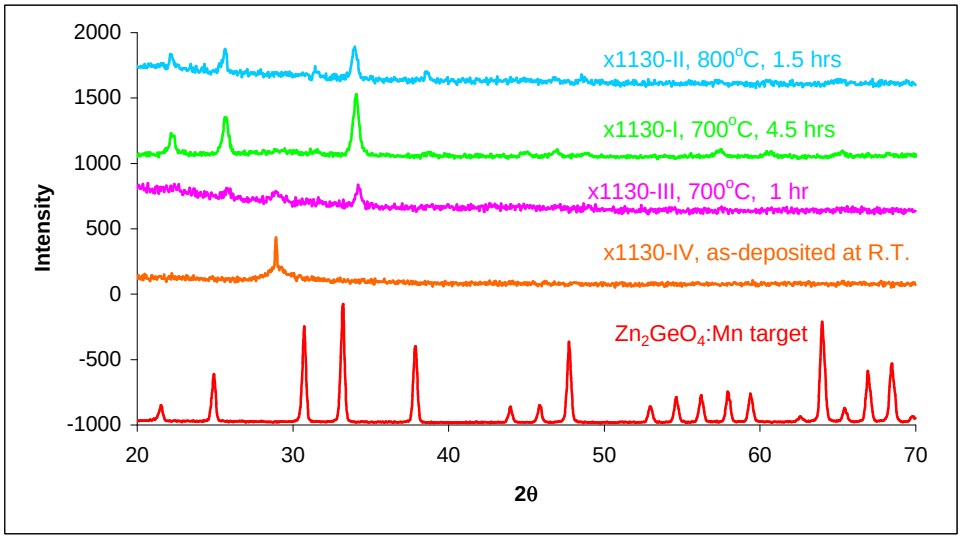

Figure 5-18 X-ray diffraction pattern of sputter deposited Zn_2GeO_4:Mn on Si at room temperature for annealing at three recipes: 1) 700°C for 1hr; 2) 700°C for 4.5hrs; and 3)800°C for 1.5 hrs.

5.3 Summary and Discussions

5.3.1 Annealing of Zn_2GeO_4:Mn on PZT

Films deposited at room temperature and 250°C were amorphous, according to x-ray diffraction data. Annealing at high temperature caused re-crystallization of Zn_2GeO_4. The Zn_2GeO_4:Mn annealed at 700°C was not well crystallized. When the annealing temperature went up to 800°C, the Zn_2GeO_4:Mn crystallinity was improved, but the PL and EL performance (Figure 5-8 and Figure 5-9) degraded. Zn_2GeO_4:Mn annealed at

700^{o}C for 3.5 hrs demonstrated a much better PL and EL intensity than that annealed on 800^{o}C for 2hrs. The effects of annealing temperature versus annealing time needs further discussions. The SEM image for the two films show that the grain size of the film on PZT annealed at 800^{o}C for 20 mins is larger than that of the film annealed at 700^{o}C for 3.5 hrs. (Figure 5-10). The x-ray diffraction pattern of the two films were complicated (Figure 5-11). Zn_2GeO_4:Mn recrystallization is seen in the two films after annealing. But the PZT substrate recrystallization was also seen. Some of Zn_2GeO_4:Mn peaks overlapped with the PZT peaks and making it difficult to isolate one from another. More peaks appear from the film annealed at 800^{o}C. Whether the peaks are associated with enhancement of PL and EL performance needs to be further investigated. New peaks could result from the three different mechanisms: 1) Zn_2GeO_4 phase transformation from rhombohedral to tetrahedral or cubic; 2) PZT phase transformation or new crystal structures from reaction of Zn_2GeO_4 and PZT. Comparing the x-ray diffraction pattern of the films with the Zn_2GeO_4 tetrahedral and cubic structure reference peaks, none of the new peaks match well with the peaks from tetrahedral or cubic phases. The x-ray diffraction of Zn_2GeO_4:Mn deposited on Si (Figure 5-18) confirmed that the Zn_2GeO_4:Mn annealed at 700^{o}C and 800^{o}C in the Zn_2GeO_4 rhombohedral structure. Annealing of the PZT substrates and no new x-ray diffraction peaks show the conclusion that no new PZT phases were formed. Some of the PZT peaks were increased, suggesting the PZT re-crystallized upon annealing. No phase transformations were observed after annealing. The only remaining possibility is that reaction between Zn_2GeO_4 and PZT. To identify the new peaks of Zn_2GeO_4:Mn on PZT after annealing, Zn_2GeO_4:Mn films on PZT were annealed at 700^{o}C for different time between 1 hr and 4.5 hrs. The other two

films were annealed for 2.5 hrs at different temperatures between 700°C and 800°C. The x-ray diffraction results (Figure 5-14) indicated that annealing for a longer time at 700°C increased Zn_2GeO_4 peaks, but annealing at higher temperature 800°C produced new peaks, which supports the statement that the new peaks are the result of reaction of Zn_2GeO_4 and PZT.

5.3.2 Comparison of PLD and SD Zn_2GeO_4:Mn Films

Electroluminescence was demonstrated for the first time from pulsed laser deposited (PLD) film. These films were compared to sputter deposited (SD) Zn_2GeO_4:Mn ACTFEL device using PZT dielectric layers.

The EL results show that the brightness of PLD films were greater than SD films, as shown in Figure 5-19. Both the films were annealed at 750°C in air for 2.5hrs.

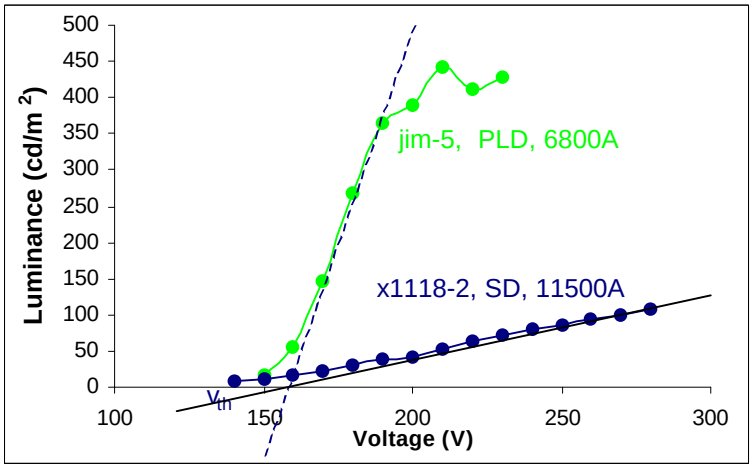

Figure 5-19 Electroluminescent brightness vs. voltage curve of the Zn_2GeO_4:Mn ACTFEL devices deposited by two deposition techniques: 1) pulsed laser deposition; and 2) RF sputtering deposition.

The 6800Å Zn_2GeO_4:Mn film grown by pulsed laser deposition demonstrated the highest EL brightness (450cd/m^2) at a 2.5kHz, while the 11500Å Zn_2GeO_4:Mn film grown by sputtering deposition gave the highest brightness only (110cd/m^2). Generally, thicker films are brighter, where the opposite is seen here. It should be noted that the annealing recipe for the two films was slightly different. The PLD film was annealed at 750^{o}C for 1.5 hrs., while the SD film was annealed at 700^{o}C for 2.5 hrs. As discussed in Section 5.2.2., temperature higher than 700^{o}C gave dramatically degraded both PL and EL performance. In this point, the PLD film annealed at 750^{o}C should give a lower brightness than the SD film which was annealed at 700^{o}C. But, the result is reverse. Point defect is speculated to be responsible for the enhanced EL performance in PLD films.

Another possible explanation for higher EL brightness for PLD versus SD films would be the substrate temperature. The PLD was grown at a substrate temperature of 250^{o}C, while the SD film was grown at room temperature. The x-ray diffraction patterns from films grown by PLD and SD are compared in Figure 5-20.

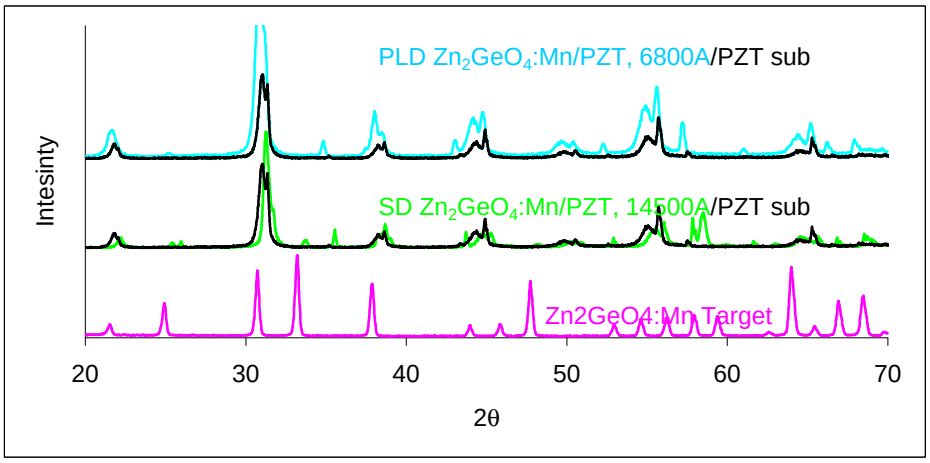

Figure 5-20 X-ray diffraction pattern of Zn_2GeO_4:Mn deposited on PZT by two growth techniques: 1) pulsed laser deposition and 2) RF sputtering deposition.

Extra diffraction peaks from polycrystalline rhombohedral Zn_2GeO_4:Mn is seen in both the films. The Zn_2GeO_4 peak at 58^o appear stronger in the PLD film than that in the SD. This peak doesn't appear at the same position in the two films due to the pattern shift. The pattern shift can be seen when compared with the peaks from the same PZT substrate. As shown in the patterns, the pattern of the SD film is shifted slightly to the right, and the pattern of the PLD one shifted slightly to the left, which makes the relative shift of the two patterns is even larger. It is evident that the re-crystallization of Zn_2GeO_4:Mn in the PLD film was better than that in the SD film. As discussed above, the annealing at 750^oC for 1.5 hrs. in the PLD film shouldn't result in a better re-crystallization than that the annealing at 700^oC for 2.5 hrs. The x-ray diffraction pattern of annealed Zn_2GeO_4:Mn films was complicated by the overlapping polycrystalline PZT diffraction peaks and frequently overlapped with new peaks from the reaction products from Zn_2GeO_4 and PZT. To clarify these facts, x-ray diffraction patterns of Zn_2GeO_4:Mn films pulsed laser deposited on Si at substrate temperatures R.T and 250^oC were compared. Both of them were annealed at the same condition of 24hrs at 800^oC, and almost all the rhombohedral Zn_2GeO_4 peaks are evident from the film deposited at 250^oC. In contrast, the film deposited at room temperature exhibits only very weak peaks, but these matched the rhombohedral target pattern very well. This data show that the substrate temperature is a critical dominating factor controlling Zn_2GeO_4:Mn re-crystallization. This can be also speculated by the fact that the Zn_2GeO_4:Mn crystallization temperature (650^oC) is high.[46]

Another factor potentially responsible for the enhanced EL performance of PLD films could be the atom energy transferred from the power source (laser versus Ar

plasma). For the Zn_2GeO_4:Mn sputtering deposition, 25W power was applied to the 1" target. Assuming all the energy is transferred to the sputtered atoms by Ar plasma, the power by area is 5 J/cm^2-s. For Zn_2GeO_4:Mn pulsed laser deposition, each 20ns pulse gives a laser energy density 1.6J/cm^2, which is equivalent to an continuous laser power density of $8x10^8$J/cm^2-s. This huge laser power density causes the target to be ablated. Since the laser repetition rate was 10Hz, the average laser power density is 16J/cm^2-s. Thus, the average PLD power is four times of the sputtering power.

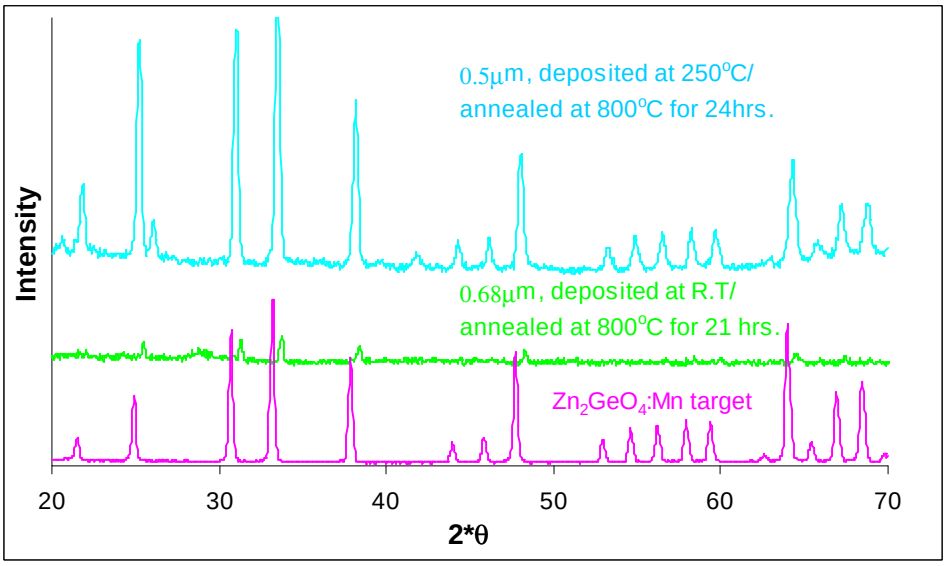

Figure 5-21 X-ray diffraction pattern of the Zn_2GeO_4:Mn film deposited on two different substrate temperatures: 1) room temperature and 2) 250°C, and both followed by an annealing at 800°C for over 20hrs

Therefore, pulsed laser deposition transfer more energy to the atoms knocked off the target and the atoms would have a higher surface mobility before they rest on the substrate surface. This higher mobility should be an advantage for the film growth on

rough PZT substrate. More details about how the PZT substrate roughness effects EL performance will be discussed in next section.

The crystallinity for the PLD film is slightly better than that for the SD film, according to the x-ray diffraction results (Figure 5-20). The result from the SEM image of the two films (Figure 5-22) show larger grain size for 750^{o}C annealed PLD vs. 700^{o}C annealed SD films

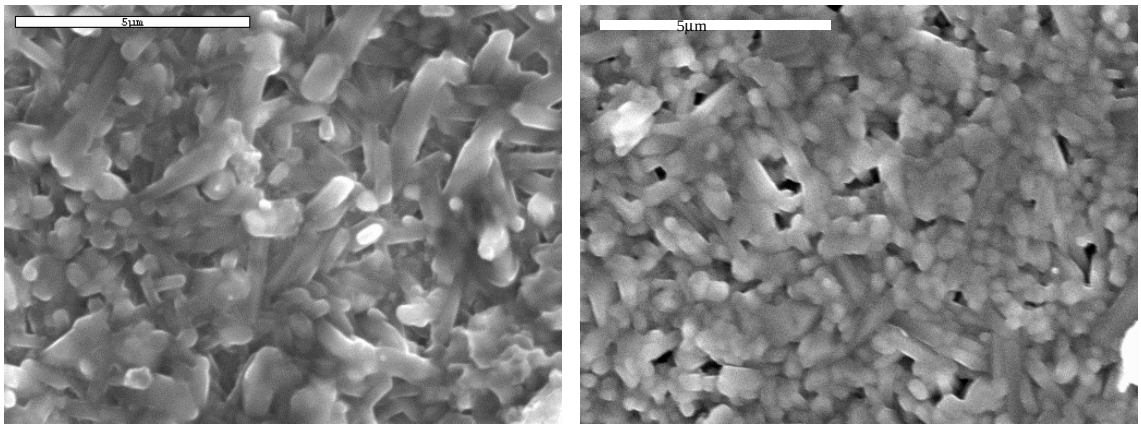

a) b)

Figure 5-22 SEM Image of Zn_2GeO_4:Mn film deposited by two different deposition techniques: a) pulsed laser deposition at T_s = 250^{o}C and T_a = 750^{o}C for 1.5hrs and b) RF sputtering deposition at T_s = R.T. and T_a = 700^{o}C for 2.5hrs.

The enhanced EL from PLD films is attributed to the difference in charge transfer. The Q-V curve of the films grown respectively by pulsed laser deposition and RF sputtering deposition were obtained and shown in Figure 5-23. As shown in Figure 5-23, after the threshold voltage (160V) is reached, the charge transfer in the PLD film is larger (20µC and 50µC at 190V and 230V respectively). The charge transfer in the SD film is small after the threshold voltage is reached. For the case of 220V, the charge transfer is only 4µC.

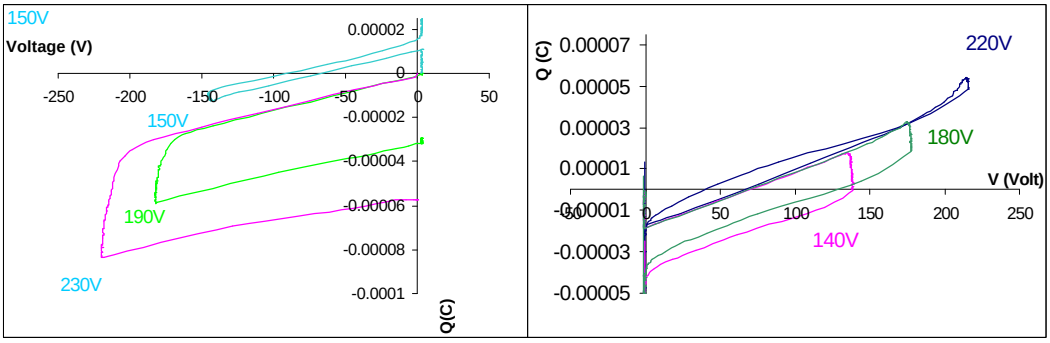

a) b)

Figure 5-23 Q-V Curve of Zn_2GeO_4:Mn film deposited by two different deposition techniques: a) pulsed laser deposition at T_s = 250°C and annealed at 750°C for 1.5 hrs and b) RF sputtering deposition at T_s = R.T. and annealed at 700°C for 2.5 hrs.

With increased transfer charge, more electrons are available to excite luminescent centers. This increased charge transfer could be related to the interface of Zn_2GeO_4:Mn and PZT.[84, 85]

The charge transfers are shown in Figure 5-24. The charge flows during the 30μs stay time of the voltage pulse for the PLD film; while the charge almost remains unchanged during the 30μs stay time. The current shape and dropping bumps are also the important information to understand the charge transferring.[74, 86]

5.3.3 Zinc deficiency of Zn_2GeO_4:Mn films

As discussed in Chapter 5, the Zn/Ge ratio shown in the EDX results for pulsed laser deposited Zn_2GeO_4:Mn was 0.77~0.83, but the x-ray diffraction pattern for the films show only Zn_2GeO_4:Mn rhombohedral structure. The EDX result seems not accurate.

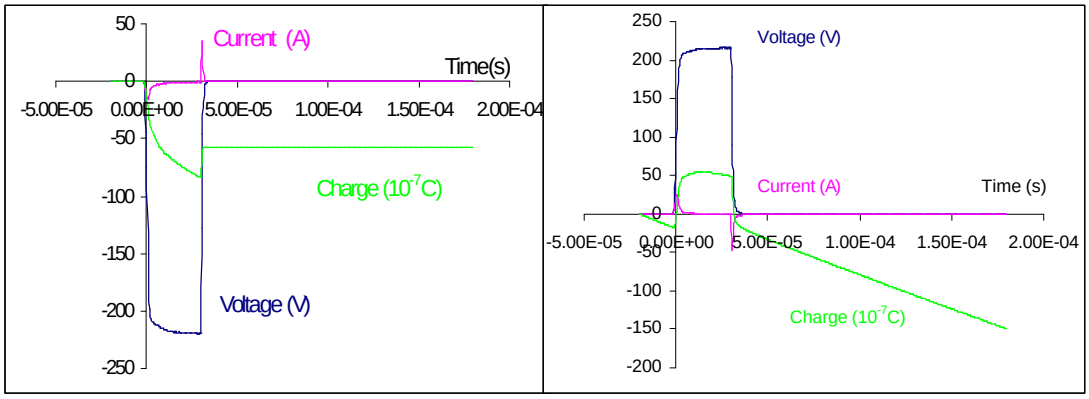

a) b)

Figure 5-24 Current, voltage and charge vs. time curve of Zn_2GeO_4:Mn film deposited by two different deposition techniques: a) pulsed laser deposition at T_s = 250°C and T_a = 750°C for 1.5hrs and b) RF sputtering deposition at T_s = R.T. and T_a = 700°C for 2.5hrs.

The EDX results for the sputter deposited Zn_2GeO_4:Mn were 0.99~1.04.[46] This Zn/Ge ratio is much higher than that in the pulsed laser deposited Zn_2GeO_4:Mn films. The assumption is that if the pulsed laser deposited Zn_2GeO_4:Mn is stoichiometric (Zn:Ge = 2:1), the sputter deposited Zn_2GeO_4:Mn should be Ge-rich. The Ge containing phases should exist in the sputter deposited Zn_2GeO_4:Mn films. The Ge rich phases could be $ZnGeO_3$ or simply GeO_2. If a Zn_2GeO_4 film contains Zn_2GeO_4, $ZnGeO_3$ and GeO_2. The environment of Ge^{4+} for the different phases should be different. XPS was used to identify the chemical band of Ge^{4+}. The result is shown in Figure 5-25. The Ge^{4+} LMM Auger electron peak in GeO_2 should be located at 115.9eV. The only peak observed near 115.9eV is 117eV. This information can't confirm whether GeO_2 is in the Zn_2GeO_4 film since the peak could be shifted due to surface charging. Fortunately, the shift can be calibrated by using the carbon reference peak.

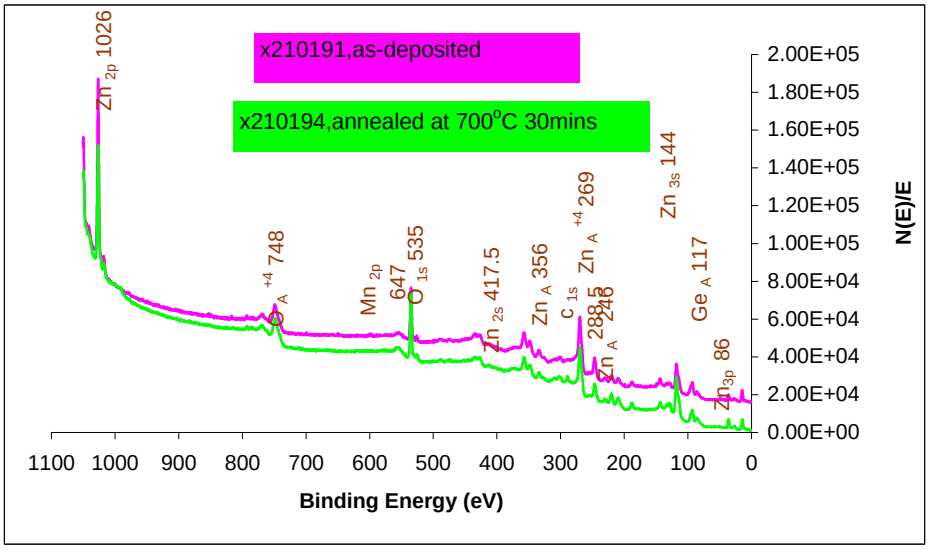

Figure 5-25 X-ray photo-electron spectrum of sputter deposited Zn_2GeO_4:Mn films on PZT

But, the most important is to identify how many peaks appears at the energy near to 115.9eV, which are the characteristic peaks of Ge^{4+}. The LMM Auger peak of Ge^{4+} in different environments would shift. If $ZnGeO_3$ or GeO_2 coexist in the Zn_2GeO_4film, more than one Ge^{4+} LMM Auger peaks should be seen in the XPS spectrum. As shown in the zoomed spectrum (Figure 5-26) , a bump is seen at 114eV. This is the peak shadowed by the large peak 117eV. Therefore, two Ge^{4+} peaks are observed. This refers that the Ge containing phase other than Zn_2GeO_4:Mn exist in the film. In this point, it is more appropriate to say that the pulsed laser deposited Zn_2GeO_4:Mn is stoichiometric, while the sputter deposited Zn_2GeO_4:Mn is Ge rich. According to the EDX results, it could conclude as well that the sputter deposited Zn_2GeO_4:Mn is stoichiometric, while the pulsed laser deposited Zn_2GeO_4:Mn is Zn-deficient.

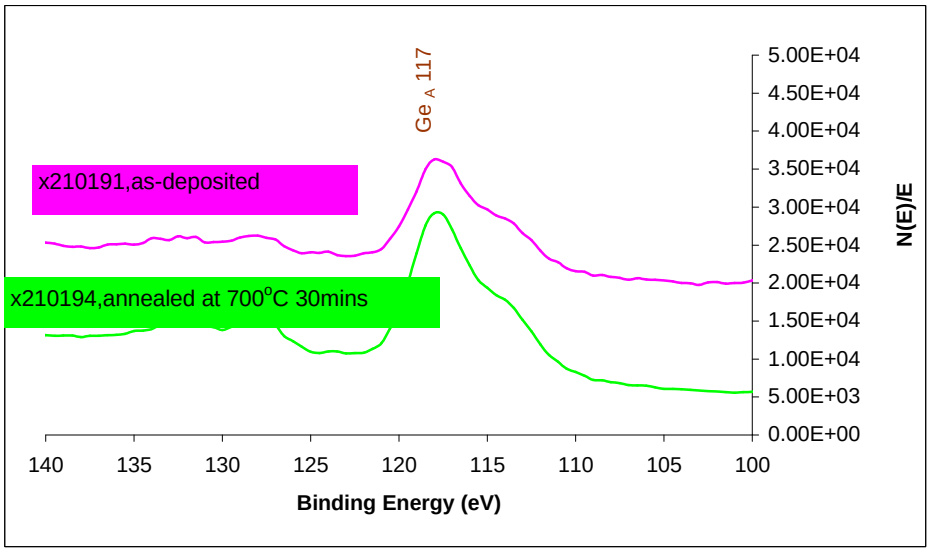

Figure 5-26 X-ray photo-electron spectrum of sputter deposited Zn_2GeO_4:Mn films on PZT to identify Ge^{4+}

Which one is true depends how accurate the EDX results are. The strong evidence is that Zn_2GeO_4:Mn grown by pulsed laser deposition was stoichiometric according to the x-ray diffraction. Therefore, the former assumption is more likely true that the pulsed laser deposited Zn_2GeO_4:Mn is stoichiometric while the sputter deposited Zn_2GeO_4:Mn is Ge-rich.

5.3.4 Effect of PZT Roughness

According to literature reports, leakage current of ZnS:Pr on Ta_2O_5 is increased with increased surface roughness and the C-V curve in the transition region is less steep.[85, 87] When the thickness of Zn_2GeO_4:Mn layer was decreased to 5000Å, the EL brightness was dramatically reduced. This trend is completely different from how the PL brightness changes with the thickness as discussed in Section 5.1.4. The PL brightness was almost linearly increased with the thickness and the "dead layer" is only less than

1250Å (Figure 5-7). But this is not the case for the EL. The EL brightness vs. voltage curve for the thickness of 4750Å and 11150Å is shown below. The 11150 Å film is much brighter than the 4750 Å film.

Figure 5-27 L-V curve of sputter deposited Zn_2GeO_4:Mn on PZT at different

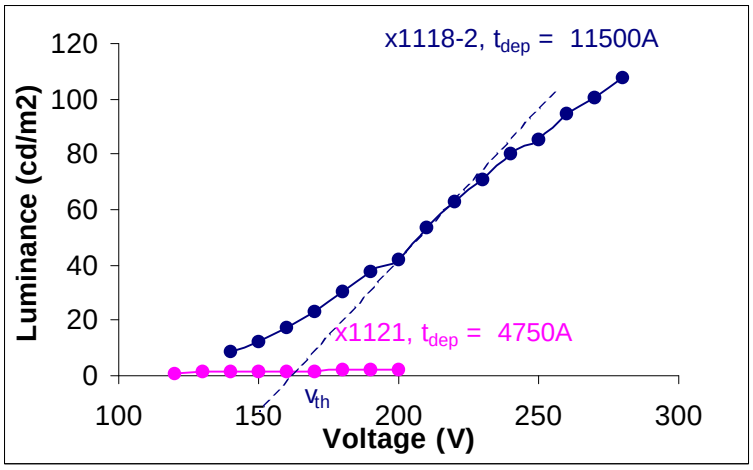

thicknesses: 1) 4750Å and 2)11500Å

The brightness for the 4750Å film is extremely low. Generally, the EL brightness is proportional to the thickness.[12]

A model of non-continuous Zn_2GeO_4:Mn layer on rough PZT layer is discussed to explain why the brightness is low in the thin (4750Å) Zn_2GeO_4:Mn layer on PZT. Since the PZT layer surface is extremely rough (Figure 4-4), the Zn_2GeO_4:Mn almost certainly is discontinuous, especially in the PZT surface valley area. The discontinuous Zn_2GeO_4:Mn layer is shown in Figure 5-28. A discontinuous layer is supported by the EDX results. The Pb, Zr and Ti peaks were detected in the EDX spectrum of the Zn_2GeO_4:Mn deposited on PZT even when the average Zn_2GeO_4 layer thickness was over 1.3μm.

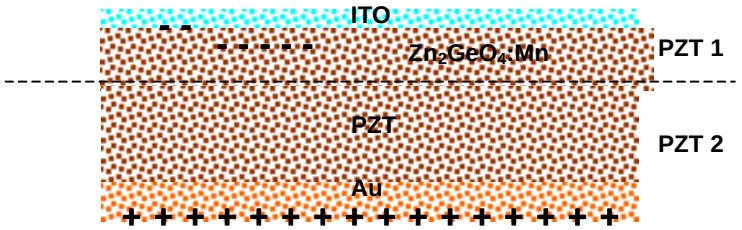

Figure 5-28 Schematic of non-continuous Zn_2GeO_4:Mn film on rough PZT substrate

For this to be true, either the 15keV primary electrons penetrated into the underlying PZT, or some of the PZT was not covered by Zn_2GeO_4 surface layer. The 1μm Zn_2GeO_4:Mn film deposited on Si completely blocked the Si.

In this case, the equivalent capacitance of the EL is from three parts: PZT part 1, PZT part 2 and Zn_2GeO_4:Mn. PZT part 1 is the bumps which are adjacent to the isolated Zn_2GeO_4:Mn islands in Figure 5-28. The equivalent circuit is shown in Figure 5-29. The thickness of PZT part 1 (< 0.5μm of the Zn_2GeO_4:Mn layer) should be much smaller than that of the underlying PZT layer (20μm). The thickness difference is almost a factor of 40. Therefore, the capacitance of PZT part 1 C_{pzt-1} should be much larger than that of PZT part 2 C_{pzt-2} in term of $C = \varepsilon*(A/t)$, where A is the area and t is the thickness and the capacitance difference is at a factor of 40 as well.

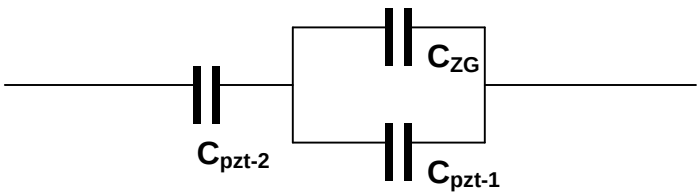

Figure 5-29 Electric equivalent circuit of non-continuous Zn_2GeO_4:Mn film on rough PZT substrate

It has been identified that the capacitance of the Zn_2GeO_4:Mn layer is similar to that of the PZT layer (Table 4-3). C_{ZG} here stands for the capacitance of all the isolated Zn_2GeO_4:Mn island together. Since the C_{ZG} and the C_{pzt-1} are connected in parallel, the total capacitance of the two is simply the addition of the two individual ones $C_{total-parallel} = C_{ZG} + C_{pzt-1}$. Since C_{pzt-1} (~ $40*C_{pzt-2}$) is much greater than C_{ZG} (~C_{pzt-2}), the total capacitance $C_{total-parallel}$ is almost from C_{pzt-1}. In this case, the voltage dropped on the phosphor is given by $V_{ZG} = V_a * C_{pzt-2} / (C_{total-parallel} + C_{pzt-2})$. Since $C_{total-parallel}$ is almost C_{pzt-1} and the C_{pzt-1} (~$40*C_{pzt-2}$) is much larger than C_{pzt-2}, V_{ZG} becomes extremely small. The internal field E cross the Zn_2GeO_4:Mn is accordingly small in term of E = V/t. This means that the same voltage applied to the device, a much smaller portion of the voltage dropped on the Zn_2GeO_4:Mn phosphor layer and most of it dropped through the underlying PZT layer.

The effect of PZT substrate roughness on the Zn2GeO4:Mn EL brightness can be further supported by the EL result of Zn_2GeO_4:Mn on smooth glass/ITO/ATO. For the Zn_2GeO_4:Mn layer at small thickness (5000Å), the EL brightness on glass/ITO/ATO was much better than that on PZT even if the re-crystallization of Zn_2GeO_4:Mn on glass/ITO/ATO was much poorer than that on PZT substrate due to the much shorter allowed annealing time. The Zn_2GeO_4:Mn film on PZT was generally annealed at 700^{o}C~800oC for a couple hours while the Zn_2GeO_4:Mn on glass/ITO/ATO wasn't allowed for any annealing at 800^{o}C over 2 minutes Two films were deposited respectively on PZT substrate and glass/ITO/ATO substrate. Both were deposited at the same condition: Ar 70 sccm/ O_2 30 sccm, working pressure 15mT, substrate temperature and deposition time 100 minutes, which gave a 4750Å thickness.

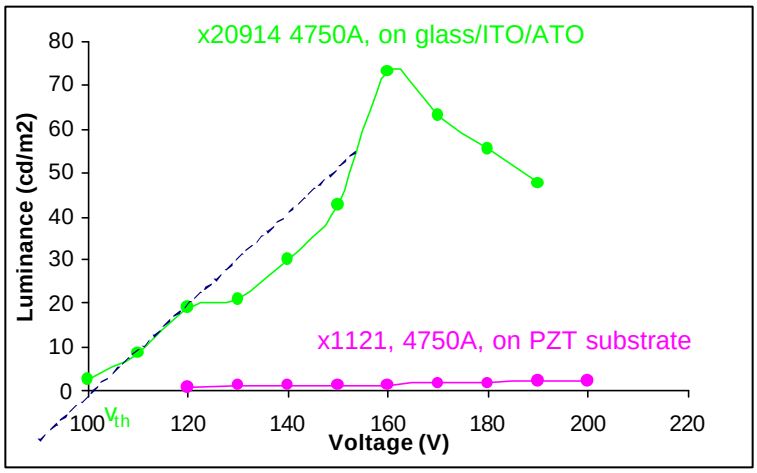

Figure 5-30 L-V curve of sputter deposited on Zn_2GeO_4:Mn film on PZT substrate and glass/ITO/ATO

As shown in Figure 5-30, the film deposited on glass/ITO/ATO demonstrates a much higher EL brightness and a sharper turn-on slope. This further supports the above model that the rough PZT substrate surface reduced the voltage drop through the Zn_2GeO_4:Mn phosphor layer, resulting in a decreased EL brightness. As shown in Figure 5-31, the charge transfer at the threshold voltage region (140V) for the film deposited on glass/ITO/ATO changes rapidly from 800μC to 1800μC/cm^2 of 1mC/cm^2. The charge transfer for film deposited on PZT is only 400μC/cm^2. The charge transfer for the film deposited on glass/ITO/ATO was much greater than that deposited on PZT consistent with a larger EL brightness.

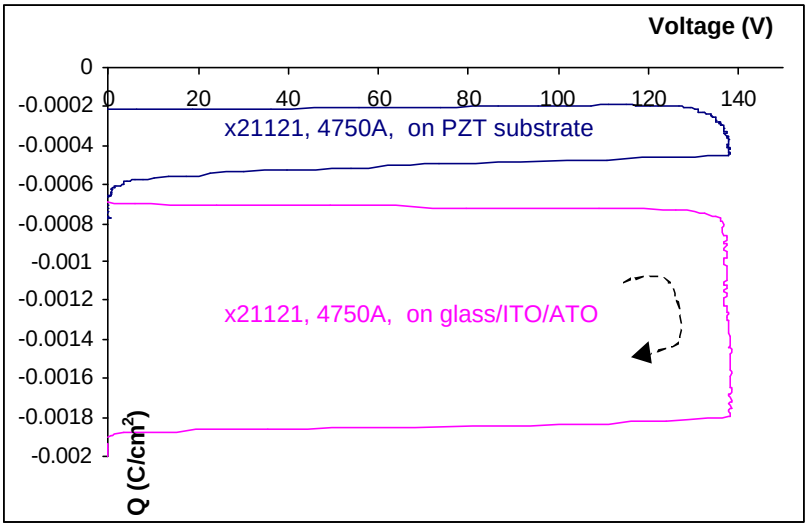

Figure 5-31 Q-V curve of sputter deposited on Zn_2GeO_4:Mn film on PZT substrate and glass/ITO/ATO

CHAPTER 6
$Zn_{1-x}Mg_xS:Mn$

6.1 Introduction

The optical transition energy from the A_4 to T_6 states of Mn^{2+} ion is increased when its crystal field is reduced.[16] Since electrons in the 3d shell are not shielded in the Mn^{2+} ion, its crystal field can be modified by its host material. The crystal field for a Mn^{2+} ion is determined primarily by the types and distance of atoms (ions) in the nearest and next nearest neighboring. Therefore, any change of lattice parameter, crystal structure and (or) electronegativity of host material could result in the change of crystal field. Allowed optical transition of Mn^{2+} in host ZnS exhibits orange color emission. If the crystal fields around Mn^{2+} were reduced, the transition of Mn^{2+} could green shift i.e. a photon with a shorter wavelength than orange, could be emitted. If Mg^{2+} were to replace Zn^{2+} in ZnS it could expand the lattice and thereby result in a reduced crystal field. Green shifted emission from a ZnMgS:Mn ACTFEL devices with a $SiON_x$ dielectric layer were first reported by Noma et al.[43] In this research, the electron-beam evaporation technique discussed in Chapter 3 was used for ZnMgS:Mn thin films and test ACTFEL devices. Two different Mn^{2+} sources (MnS and metal Mn) were studied as was the effect of the ZnMgS microstructure on EL brightness. The EL brightness reported from ZnMgS:Mn films (335 cd/m^2,[43]) was much lower than ZnS:Mn (5000 cd/m^2, [16]) and the hypothesis to be tested was that the solution of Mg in ZnS restricted the host crystallinility.

6.2 Experimental Results

6.2.1 $Zn_{1-x}Mg_xS$:Mn Source Pellet

The ZnMgS:Mn source was made into an 1/4" diameter pellet to fit the crucible for the e-beam evaporation system. A mixture of ZnS, MgS and MnS/Mn powder was expected to form ZnMgS:Mn after being sintered at 650°C in 5% H_2S/ 95% Ar ambient. The amount of MgS in solution of ZnS may be restricted by the solid solubility limits (Figure 2-9). Data in Chapter 2 showed this limit was 7% atomic MgS for ZnS in the wurtzite hexagonal phase, 7% to 24% atomic MgS for ZnS in zinc-blende cubic phase. Over 24% MgS substitution separates out MgS rocksalt cubic phase. In another word, maximum 24% ZnS can be substituted by MgS before MgS phase is separated. $Zn_{1-x}Mg_xS$:Mn source pellets were prepared at three different MgS substitution percentages x =0, 10 and 20% 20%. A solution of ZnMgS was expected upon sintering at a temperature of 850°C in 5% H_2S/ 95% Ar. However, Mg tends to oxidize at high temperatures. The $Zn_{0.8}Mg_{0.2}S$:Mn sources were therefore sintered at two different temperatures: 650°C and 850°C. The x-ray diffraction of the source annealed at the two different temperature are shown in Figure 6-1. The x-ray diffraction pattern from powder ZnS, MgS, metal Mn and a powder mixture of $Zn_{0.8}Mg_{0.2}S$:Mn before sintering are shown. Pure ZnS is zinc-blende cubic phase. As shown in Figure 6-1, after sintered at 650°C, ZnMgS-α phase was formed since the three characteristic wurtzite phase peaks at around 28° appeared. Further increasing sintering temperature up to 850°C, the three characteristic peaks were even stronger. However, the MgO phase was also formed since the major MgO peak at ~40° appeared after sintering.

Photoluminescence is generally weak from ZnS:Mn.[46] However, photoluminescence should be measured from ZnMgS:Mn using excitation by a He-Cd laser at 325nm (described in Chapter 3). The result is shown in Figure 6-2.

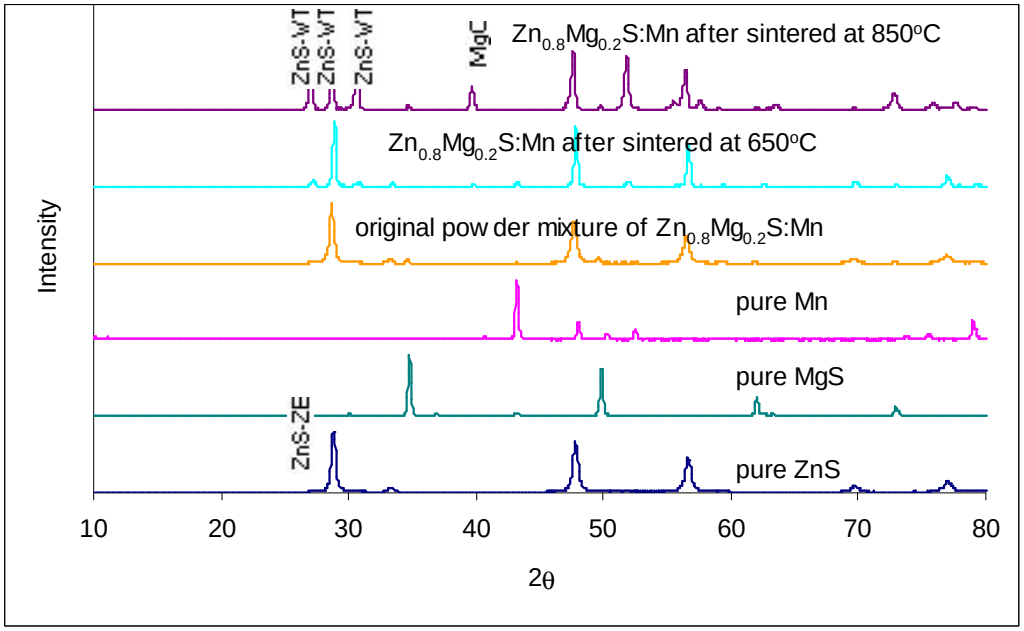

Figure 6-1 X-ray diffraction pattern of $Zn_{0.8}Mg_{0.2}S$:Mn pellet before and after sintering (ZB: zinc-blende and WT:wurtzite)

As expected, no PL was obtained from ZnS:Mn. After sintering at 850°C, both $Zn_{0.9}Mg_{0.1}S$:Mn and $Zn_{0.8}Mg_{0.2}S$:Mn demonstrated a large peak at ~590nm (orange color). The peak from $Zn_{0.8}Mg_{0.2}S$:Mn is slightly shifted to the lower wavelength region compared that from $Zn_{0.9}Mg_{0.1}S$:Mn. This observation is consistent with Mg substitution causing green shift. However, neither of the two ZnMgS:Mn sources demonstrated green PL emission, suggesting that ZnMgS:Mn solution weren't completely formed during sintering. Another peak was observed in the $Zn_{0.8}Mg_{0.2}S$:Mn PL spectrum at around 680nm as marked in Figure 6-2. This peak is probably from MgS:Mn which was reported

by the literature.[58] This is consistent with insufficient formation of ZnMgS compound during sintering.

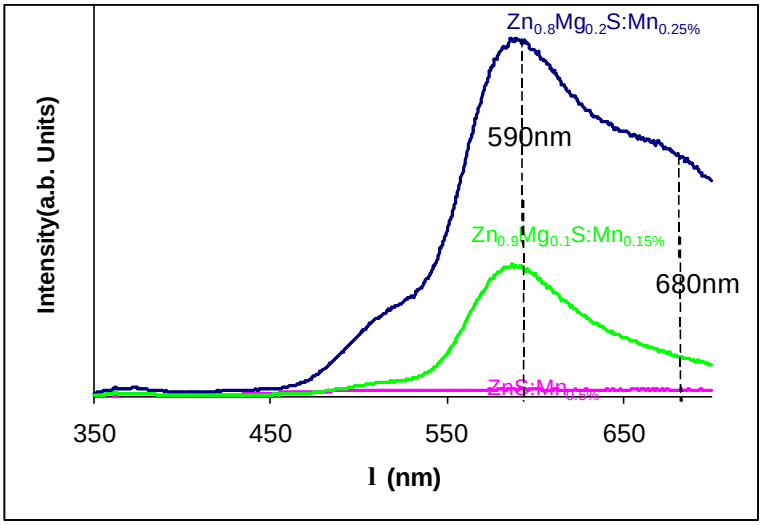

Figure 6-2 Photoluminescence of $Zn_{1-x}Mg_xS$:Mn source excited by a He-Cd laser source at 325nm

6.2.2 Mn^{2+} Doping

Noma et al.[43] used MnS as the doping source in the formation of ZnMgS:Mn. An optimum Mn concentration is necessary for a maximum EL brightness.[16] Too low a Mn concentration in the host material leads to too few Mn^{2+} luminescent centers while for too many Mn^{2+} luminescent centers, concentration quenching is observed. In concentration quenching, the physical distance between two Mn^{2+} ions is too close and the energy will be transferred between two Mn^{2+} ions until a non-radiation recombination center is encountered, no photon will be emitted and low luminescent intensity is observed.[16] Since generally the optimum Mn^{2+} concentration wouldn't be changed with Mg substitution,[43] the optimum MnS concentration [MnS] was determined for ZnS:Mn

by comparing the L-V curve of the ZnS:Mn_x films. As shown in Figure 6-3, a [MnS] concentration near 0.50 % resulted in the highest EL brightness.

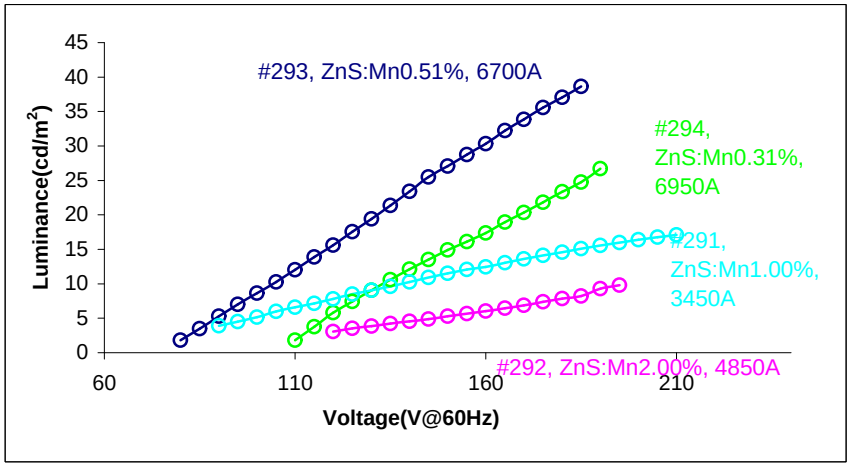

Figure 6-3 L-V curves for ZnS:Mn_x half-cell ACTFEL devices

While the optimum Mn^{2+} concentration in ZnMgS:Mn film is generally not changed with Mg substitution. Addition of MgS to the source pellet reduced the concentration required for optimum Mn in the ZnMgS:Mn film. The best electroluminescence of $Zn_{1-x}Mg_xS$:Mn at various Mg substitution (Mg 10% and 20%)were obtained and are shown in Figure 6-4. From Figure 6-4, Mg substitution reduced the EL brightness. The optimum source Mn concentration was decreased from 0.5% to 0.15% when the source Mg was increased from 0% to 20%.

6.2.3 Optimization of Mn in Evaporated ZnS:Mn

Metallic Mn doping was first optimized for evaporated ZnMgS:Mn ACTFEL devices. Electroluminescence of ZnS:Mn_x was obtained at metal Mn source doping concentrations from 0.13% to 4% atomic. As shown in Figure 6-5, metallic Mn doping at 1.00% in the source ZnS:Mn_x results in the best electroluminescence brightness. Mn

doping level in the source higher or lower than 1.00% reduced the electroluminescence brightness.

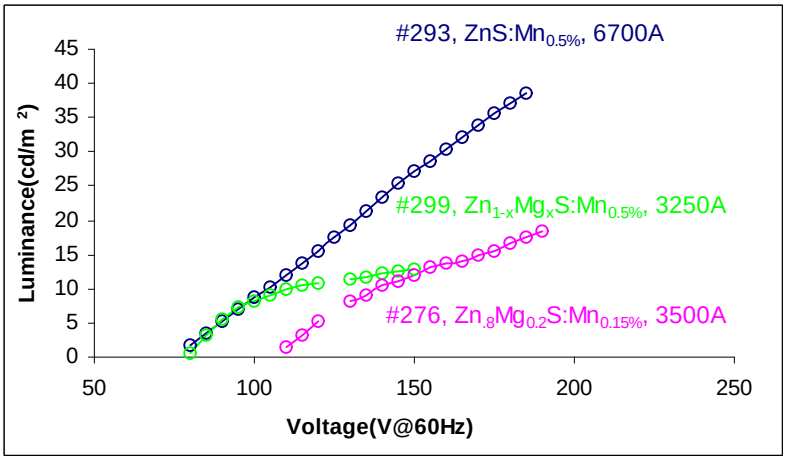

Figure 6-4 L-V curves of $Zn_{1-x}Mg_xS:Mn_y$ half cell EL devices vs. Mn concentration in the source pellet

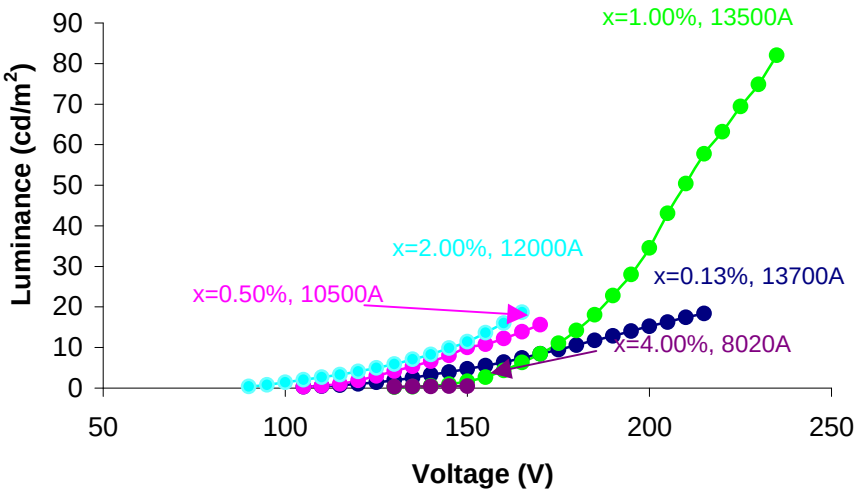

Figure 6-5 L-V curves of $ZnS:Mn_x$ for varying metal Mn source doping concentration in the source pellet

To determine the amount of Mn incorporated into the evaporated films, analysis by EDX and SIMS were considered. However the Mn concentration in the ZnS:Mn films was generally less than 1%, which is not detected by EDX. Therefore, SIMS was used

here to obtain the Mn doping profile and the absolute Mn concentration in ZnS films. The result is shown in Figure 6-6. The highest EL brightness was obtained at the optimum [Mn] of 0.12% in ZnS:Mn film. The highest EL brightness was obtained at a Mn concentration of 0.12% in ZnS:Mn films.

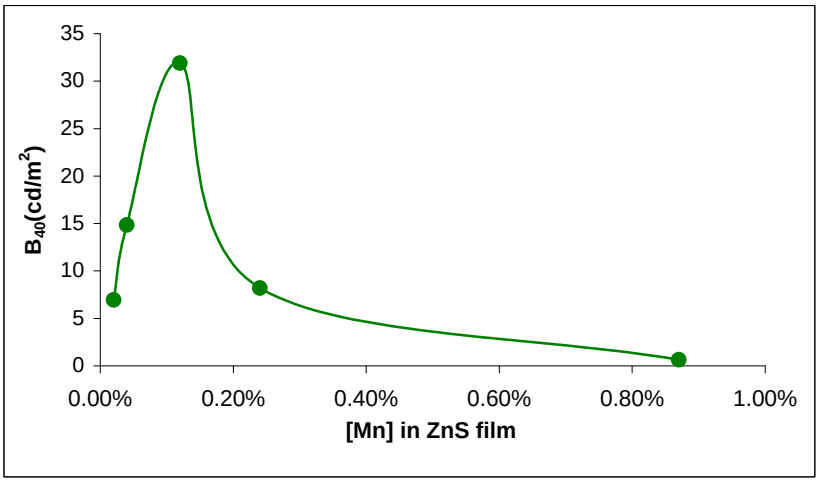

Figure 6-6 Brightness vs. Mn concentration curve in ZnS:Mn films resulted by SIMS

The optimum Mn concentration in film (0.12%) is much lower than the optimum Mn concentration in the source. After evaporation, a greenish MnS residue was observed in the crucible. Thus most of the MnS remained in the crucible and did not evaporate. This is consistent with the vapor pressure of MnS being less than that of ZnS.[36] The deviation of Mn concentration in the film from that in the source is plotted in Figure 6-7.

6.2.4 Rapid Thermal Annealing of ZnS:Mn

The crystallinity of ZnS:Mn films can be enhanced either by depositing at a high substrate temperature or annealing at high temperature after annealing.[12, 88] However, the

deposition rate of ZnS:Mn becomes zero when substrate temperature is over 250^{o}C due to high sulfur vapor pressure.[66]

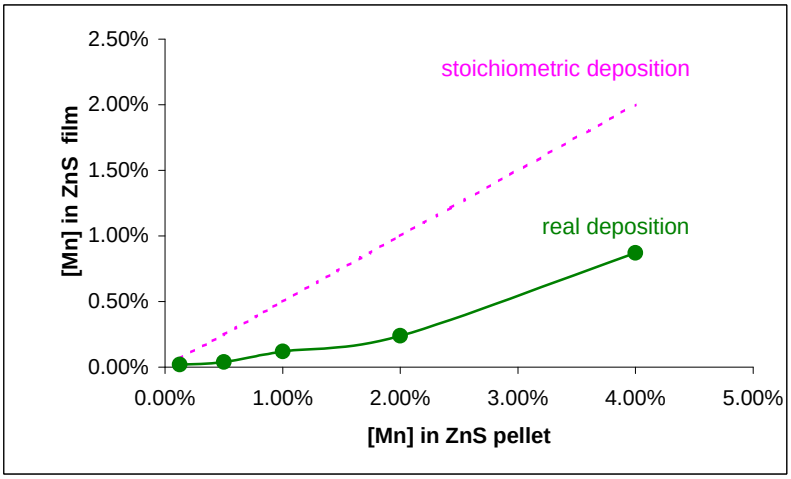

Figure 6-7 Deviation of [Mn] in ZnS film from [Mn] in source ZnS

Therefore a substrate temperature of 150^{o}C was used for the present ZnS:Mn film growth. Rapid thermal annealing at 650^{o}C in Ar for 5 minutes was used as a post deposition anneal to enhance crystallinity. As shown in Figure 6-8, the brightness and the slope of dL/dV increased upon annealing. After annealing the doped Mn was distributed more uniformly than before annealing. As shown in the SIMS profile before and after annealing at 650^{o}C in Ar for 5 min.s (Figure 6-9). As shown in Figure 6-9, before annealing the Mn doping was not distributed uniformly. However, after annealing Mn doping profile became flat, which indicates that Mn doping had diffused and re-distributed uniform except for 0<t<200s. The dip at the beginning of the profile will be discussed below, but it doesn't represent a dip in concentration.

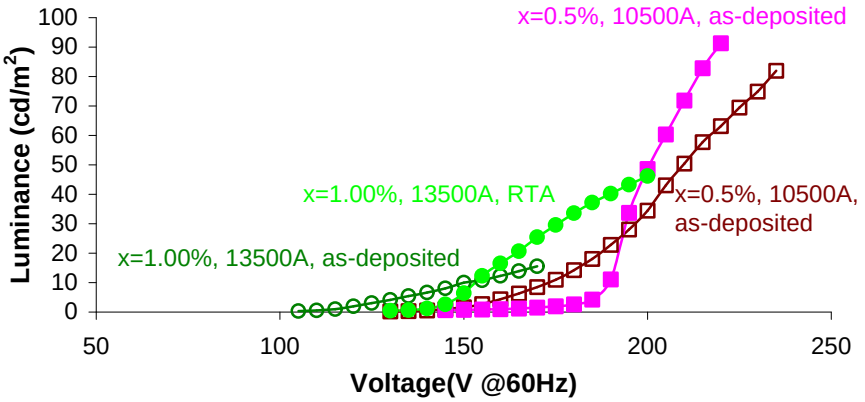

Figure 6-8 L-Vcurve of ZnS:Mn before and after rapid thermal annealing

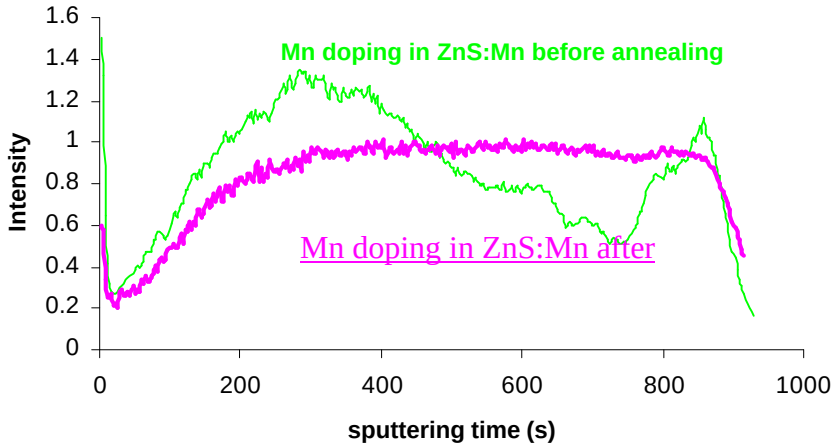

Figure 6-9 SIMS profile of Mn concentration in ZnS before and after rapid thermal annealing at 650^{o}C, 30 mins in Ar

Since the pellet composition changed during evaporation from accumulation of MnS, the composition of ZnS:Mn in film could have a gradient throughout the film depth. SIMS was used here to the study elemental profiles of the ZnS:Mn film. The results are given in Figure 6-10. The film was obtained from the pellet ZnS:MnS(1.00%). The Zn and S concentration was almost constant along the whole ZnS:Mn layer depth. But, the Mn

concentration was increased with the thickness depth, which means that the Mn concentration near the surface of the ZnS:Mn layer was higher than that near the bottom of the ZnS:Mn layer. As illustrated by data in Figure 6-4 to 6-6, the electroluminescence brightness of ZnS:Mn is strongly dependent on Mn concentration relative to ZnS, therefore non-uniform Mn concentrations lead to lower EL brightness.

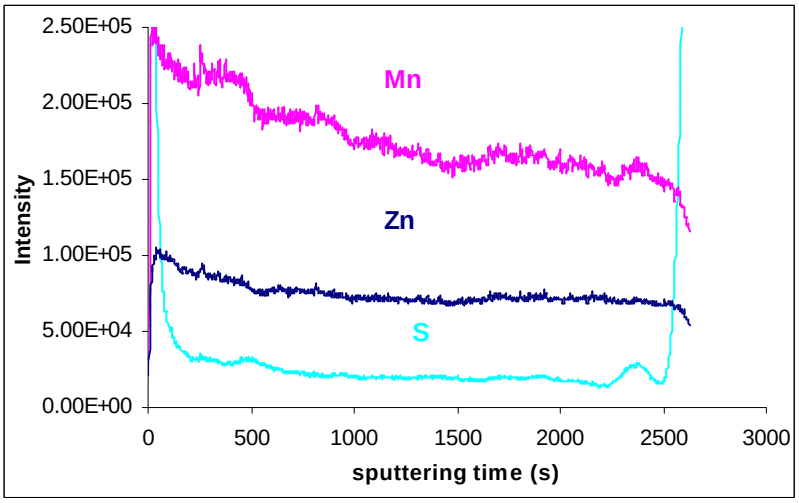

Figure 6-10 SIMS profile of E-beam evaporated ZnS:Mn film

6.2.5 Lattice Expansion of $Zn_{1-x}Mg_xS$:Mn

Evaporated ZnMgS:Mn is generally poorly crystallized because of the limited solubility of two different phases: rocksalt MgS and zinc-blende ZnS.[89] Maximum reported solubility of MgS in ZnS is 24%.[89] The Mg concentration in the film was generally much higher than that in the source which the film was evaporated from.[43] The highest Mg concentration addition to the $Zn_{1-x}Mg_xS$:Mn pellets was 20%. The crystallinity was getting poor when Mg substitution percentage was increased. The lattice constant was expected to increase with Mg substitution and the x-ray diffraction data from the $Zn_{1-x}Mg_xS$:Mn shown in Figure 6-11 support this fact. With increase of Mg in

the source powder, the ZnMgS peak at 28.5^{o} was shifted to the lower 2θ, consistent with a lattice parameter increase. Low peak intensity and large FWHM shown in Figure 6-11 indicates a poor crystallinity after Mg concentration is increased.

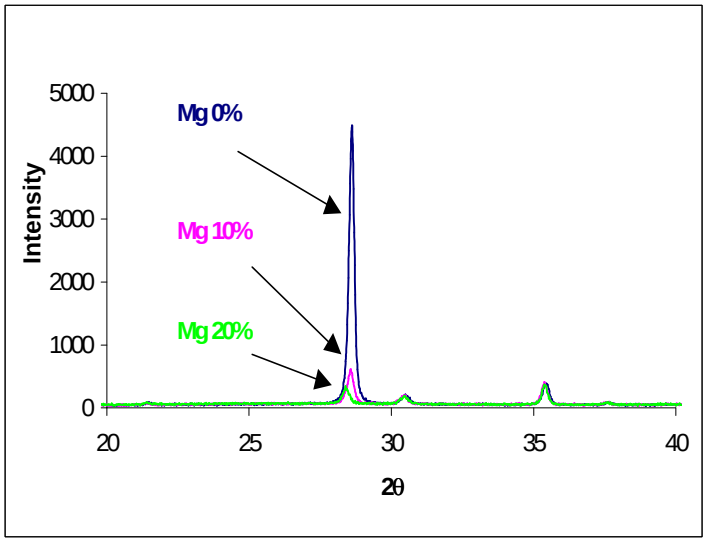

Figure 6-11 X-ray diffraction pattern of $Zn_{1-x}Mg_xS$:Mn at x= 0.00 and 0.10 and 0.20 based on mixture of powder before sintering of source pellet

6.2.6 Green Shift of $Zn_{1-x}Mg_xS$:Mn

Electroluminescence was obtained from $Zn_{1-x}Mg_xS$:Mn films with x= 0.00, 0.10 and 0.20 in the starting pellet and the CIE coordinates were also measured by the spectrometer and are listed along with brightness in Table 6-1. EL emission from both ZnS:Mn and $Zn_{0.9}Mg_{0.1}S$:Mn were in the orange color region according to the CIE chart (Figure 2-4). EL emission of $Zn_{0.8}Mg_{0.2}S$:Mn is shifted to the yellow-greenish region according to values x and y of 0.505 and 0.490 respectively.

6.2.7 Cross Section TEM

With the increase of the Mg substitution percentage, the crystallinity of $Zn_{1-x}Mg_xS$:Mn becomes poorer and the rocksalt MgS phase tends to separate out of the ZnMgS wurtzite phase. To determine if the MgS phase was segregated on the ZnMgS grain boundaries, cross-section TEM was used.

Table 6-1 CIE coordinates of $Zn_{1-x}Mg_xS$:Mn at x = 0.00, 0.10, and 0.20 for the concentration in the starting pellet

	[Mn] (at.)	sample	B40 (cd/cm^2)	V (V)	thickness (Å)	x	y
ZnS:Mn	0.50%	#293	10.24	105	6950	0.5451	0.4529
$Zn_{0.9}Mg_{0.1}S$:Mn	0.25%	#299	10.85	120	3250	0.5460	0.4510
$Zn_{0.8}Mg_{0.2}S$:Mn	0.15%	#276	10.98	145	3500	0.5049	0.4900

The XTEM bright field image in Figure 6-12 was taken at 50K magnification. This ZnMgS:Mn film was evaporated from the pellet $Zn_{0.8}Mg_{0.2}S:Mn_{0.15\%}$. The film was in-situ annealed in vacuum ($5*10^{-6}$Torr) at 550°C for 30 mins. The film was deposited on glass/ATO/ITO to form an EL device as shown by the layers in cross section. The top Al dot contact is not seen in this image. The thickness of the different layers in this device are identified. The ITO layer is around 2500Å, the ATO is 1000Å and the ZnMgS:Mn layer is 3500Å. The columnar ZnMgS crystallites are observed in the XTEM image at a magnification of 150K in Figure 6-13. The ZnMgS columnar grains all are oriented in the same direction, consistent with the XRD data which show the strongest ZnMgS peak at 28° , which is associated with the cubic (111) and overlaps the hexagonal (0001). The

columnar grain diameters range from 0.5μm to 1.5μm. No MgS phase can be seen in this TEM image.

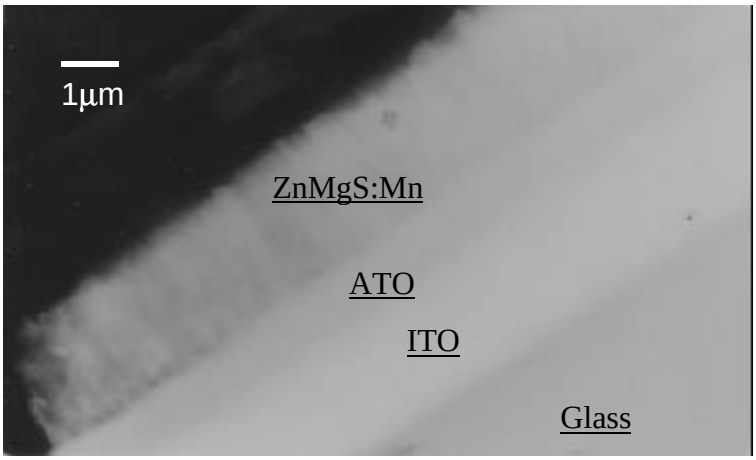

Figure 6-12 XTEM bright field image of $Zn_{0.8}Mg_{0.2}S$:Mn ACTFEL device on glass/ITO/ATO

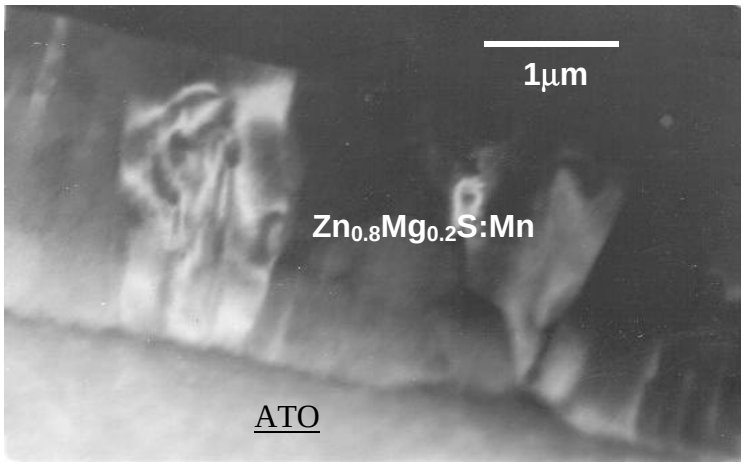

Figure 6-13 XTEM of $Zn_{0.8}Mg_{0.2}S$:Mn ACTFEL device on glass/ITO/ATO after annealed at 550^{o}C in 6*10^{-6} Torr vacuum for 30mins.

Selected Area Diffraction (SAD) and microdiffraction image were used to attempt to identify any MgS phase. Placing an aperture at the focus plane of the object lens, the diffraction pattern image can be obtained from the selected area of the specimen. When

the area of interest is smaller than the smallest aperture, the only possible way to obtain diffraction from this area is to reduce the beam size. When the beam size is reduced, the electron beam is not parallel as a diffraction pattern is required. The diffraction pattern spots will diffuse out to be a large spots. The SAD and microdiffraction of ZnMgS phase was obtained and are shown in Figure 6-14,

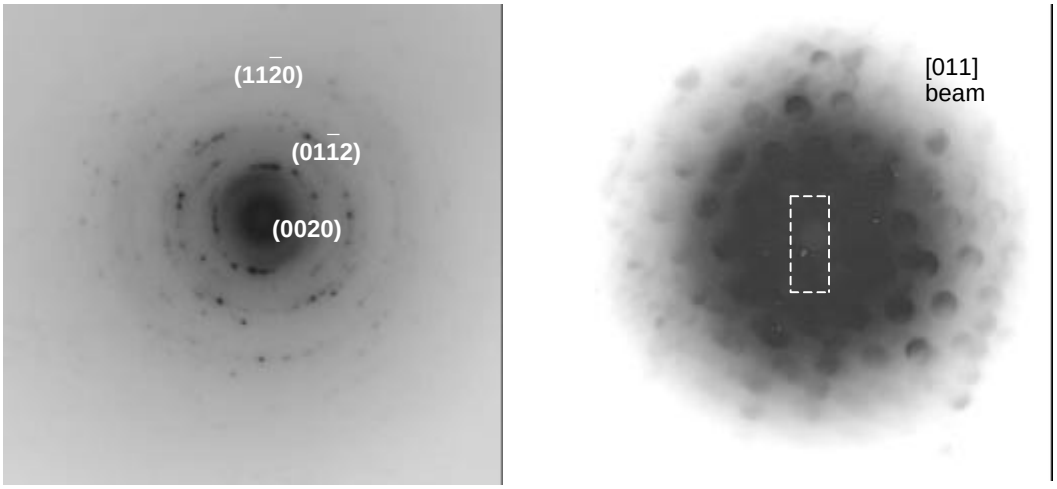

a) b)

Figure 6-14 TEM a) SAD image and b) microdiffraction image of hexagonal ZnMgS structure

As shown in Figure 6-14, the ZnMgS layer was polycrystalline as indicated the partial rings instead of the individual dots. The dots on the same circle represent the same crystal planes oriented in different directions, as well as diffraction spots from multiple grains. The distance of each of the dots from the beam center is governed by the following equation:

$$Rd = \boldsymbol{l}L \qquad (6\text{-}1)$$

where *R* stands for the distance of each dot from the beam center, *d* is the spacing of a given crystal plane, ***l*** is the wavelength of electron after the relativitistic factor is considered, L is the camera length. The camera length used for this image was 82cm. The electron acceleration voltage was 200KV. The crystal plane spacing d is given by

$$d = \frac{1}{\sqrt{(h/a)^2 + (k/b)^2 + (l/c)^2}} \qquad (6\text{-}2)$$

in which a, b and c are the lattice constants. It is found that the three circles closest to the beam center in the SAD image were from the ZnMgS hexagonal structure, (1120), (0112), (0020) are labeled in Figure 6-15. The microdiffraction image shows a two-fold symmetry. This further indicates that diffraction is from two-fold ZnMgS hexagonal rather than four-fold MgS cubic structures. The SAD and microdiffraction patterns from the MgS phase were also obtained and are shown in Figure 6-15. As shown, the circles in the SAD image match the three MgS crystal planes (002), (111) and (220). In addition, the microdiffraction image is four-fold symmetry which further supports that the diffraction is from MgS rocksalt cubic structure.

6.3 Summary and Discussions

6.3.1 $Zn_{1-x}Mg_xS$:Mn Source

After sintered at 850^{o}C, the $Zn_{1-x}Mg_xS$:Mn source wurtzite phase was formed. However, magnesium oxidation was observed. The photoluminescence spectra of the $Zn_{1-x}Mg_xS$:Mn (x=0.10 and 0.20) showed a big peak 590nm which is most likely from ZnS:Mn and a peak 680nm which is probably from MgS:Mn. This implies that the Zn_{1-}

$_xMg_xS$:Mn source was more like the separate ZnS:Mn and MgS:Mn instead of $Zn_{1-x}Mg_xS$:Mn.

6.3.2 Optimum Mn Doping

Two doping sources MnS and metal Mn were used. According to the EL performance of the ZnS:Mn films from the two doping sources, either of the doping sources (MnS or metal Mn) didn't make much difference in the EL performance.

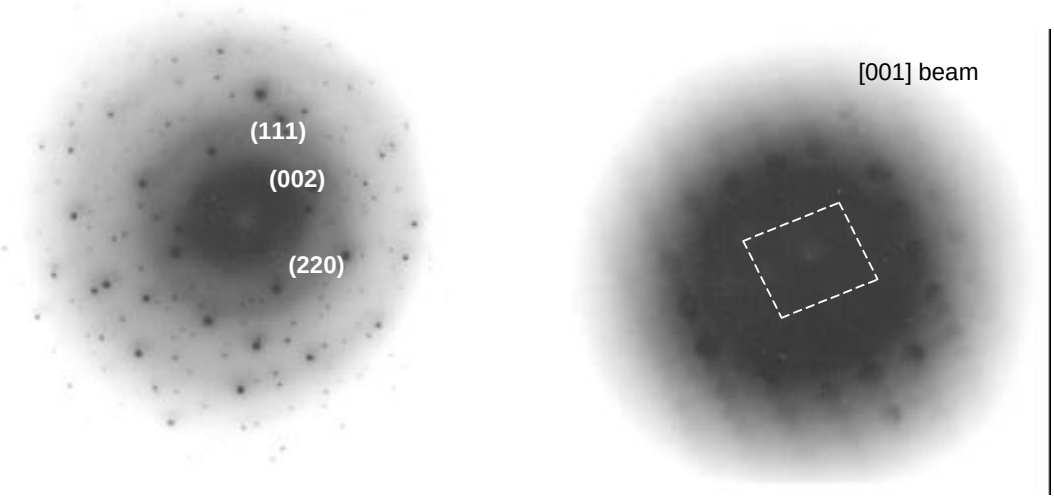

a) b)

Figure 6-15 The TEM a) SAD image and b) the microdiffraction image of cubic MgS phase

The optimum Mn concentration in source from metal Mn (0.5%) was higher than that from MnS concentration (1.5%). Metal Mn probably tends to be sulfidized into MnS during evaporation and remained in the crucible. The evidence was that the greenish MnS was observed after evaporation.

The optimum Mn concentration in film was much lower than the optimum Mn concentration in source. The same reason is that some of the Mn doping became MnS residue during evaporation and left in the crucible.

According to the literature reports of Noma et al,[43] the optimum Mn concentration in ZnMgS:Mn films was not generally changed with Mg substitution percentage. However, the optimum Mn concentration in source was dependent on Mn substitution percentage for Zn. The more Mg was substituted for Zn, the less Mn doping was required in source. The best EL performance for ZnS:Mn and $Zn_{0.9}Mg_{0.1}S$:Mn was obtained at Mn concentration at 0.5% in source, while the best EL performance for $Zn_{0.8}Mg_{0.2}S$:Mn was obtained at Mn concentration at 0.15%.

Although the Mn concentration in source is dependent on many factors such as Mg substitution percentage, substrate temperature and deposition rate, the optimum Mn concentration in ZnS:Mn and ZnMgS:Mn remains constant.[43] In order to obtain this optimum Mn concentration in film, the SIMS technique and the Mn reference in ZnS matrix were used. The optimum Mn in films was 0.12%. It was lower than the optimum concentration in source.

6.3.3 Rapid Thermal Annealing

Rapid thermal annealing at 650^{o}C for 30 minutes dramatically improved EL brightness and L-V slope sharpness. The improved crystallinity after RTA is probably responsible for the enhanced EL performance. Another factor responsible for this is the Mn doping distribution. The SIMS data found that the Mn doping profile was not uniform before RTA, while it became uniform after RTA.

6.3.4 Characteristics of $Zn_{1-x}Mg_xS$:Mn Films

The x-ray diffraction of the $Zn_{1-x}Mg_xS$:Mn films at varied x show that the lattice constant of the $Zn_{1-x}Mg_xS$:Mn was increased with increase of Mg substitution. This observation is consistent with the results reported by Noma et al[43] and the yellow-greenish EL emission was observed in the ZnMgS:Mn films evaporated from the source $Zn_{0.8}Mg_{0.2}S$:Mn. Compared with the films, the $Zn_{1-x}Mg_xS$:Mn source didn't show any visible PL green shift.

6.3.5 MgS phase Segregation

According to the ZnS-MgS equilibrium diagram, MgS substitution over 24% for ZnS will result in MgS segregation. The XTEM was used to identify the microstructure of ZnMgS:Mn films. The cross section TEM bright field images give the information that the ZnMgS:Mn film evaporated from $Zn_{0.8}Mg_{0.2}S$:Mn was columnar crysatllites oriented in the film plane normal. The ZnMgS phase and MgS phase were identified by examining the SAD diffraction patterns. Both ZnMgS phase and MgS phase structure were observed in the SAD diffraction patterns. Further evidence was given by microdiffraction patterns which give the information about the crystal structure symmetry. The ZnMgS wurtzite is 2-fold symmetry and the MgS phase is 4-fold symmetry. The 2-fold symmetry was observed in the microdiffraction pattern. The segregation of MgS from ZnMgS:Mn was observed, but whether it was located at ZnMgS:Mn crystal boundaries was not further investigated.

CHAPTER 7
CONCLUSIONS

7.1PulsedLlaser Deposited (PLD) Zn_2GeO_4:Mn

The Zn_2GeO_4:Mn ACTFEL devices fabricated by pulsed laser deposition were the first successfully achieved by this deposition technique. The growth parameters and annealing parameters of Zn_2GeO_4:Mn deposited on both PZT substrates and glass/ITO/ATO were investigated and the optical performance of Zn_2GeO_4:Mn (photoluminescence and electroluminescence) were studied. Structural, chemical and electrical characteristics were measured to further understand the behavior of Zn_2GeO_4:Mn optical performance. The following conclusion are the result,

1. The highest EL brightness of the Zn_2GeO_4:Mn ACTFEL devices was 450cd/m^2. This was a half cell Zn_2GeO_4:Mn EL device deposited on PZT (device structure Al_2O_3substrate/Au(2000Å)/Pb(ZrTi)O_3(20μm)/ Zn_2GeO_4:Mn(6800Å)/ITO(2000Å), measured with a 2.5kHz trapezoidal voltage waveform (5μs rise, 30μs stay and 5μs drop time).
2. The Zn_2GeO_4:Mn source target had a rhombohedral polycrystalline structure after being sintered at 1150^{o}C and it demonstrated green PL emission at 540nm.
3. Zn_2GeO_4:Mn films grown by pulsed laser deposition demonstrated green PL and EL emission at 540nm.
4. Zn_2GeO_4:Mn films deposited on Si at 250^{o}C (then annealed at 800^{o}C) demonstrated a much higher photoluminescence than those deposited at 800^{o}C. This was

hypothesized to be due to higher deposition rate resulting in a larger thickness and due to the long annealing time which resulted in a rougher film.

5. Zn_2GeO_4:Mn ACTFEL devices on a PZT substrate showed a much higher brightness and large dL/dV slope than those from films deposited on glass/ITO/ATO due to longer annealing time which resulted in better crystallinity, and the larger dielectric thickness which allows a higher voltage across the dielectric layer.
6. Higher laser energy density pulses during pulsed laser deposition of Zn_2GeO_4:Mn resulted in a larger film thickness due to a higher deposition rate, but resulted in a reduced film grain size.
7. The enhanced EL brightness of Zn_2GeO_4:Mn film on PZT annealed at 750^oC for 2.5 hrs., compared with the film annealed at 770^oC for 10 mins, was the result of the longer annealing time and lower annealing temperature. This longer annealing time resulted in a better crystallinity, rougher surface and less defects. The lower temperature minimized the reaction of the Zn_2GeO_4:Mn and the PZT.
8. The Zn_2GeO_4:Mn film deposited on Si at 250^oC (annealed at 800^oC) demonstrated the highest PL. The Zn_2GeO_4:Mn deposited at lower temperature (RT) (annealed at 800^oC) demonstrated no PL due to poorer re-growth during annealing. The Zn_2GeO_4:Mn deposited at higher temperature (800^oC) demonstrated a reduced PL due to a lower deposition rate, which resulted in a smaller film thickness.
9. The Zn_2GeO_4:Mn grown by pulsed laser deposition was non-stoichiometric (Zn-deficient) based on the EDX result and stoichiometric based on the XRD results. The Zn-deficiency was independent of substrate temperature (from 250^oC to 800^oC).

7.2 RF Sputter Deposited (SD) Zn_2GeO_4:Mn

Zn_2GeO_4:Mn was sputter deposited on PZT or glass/ITO/ATO substrates using RF sputtering deposition. Both deposition and annealing parameters were varied for Zn_2GeO_4:Mn.

1. The highest brightness of Zn_2GeO_4:Mn ACTFEL devices (Al_2O_3/Au/PZT/Zn_2GeO_4:Mn(13000Å)/ITO) was 120cd/m^2 at 2.5Khz trapezoidal voltage waveform.
2. The Zn_2GeO_4:Mn grown by sputter deposition demonstrated PL and EL emission at 540nm.
3. The photoluminescence of Zn_2GeO_4:Mn grown by RF sputter deposition was independent of major sputtering deposition parameters, including vacuum pressure ($5x10^{-5}$~$5x10^{6}$Torr) , ambient O_2/Ar ratio (0/100 to 50/50) and working pressure (7.3~25 mTorr). The photoluminescence brightness of Zn_2GeO_4:Mn deposited on PZT increased linearly with the film thickness and the dead-layer thickness value of 1250Å was determined.
4. Zn_2GeO_4:Mn films deposited on PZT and annealed at 700^{o}C for 3.5 hrs demonstrated a much higher PL and EL than that annealed at 800^{o}C for 20 mins. The substantial reaction of Zn_2GeO_4:Mn with PZT at 800^{o}C was responsible for the reduced optical performance. Longer annealing time at 700^{o}C (up to 10hrs.) increased PL intensity.
5. Zn_2GeO_4:Mn films grown by RF sputtering deposition were Zn-deficient based on the EDX results, while the XPS results indicated that Ge containing materials exists in the Zn_2GeO_4:Mn, which could be GeO_2.
6. EL brightness was extremely poor when the thickness was reduced to 5000Å. A model of non-continuous Zn_2GeO_4:Mn film on PZT was used to explain this

observation. Due to the non-continuous Zn_2GeO_4:Mn film on PZT, the majority of the voltage was dropped through the PZT rather than the Zn_2GeO_4:Mn.

7.3 Comparison of PLD and SD Zn_2GeO_4:Mn

Comparing the two deposition techniques for Zn_2GeO_4:Mn growth of Zn_2GeO_4:Mn on $Pb(ZrTi)O_3$, Zn_2GeO_4:Mn grown by pulsed laser deposition demonstrated a much better electroluminescence than that grown by sputter deposition, mainly due to a higher substrate temperature (PLD 250^{o}C and SD at R.T.) and a high atom energy for better surface mobility in the case of PLD.

7.4 Electron-beam Evaporated $Zn_{1-x}Mg_xS$:Mn

$Zn_{1-x}Mg_xS$:Mn ACTFEL devices deposited on glass/ITO/ATO by electron beam evaporation were investigated.

1. Greenish electroluminescent emission was obtained in the film evaporated from a $ZnS_{0.2}$:$MgS_{0.2}$:Mn source.
2. ZnMgS:Mn films evaporated from a MnS doped source demonstrated a higher electroluminescence than those evaporated from a metal Mn doped source.
3. An optimum Mn doping of 0.12% atomic was determined in films using SIMS analysis.
4. Thermal annealing at 650^{o}C for 30mins in Ar dramatically increased the EL brightness and the dL/dV slope compared with the as-deposited films.

5. Columnar ZnMgS crystallites were observed in ZnS0.8:MgS0.2:Mn using XTEM. MgS phase segregation was identified using TEM selected area diffraction and microdiffraction.

LIST OF REFERENCES

1. P. D. Rack and P. H. Holloway, Materials Science & Engineering **R21,** p171-219 (1998).

2. R. E. Hummel, Electronic Properties of Materials, Springer Verlag, ISBN: 038795144X (December, 2000).

3. R. Mach and G. O. Muller, J. Cryst. Growth (Netherlands), Journal of Crystal Growth **101,** 967-75 (1990).

4. P. H. Holloway, J. Sebastian, T. Trottier, S. Jones, H. Swart, R. O. Petersen, H. M. K., J. Kanicki, C. J. Summers, and F. Funada, Flat Panel Display Materials II. Symposium**,** xiii+513, 425-31 (1997).

5. H. Hori, Oyo Buturi **68,** 435-41 (1999).

6. H. Uchiike, S. Shionoya, and H. Kobayashi, Electroluminescence. Proceedings of the Fourth International Workshop**,** xv+396, 238-45 (1989).

7. M. Grundmann, Physica E **5,** 167-84 (1999).

8. L. J. Rothberg and A. J. Lovinger, Journal of Materials Research **11,** 3174-87 (1996).

9. J. Ghrayeb, T. W. Jackson, R. Daniels, and D. G. Hopper, Proc. SPIE - Int. Soc. Opt. Eng. (USA), Proceedings of the SPIE - The International Society for Optical Engineering, **3057,** 237-48 (1997).

10. C. N. King, J. Soc. Inf. Disp. (USA), Journal of the Society for Information Display **4,** 153-6 (1996).

11. S. Naka, M. Shibata, H. Onnagawa, and K. Miyashita, Transactions of the Institute of Electronics, Information and Communication Engineers C-II **J76C-II,** 159-61 (1993).

12. K. E. Waldrip, J. S. Lewis, Q. Zhai, M. Davidson, and P. H. Holloway, Applied Physics Letters **76,** 1276-8 (2000).

13. K. Bhattacharyya, S. M. Goodnick, and J. F. Wager, Journal of Applied Physics **73,** 3390-5 (1993).

14. K. Brennan, Journal of Applied Physics **64,** 4024-30 (1988).

15. P. A. Keller, Information Display **12,** 18-22 (1996).

16. Y. A. Ono, Electroluminescent Displays, World Scientific Pub Co; ISBN: 9810219210 (June, 1995).

17. C. N. King, G. N. Parsons, C. C. Tsai, T. S. Fahlen, and C. H. Seager, Flat-Panel Display Materials - 1998. Symposium**,** xi+342, 247-58 (1998).

18. D. H. Smith, J. Lumin. (Netherlands), Journal of Luminescence **23,** 209-35 (1981).

19. S. Matsumoto, Electronic Display Devices, John Wiley & Sons, ISBN: 0471922188 (April 1990).

20. E. Bringuier, Journal of Applied Physics **75,** 4291-312 (1994).

21. B. A. Baukol, J. C. Hitt, P. D. Keir, and J. F. Wager, Applied Physics Letters **76,** 185-7 (2000).

22. S. Kobayashi, J. F. Wager, A. E. S. V. P. Abu-Dayah, and J. C. McClure, Electroluminescence. Proceedings of the Sixth International Workshop**,** xi+422, 234-9 (1992).

23. M. Dur, S. M. Goodnick, S. S. Pennathur, J. F. Wager, M. Reigrotzki, and R. Redmer, Journal of Applied Physics **83,** 3176-85 (1998).

24. E. Bringuier and K. Bhattacharyyal, Semiconductor Science and Technology **10,** 1065-75 (1995).

25. T. D. Thompson and J. W. Allen, Journal of Physics C (Solid State Physics) **20,** L499-503 (1987).

26. E. Bringuier, Journal of Applied Physics **70,** 4505-12 (1991).

27. E. Bringuier, Journal of Applied Physics **67,** 7040-4 (1990).

28. G. Blasse and B. C. Grabmaier, Luminescent Materials Springer Verlag; ISBN: 0387580190 (September 1994).

29. P. H. Holloway, S. Jones, T. Trottier, and Sebastian, Eleventh International Vacuum Microelectronics (1998).

30. P. D. Keir, Ph. D. Dissertation, Electrical and Computer Engineering, Oregon State University (1999).

31. L. Duan, T. Xiao, and A. H. E. M. J. Kitai, Conference Record of the 1997 International Display Research Conference and International Workshops on LCD Technology and Emissive Technology**,** xvi+679, 358-61 (1997).

32. F. O. Adurodija, H. Izumi, T. Ishihara, H. Yoshioka, H. Matsui, and M. Motoyama, Applied Physics Letters **74,** 3059-61 (1999).

33. T. Minami, Luminescent Materials. Symposium p. xi+368**,** 47-58 (1999).

34. E. Bringuier, Journal of Applied Physics **66,** 1314-25 (1989).

35. Planar American Inc. website: www.planar.com, (March 2001).

36. D. R. Lide, Handbook of Chemistry and Physics, 81st Edition, CRC Press (June 6, 2000).

37. H. Kobayashi and S. Tanaka, J. Soc. Inf. Disp. (USA), Journal of the Society for Information Display **4,** 157-64 (1996).

38. R. H. Mauch, Journal of the Society for Information Display **5,** 173-8 (1997).

39. S. M. Sze, Physics of Semiconductor Devices, John Wiley & Sons, ISBN: 0471056618 ; (September 1981).

40. T. Minami, Flat Panel Displays and Sensors Principles, Materials (2000).

41. L. Tannas, Flat Panel Displays and CRT's, Van Nostrand Reinhold, New York (1985).

42. T. Minami, Flat Panel Displays and Sensors Principles, Materials and Processes. Symposium **558,** 29-40 (2000).

43. M. Noma, K. Tanaka, A. Mikami, and M. Yoshida, Journal of Applied Physics **84,** 6321-6 (1998).

44. L. Binet, D. Gourier, and C. Minot, Journal of Solid State Chemistry **113,** 420-33 (1994).

45. S. H. M. Poort, D. Cetin, A. Meijerink, and G. Blasse, Journal of the Electrochemical Society **144,** 2179-83 (1997).

46. J. S. Lewis, Ph.D. dissertation, Department of Materials Science and Engineering, University of Florida (2000).

47. T. Minami, Y. Kuroi, H. Yamada, and S. Takata, J. Soc. Inf. Disp. **6,** 17-22 (1998).

48. L. Yong Eui, D. P. Norton, J. D. Budai, C. M. Rouleau, and P. Jae-Won, J. Electroceram. (Netherlands), Journal of Electroceramics **4,** 293-7 (2000).

49. R. K. Singh and D. Kumar, Materials Science & Engineering R (Materials Research Society): Reports **R22,** 113-85 (1998).

50. K. G. Cho, D. Kumar, D. G. Lee, S. L. Jones, P. H. Holloway, and R. K. Singh, Applied Physics Letters **71,** 3335-7 (1997).

51. R. K. Singh and J. Narayan, Physical Review B (Condensed Matter) **41,** 8843-59 (1990).

52. S. L. Jones, D. Kumar, K. G. Cho, R. Singh, and P. H. Holloway, Displays **19,** 151-67 (1999).

53. K. G. Cho, D. Kumar, D. G. Lee, P. H. Holloway, R. K. Singh, G. N. Parsons, C. C. Tsai, T. S. Fahlen, and C. H. Seager, Flat-Panel Display Materials - 1998. Symposium**,** xi+342, 301-6 (1998).

54. D. B. Chrisey and G. K. Hubler, Pulsed Laser Deposition of Thin Films, John Wiley & Sons; ISBN: 0471592188 ; (June 7, 1994).

55. V. Sallet, A. Lusson, M. Rommeluere, and O. Gorochov, Journal of Crystal Growth **220,** 209-15 (2000).

56. K. Ichino, K. Ueyama, H. Kariya, N. Suzuki, M. Kitagawa, and H. Kobayashi, Applied Physics Letters **74,** 3486-8 (1999).

57. K. Ichino, K. Ueyama, M. Yamamoto, H. Kariya, H. Miyata, H. Misasa, M. Kitagawa, and H. Kobayashi, Journal of Applied Physics **87,** 1-3 (2000).

58. R. Inoue, M. Kitagawa, T. Nishigaki, K. Ichino, H. Kobayashi, M. Ohishi, and H. Saito, J. Cryst. Growth **184,** 1076-80 (1998).

59. H. Kimijima, M. Kitagawa, R. Inoue, N. Shiraishi, N. Hoashi, K. Ichino, and H. Kobayashi, Appl. Surf. Sci. **113,** 432-5 (1997).

60. T. A. O'Brien, P. D. Rack, P. H. Holloway, and Zerner, Journal of Luminescence **78,** 245-57 (1998).

61. T. Minami, Y. Kuroi, and S. Takata, J. Soc. Inf. Disp. **4,** 299-303 (1996).

62. T. Minami, Y. Kubota, and T. Miyata, Proceedings of the 18th. International Display Research Conference. Asia Display '98**,** p. xi+1194, 81-4 (1998).

63. www.alfa.com, Alfa Aesar , A Johnson Matthay Company (March, 2001)

64. J. F. O'Hanlon, A User's Guide to Vacuum Technology, 2nd Edition, John Wiley & Sons; ISBN: 0471812420 (April 24, 1989).

65. J. M. Lafferty, Foundations of Vacuum Science and Technology, John Wiley & Sons; ISBN: 0471175935 (January 1998).

66. T. N. Chin, O. B. O'Neill, and P. E. Houser, Appl. Surf. Sci. (Netherlands), Applications of Surface Science, **11-12,** 553-62 (1982).

67. T. Minami, T. Yamamoto, Y. Toda, and T. Miyata, Thin Solid Films (Switzerland), Thin Solid Films **373,** 189-94 (2000).

68. K. Donghwan, H. Younggun, C. Jun-Sik, and K. Seok-Keun, Thin Solid Films (Switzerland), Thin Solid Films, **377-378,** 81-6 (2000).

69. T. Minami, T. Miyata, and Y. Sakagami, Surf. Coat. Technol. **108,** 1-3 (1998).

70. P. D. Keir and J. F. Wager, 1996 SID International Symposium. Digest of Technical Papers. First Edition**,** xx+1022, 305-8 (1996).

71. J. P. Bender and J. F. Wager, IEEE Transactions on Electron Devices **47,** 1113-15 (2000).

72. V. Bondar, Mater. Sci. Eng. B, Solid-State Mater. Adv. Technol. (Switzerland), Materials Science & Engineering B (Solid-State Materials for Advanced Technology), **B69-70,** 510-13 (2000).

73. B. Soenen, K. Neyts, G. Stuyven, and P. De Visschere, 1998 SID International Symposium. Digest of Technical Papers. Vol. 29**,** xxiv+1269, 655-8 (1998).

74. K. Ohmi, K. Ishitani, Y. Kashio, S. Tanaka, and H. Kobayashi, J. Soc. Inf. Disp. (USA), Journal of the Society for Information Display **5,** 145-9 (1997).

75. S. Wilson, C. R. Brundle, and C. Evans, Encyclopedia of Materials Characterization: Surfaces, Interfaces, Thin Films, Butterworth-Heinemann; ISBN: 0750691689.

76. J. W. Edington, The operation and calibration of the electron microscope, ASIN: 0333181336.

77. L. Yong Eui, C. M. Rouleau, C. Park, D. P. E. M. J. Norton, B. Di Bartolo, and K. Mishra, Luminescent Materials. Symposium**,** xi+368, 59-64 (1999).

78. S. A. Campbell, The Science and Engineering of Microelectronic Fabrication, Oxford University Press, ISBN 0-19-510508-7 (1996).

79. L. Yong Eui, D. P. Norton, and J. D. Budai, Applied Physics Letters **74,** 3155-7 (1999).

80. L. Yong Eui, C. M. Rouleau, C. Park, D. P. Norton, J. McKittrick, B. Bartolo, and K. Mishra, Luminescent Materials. Symposium**,** xi+368, 59-64 (1999).

81. D. L. Smith, Thin Film Deposition : Principles and Practice, McGraw Hill Text, ISBN: 0070585024 (May 1994).

82. I. A. Bondar, Izvestiya Akademii Nauk SSSR, Neorganicheskie Materialy **15,** 1008-13 (1979).

83. K. G. Cho, D. Kumar, P. H. Holloway, R. K. Singh, D. H. Lowndes, D. B. Chrisey, E. Fogarassy, and J. Narayan, Advances in Laser Ablation of Materials. Symposium**,** xi+431, 317-22 (1998).

84. J. D. Britton, J. C. McClure, and V. P. Singh, Electroluminescence. Proceedings of the Sixth International Workshop**,** xi+422, 286-91 (1992).

85. L. Yun-Hi, K. Young-Sik, J. Byeong-Kwon, and O. Myung-Hwan, IEEE Transactions on Electron Devices **46,** 892-6 (1999).

86. U. Troppenz, T. K. Plant, B. Huttl, K. O. Velthaus, and R. H. Mauch, J. Soc. Inf. Disp. (USA), Journal of the Society for Information Display **4,** 293-7 (1996).

87. Y. S. Kim, Y. H. Lee, B. K. Ju, M. H. Oh, M. Y. Sung, and D. K. Shin, 1998 SID International Symposium. Digest of Technical Papers. Vol. 29**,** xxiv+1269, 659-62 (1998).

88. Z. Qing, L. Jinghong, J. Lewis, K. Waldrip, P. H. Holloway, J. McKittrick, B. Di Bartolo, and K. Mishra, Luminescent Materials. Symposium**,** xi+368, 21-6 (1999).

89. J. W. Brightwell, B. Ray, and S. White, Journal of Materials Science Letters **3,** 951-4 (1984).

BIOGRAPHICAL SKETCH

Tao Feng was born in Chengdu, P. R. China. She grew up and was educated in her hometown. She entered the University of Electronic Science and Technology of China (UESTC) in 1985 to study materials science and engineering with a specialty of magnetic materials and devices. The research project for her bachelor's degree was wet-deposition of Ba-ferrite magnetic powder using NaCl fluxing. She obtained her bachelor degree of science in 1989. She continued at UESTC and obtained her master's degree in engineering in 1992. The research area for her master's degree was magneto-resistive NiFe/NiCo thin film growth and magnetic sensor development. After graduation from UESTC, she was hired by the Physics Institute of Southwestern China as a research scientist to investigate wet epitaxy of InAs for infra-red application. Six months later, she moved to Shenzhen and started a 4-year working experience in CASTIC-SMP Corp., Ltd. as a senior engineer and general manager assistant. In 1996, she was offered an assistantship by Dr. J. R. Childress at the University of Florida to pursue her Ph.D. in Materials Science and Engineering with a specialty of electronic materials. Her research area at Dr. Childress's group was giant magneto-resistive thin film growth and characterization, and magnetic thin film growth used for non-volatile magnetic random memory. She obtained her Master degree of Science in 1998. In the summer of 1998, her research interest was switched to growth and characterization of thin film electroluminescent devices under the supervision of Dr. P. H. Holloway. Her research area emphasized electron beam evaporation of ZnMgS:Mn, and pulsed laser and RF sputter deposition of Zn_2GeO_4:Mn. She spent the summer, 2000, at Bell-Labs investigating Si shallow junction leakage current and TEM cross-section analysis under the supervision of Dr. H. J. Gossmann